INTERACTIONS IN SMALL COMPLEXES

Joe Phillip Harris

Thesis submitted to the University of Nottingham

for the degree of Doctor of Philosophy

May 2015

"Some subjects are so serious that one can only joke about them."

Niels Bohr

Abstract

High-quality potential energy curves (PECs) for several series of M^+–RG complexes (M = B, Be—Ra, and Zn—Hg, and RG = He—Rn) have been calculated using coupled cluster theory and large basis sets. Spectroscopic constants for these species have been calculated, and using trends in these in conjunction with orbital contour plots, partial atomic charges, and total local energy density analyses, the natures of the interactions are investigated. In general, high binding energies for rare gas complexes were obtained for many of these species. In particular, interactions between the metal cations, B^+ and Be^+, and the heavier rare gas atoms show very high dissociation energies, with some covalent component to the nature of bonding deduced.

The anionic MH^- (M = Be—Ra) and RG–H^- (RG = He—Rn) series are investigated through use of high quality PECs calculated at the coupled cluster level of theory using large basis sets, with spectroscopic constants being subsequently appraised. Dissociation energies in the RG–H^- series are found to be weak, although reaching moderate values for the heavier rare gases. Conversely, the MH^- series possess much higher dissociation energies, especially in the case of BeH^-. These differences are discussed in the context of hybridisation on the Group 2 metal centres, and comparison is also made to the isoelectronic BeHe complex.

Laser ablation has been employed to produce gas-phase copper atoms suitable for study by resonance-enhanced multiphoton ionisation spectroscopy (REMPI). Since the copper atoms result from an initial copper plasma, many

excited electronic states are prepared, which can yield interesting results when studied by electronic spectroscopy. REMPI spectra are presented of transitions from the ground state to the two spin-orbit split components of the low-lying $3d^{10}4p$ state, and to a series of higher lying $3d^{10}nd$ Rydberg states. Contributions from metastable initial electronic states are also seen, and assignments discussed.

Complexes between NO and the alkanes (alkane = methane, ethane, propane, and *n*–butane) have been studied by REMPI *via* the $\tilde{A}$ state, where the excitation is localised to the NO molecule. For NO–methane, only the 1:1 complex was observed, but for the longer chain alkanes additional higher-order NO–alkane$_n$ complexes were observed. Binding energies are deduced for the excited and ground states, and structures for these complexes elucidated, aided by use of *ab initio* calculations.

Publications Covered by this Thesis

Interactions in the B^+–RG Complexes and Comparison with Be^+–RG (RG = He—Rn): Evidence for Chemical Bonding, Joe P. Harris, Adrian M. Gardner, Timothy G. Wright, W. H. Breckenridge, and Larry A. Viehland, *The Journal of Physical Chemistry A*, 2012, **116**, 4995.

Spectroscopy of the $\tilde{A}$ state of NO–alkane complexes (alkane = methane, ethane, propane, and n-butane), Victor M. Tamé-Reyes, Adrian M. Gardner, Joe P. Harris, Jodie McDaniel, and Timothy G. Wright, *The Journal of Chemical Physics*, 2012, **137**, 214307.

Comparison of the interactions in the rare gas hydride and Group 2 metal hydride anions, Joe P. Harris, Daniel R. Manship, W. H. Breckenridge, and Timothy G. Wright, *The Journal of Chemical Physics*, 2014, **140**, 084304.

Resonance-enhanced multiphoton ionization spectroscopy of laser-ablated copper atoms, Anna Andrejeva, Joe P. Harris, Timothy G. Wright, *Chemical Physics Letters*, 2014, **613**, 80.

HM^+ and HM^+He (M = Group 2 metal): Chemical or physical interactions?, Joe P. Harris, Hannah Dodson, W. H. Breckenridge, and Timothy G. Wright, *The Journal of Chemical Physics*, 2014, **141**, 094306.

HM^+–RG complexes (M = group 2 metal; RG = rare gas): Physical vs. chemical interactions, Joe P. Harris, Hannah Dodson, W. H. Breckenridge, and Timothy G. Wright, *The Journal of Chemical Physics*, 2015, **142**, 154302.

Publications Not Covered by this Thesis

Interaction of the NO 3pπ Rydberg state with Ar: Potential energy surfaces and spectroscopy, Olga V. Ershova, Jacek Kłos, Joe P. Harris, Adrian M. Gardner, Victor M. Tamé-Reyes, Anna Andrejeva, Millard H. Alexander, Nicholas A. Besley, and Timothy G. Wright, *The Journal of Chemical Physics*, 2013, **138**, 214313.

Vibrations of the S_1 state of fluorobenzene-h_5 and fluorobenzene-d_5 via resonance-enhanced multiphoton ionization (REMPI) spectroscopy, Joe P. Harris, Anna Andrejeva, William D. Tuttle, Igor Pugliesi, Christian Schriever, and Timothy G. Wright, *The Journal of Chemical Physics*, 2014, **141**, 244315.

Acknowledgements

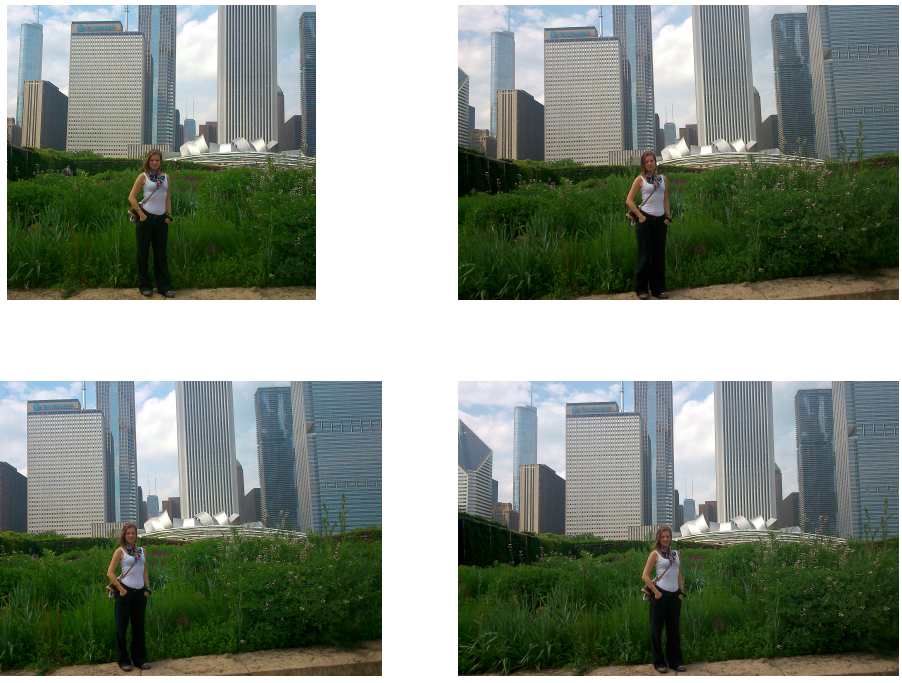
Above all else, I offer my heartfelt thanks to my supervisor, Tim. Without his constant guidance, aid, and patience, I would be nowhere. He has been a source of insight on many matters, and always there to provide help when needed. Not to mention his incredible jokes.

There are also the many people I've had the fortune to work with; thanks to Dr. Adrian Gardner for showing me the ropes—and not throttling me with them. A mention must go to Victor Tamé-Reyes, Dr. Jonny Midgley, and Dr. Steve Daly, who provided much entertainment in their own, special ways, and Gerardo Raggi and Nicolas Saquet, with whom a great deal of squash has been played. Victoria Wilton has always been there for me when needed, whether to offer reassurance or, more profitably, cake. The project students with whom I've worked more directly, Daniel Manship and Hannah Dodson, have been a pleasure. Recent addition to the group William Tuttle has also been a lot of fun to work with. Last (but far from least!) is the indispensible Anja Andrejeva, who has been a wonderful partner in crime as we somehow figured out how everything is supposed to work, together.

It has been a pleasure to work with long-standing collaborator of the group Bill Breckenridge, especially on his visits, bringing a fresh perspective to many problems. The workshop team have been vital to any experimental efforts, especially Paul Gaetto, who diligently machined a great many copper rods without even complaining. General overlord of the school Neil Barnes has always been on hand to show me exactly how I'm doing everything

wrong, as well as how to fix it.

Thanks must also go to my mother and father, who have supported me throughout this endeavour. Often with huge quantities of food.



Impromptu 'photo session' with Anja in Chicago, after ISMS 2014.

Not shown: the accepted 63rd attempt.

Contents

1 Introduction **1**

1.1 Chemistry of Rare Gas Atoms 1

1.2 Nitric Oxide Complexes 5

2 Computational Techniques **11**

2.1 Computational Theories 11

2.1.1 Configuration Interaction (CI) Theory 11

2.1.2 Coupled-Cluster (CC) and Quadratic Configuration Interaction Singles and Doubles (QCISD) Theories . 13

2.2 Basis Sets 14

2.2.1 Correlation-Consistent Basis Sets 15

2.2.2 Effective Core Potentials (ECPs) 17

2.3 Population Analyses 18

2.3.1 Mulliken Population Analysis 18

2.3.2 Natural Bond Orbital (NBO) Theory 18

2.3.3 Atoms in Molecules 19

2.4 Derivation of Spectroscopic Constants 20

2.4.1 Dissociation Energies 20

2.4.2 Basis Set Superposition Error (BSSE) 22

2.4.3 Morse Relationships 24

2.4.4 Birge-Sponer Plots 25

3 Theoretical Results on the B^+–RG series **29**

3.1 Computational Methodology 30

3.2 Previous Studies 32

3.2.1 B^+–He 32

3.2.2 B^+–Ne 33

3.2.3 B^+–Ar 34

3.2.4 B^+–Kr, B^+–Xe, and B^+–Rn 35

3.3 Trends in Spectroscopic Constants 35

3.4 $D_e{}^{Morse}/D_e$ Ratios and Birge-Sponer Plots 37

3.5 Reduced Potential Plots 39

3.6 Molecular Orbital Diagrams and Orbital Contour Plots . . . 40

3.6.1 Li^+–He 40

3.6.2 B^+–He and B^+–Ne 42

3.6.3 B^+–Ar and B^+–Kr 43

3.6.4 B^+–Xe and B^+–Rn 45

3.7 Partial Charge Analyses 46

3.8 Local Energy Density $H(r)$ 47

3.9 Conclusions 47

4 Interactions in RG–H^- (RG = Rare Gas) and MH^- (M = Group 2 Metal) Species **51**

4.1 Computational Methodology 52

4.2 Rare Gas Hydride Complexes 53

4.2.1 Previous Studies 53

4.2.2 Geometric Parameters 54

4.2.3 Dissociation Energies 55

4.2.4 Partial Atomic Charges 56

4.2.5 Orbital Contour Plots 58

4.3 Metal Hydride Complexes 58

4.3.1 Multireference Calculations 58
4.3.2 Previous Studies 59
4.3.3 Geometric Parameters 62
4.3.4 Dissociation Energies 62
4.3.5 Partial Atomic Charges 62
4.3.6 Orbital Contour Plots 63
4.3.7 Group 2 Metal Hybridisation 65
4.4 Conclusions 67

5 Trends in the Group 2 and Group 12 M^+–RG series 71
5.1 Computational Methodology 72
5.2 Previous Studies 75
5.3 Trends in the Spectroscopic Constants of the Group 2 M^+–RG Series 76
5.3.1 Equilibrium Internuclear Separations 76
5.3.2 Dissociation Energies 78
5.3.3 Harmonic Vibrational Frequencies and Force Constants 79
5.4 Trends in the Spectroscopic Constants of the Group 12 M^+–RG Series 80
5.4.1 Equilibrium Internuclear Separations 80
5.4.2 Dissociation Energies 81
5.4.3 Harmonic Vibrational Frequencies and Force Constants 82
5.5 Birge-Sponer Plots 83
5.6 Orbital Contour Plots 89
5.6.1 Be^+–RG Orbital Contours 89
5.6.2 Mg^+–RG Orbital Contours 93
5.6.3 Ca^+–RG and Sr^+–RG Orbital Contours 94
5.6.4 Ba^+–RG and Ra^+–RG Orbital Contours 96
5.6.5 Zn^+–RG Orbital Contours 97

5.6.6 Cd^+–RG Orbital Contours 100
5.6.7 Hg^+–RG Orbital Contours 101
5.7 Partial Atomic Charge Analyses 102
5.7.1 Group 12 Partial Atomic Charges 102
5.7.2 Group 2 Partial Atomic Charges 104
5.8 Comparison of Interactions in Groups 2 and 12 M^+–RG Complexes and Conclusory Remarks 107

6 Theoretical Results on the HM^+–RG Complexes 113
6.1 Introduction 113
6.2 Computational Methodology 114
6.3 Interactions in the HM^+ Complexes 116
6.3.1 Previous Results 116
6.3.2 Trends in Spectroscopic Parameters 119
6.3.3 Partial Atomic Charges and Contour Plots 120
6.4 Interactions Between HM^+ and RG atoms 123
6.4.1 Geometric Parameters 123
6.4.2 Harmonic Vibrational Frequencies 125
6.4.3 Contour Plots 126
6.4.4 Dissociation Energies 127
6.4.5 Partial Atomic Charges 129
6.4.6 Charge Induced Dipole Interactions 132
6.5 Comparison to M^+–RG and M^{2+}–RG 135
6.6 Conclusions 140

7 Resonance-Enhanced Multiphoton Ionisation Spectroscopy 145
7.1 Experimental Apparatus 147

8 Spectroscopy of Laser-Ablated Copper: Towards Copper-Containing Complexes 151

8.1 Introduction 151
8.2 Experimental 153
8.3 Spectra of Atomic Copper 156
8.3.1 One-Colour (2 + 1) REMPI Spectra 156
8.3.2 Two-Colour (1 + 1′) REMPI Spectra 159
8.3.3 Metastable States of Copper 160
8.4 Cu–Kr Complex 163
8.5 Conclusions 166

9 Spectroscopy of NO–Alkane Complexes 171

9.1 Introduction 171
9.2 Experimental 172
9.3 NO–Alkane 1:1 Complex Spectra 173
9.3.1 NO–methane 174
9.3.2 NO–ethane 175
9.3.3 NO–propane and NO–(*n*–butane) 176
9.3.4 Discussion of Binding Energies for the 1:1 NO–alkane Spectra 177
9.4 NO–Alkane 1:1 Complex Ground State Calculations 178
9.4.1 Computational Methodology 178
9.4.2 NO–methane 179
9.4.3 NO–ethane 183
9.4.4 NO–propane 185
9.4.5 NO–(*n*–butane) 185
9.5 Higher-Order NO–Alkane$_n$ Complexes 187
9.5.1 NO–ethane$_2$ 187
9.5.2 NO–ethane$_3$ 189
9.5.3 NO–propane$_2$ 191
9.5.4 NO–(*n*–butane)$_2$ 192

9.6 Conclusions 193

List of Figures

3.1 Birge-Sponer plots for the B^+–RG series. The lines plotted are linear extrapolations from the first two points, and represent Morse-like behaviour. 37

3.2 Reduced potential plots for the B^+–RG series. For each point of the *ab initio* potential, the internuclear separation R has been divided by R_e, and the interaction energy E_{int} has been divided by D_e of the respective species. 39

3.3 MO diagram for the Li^+–He complex. The energy levels and the contours are taken from a HF calculation using the CCSD(T)/a∞Z R_e value. 41

3.4 MO diagram for the B^+–He and B^+–Ne complexes. The energy levels and the contours are taken from a HF calculation using the CCSD(T)/a∞Z R_e value. 43

3.5 MO diagram for the B^+–Ar and B^+–Kr complexes. The energy levels and the contours are taken from a HF calculation using the CCSD(T)/a∞Z R_e value. 44

3.6 MO diagram for the B^+–Xe and B^+–Rn complexes. The energy levels and the contours are taken from a HF calculation using the CCSD(T)/a∞Z R_e value. 45

4.1 Natural orbital contour plots for selected members of the RG–H^- series. 57

4.2 Natural orbital contour plots for selected members of the MH^- series at varying internuclear separations. 64

5.1 Birge-Sponer plots for the Be^+–RG series. 83
5.2 Birge-Sponer plots for the Mg^+–RG series. 84
5.3 Birge-Sponer plots for the Ca^+–RG series. 84
5.4 Birge-Sponer plots for the Sr^+–RG series. 85
5.5 Birge-Sponer plots for the Ba^+–RG series. 85
5.6 Birge-Sponer plots for the Ra^+–RG series. 86
5.7 Birge-Sponer plots for the Zn^+–RG series. 86
5.8 Birge-Sponer plots for the Cd^+–RG series. 87
5.9 Birge-Sponer plots for the Hg^+–RG series. 88
5.10 Orbital energy plots for selected members of the Be^+–RG series (see text for details). 90
5.11 Orbital energy plots for selected members of the Mg^+–RG series (see text for details). 93
5.12 Orbital energy plots for selected members of the Ca^+–RG series (see text for details). 94
5.13 Orbital energy plots for selected members of the Sr^+–RG series (see text for details). 95
5.14 Orbital energy plots for selected members of the Ba^+–RG series (see text for details). 96
5.15 Orbital energy plots for selected members of the Ra^+–RG series (see text for details). 97
5.16 Orbital energy plots for selected members of the Zn^+–RG series (see text for details). 98
5.17 Orbital energy plots for selected members of the Cd^+–RG series (see text for details). 99

5.18 Orbital energy plots for selected members of the Hg^+–RG series (see text for details). 101

6.1 Contour plots of the HM^+ and HM^+RG complexes. 122

6.2 Trends in equilibrium internuclear separation between metal and rare gas for the M^+–RG, HM^+–RG, and M^{2+}–RG series. Each plot corresponds to a specific metal series with each rare gas. 136

6.3 Trends in equilibrium internuclear separation between metal and rare gas for the M^+–RG, HM^+–RG, and M^{2+}–RG series. Each plot corresponds to a specific rare gas series with each metal. 137

6.4 Trends in equilibrium dissociation energy between metal and rare gas for the M^+–RG, HM^+–RG, and M^{2+}–RG series. Each plot corresponds to a specific metal series with each rare gas. 138

6.5 Trends in equilibrium dissociation energy between metal and rare gas for the M^+–RG, HM^+–RG, and M^{2+}–RG series. Each plot corresponds to a specific rare gas series with each metal. 138

7.1 Schematic representation of different multiphoton ionisation regimes. 145

7.2 Diagram of the experimental apparatus used to perform REMPI. 148

8.1 Schematic of the LaVa source. 154

8.2 Different REMPI schemes used. Trace a) shows the one-colour (2 + 1) REMPI process responsible for the ^2D Rydberg spectrum, and trace b) the two-colour (1 + 1′) REMPI process which leads to the observation of the ^2P spectrum. 155

8.3 REMPI spectrum of ^{63}Cu, recorded under one-colour conditions. Trace a) shows mainly contributions from $3d^{10}nd \leftarrow 3d^{10}4s$ transitions, trace b) shows increasing contributions from transitions originating from metastable excited electronic states, and in trace c) some metastable transitions are seen to be more intense than the $3d^{10}nd$ lines. 157

8.4 REMPI spectrum of ^{63}Cu using (1 + 1′) REMPI conditions, with low (trace a) and higher (trace b) excitation laser powers. 159

8.5 Spectrum of Cu–Kr recorded using one-colour (1 + 1) REMPI, taken from Reference 1. 164

9.1 (1 + 1) REMPI spectra of the 1:1 NO–alkane complexes shifted so that the pure electronic transition is at zero wavenumber—see Table 9.1 for values of T_0. The data for NO–methane comes from Reference 9. The lines marked on the spectra indicate D_L, the dissociation limit being reached. 173

9.2 Energetic cycle used to calculate the ground state binding energy D_0''. 175

9.3 Optimised structures obtained by UMP2 calculations for the NO–ethane complex, along with the energy relative to that of the most stable structure obtained by CCSD(T) calculations. 182

9.4 Optimised structures obtained by UMP2 calculations for the NO–propane complex, along with the energy relative to that of the most stable structure obtained by CCSD(T) calculations. 184

9.5 Optimised structures obtained by UMP2 calculations for the NO–(*n*–butane) complex, along with the energy relative to that of the most stable structure obtained by CCSD(T) calculations. 186

9.6 Higher-order NO–ethane$_n$ spectra. The marked arrows correspond to the following quantities; *a*) T_0 for NO–ethane$_1$, *b*) D_L for NO–ethane$_1$, *c*) D_L for NO–ethane$_2$, *d*) D_L for NO–ethane$_3$. 188

9.7 Higher-order NO–propane$_n$ spectra. The marked arrows correspond to the following quantities; *a*) T_0 for NO–propane$_1$, *b*) D_L for NO–propane$_1$, *c*) D_L for NO–propane$_2$. 191

9.8 Full-range spectrum recorded in the NO–(n–butane)$_1$ mass channel. The marked arrows correspond to the following quantities; *a*) T_0 for NO–butane$_1$, *b*) D_L for NO–butane$_1$, *c*) D_L for NO–butane$_2$. 192

List of Tables

3.1 Spectroscopic constant for the B^+–RG series. R_e is the equilibrium bond length, D_e and D_0 are the equilibrium and zero point dissociation energies respectively, ω_e is the harmonic vibrational frequency, $\omega_e x_e$ is the anharmonicity constant, and k the force constant from Hooke's law. ${D_e}^{Morse}/D_e$ is calculated as outlined in Section 2.4.3. 31

3.2 Partial atomic charge analysis for the B^+–RG series in units of elementary charge e, and local energy density $H(r)$ from AIM analysis in atomic units. Q_{RG} is the partial atomic charge ascribed to the rare gas atom, and the corresponding charge on boron may be found as +(1 - Q_{RG}). 46

4.1 Spectroscopic parameters for the RG–H^- series. R_e is the equilibrium bond length, D_e and D_0 are the equilibrium and zero point dissociation energies respectively, ω_e is the harmonic vibrational frequency, $\omega_e x_e$ is the anharmonicity constant, and k the force constant from Hooke's law. 54

4.2 Ion/induced-dipole terms for the XH^- complexes. α_d is the polarisability of the metal or rare gas atom X, $-\alpha_d/2R^4$ is the ion/induced dipole interaction term, and IID/D_e is the ratio of the ion/induced-dipole to the equilibrium dissociation energy. 55

4.3 Partial atomic charge analysis for the RG–H^- and MH^- series in units of elementary charge e. For RG–H^- the charge on the RG atom is considered, and for MH^- the charge on M. 56

4.4 Values for the T_1 diagnostic for the MH^- series from CCSD(T) calculations, along with interaction energies in units of cm^{-1} calculated using MRCI+Q, CCSD(T), CCSD, and QCISD levels of theory with triple- and quintuple-ζ basis sets outlined in Section 4.1. The geometry has been fixed as the CCSD(T) R_e in each case. 59

4.5 Spectroscopic parameters for the MH^- series. R_e is the equilibrium bond length, D_e and D_0 are the equilibrium and zero point dissociation energies respectively, ω_e is the harmonic vibrational frequency, $\omega_e x_e$ is the anharmonicity constant, and k the force constant from Hooke's law. 61

4.6 NBO data for the HOMO and HOMO-1 orbitals for the MH^- series. 66

4.7 Energies of the $^1P \leftarrow {}^1S$ and $^1D \leftarrow {}^1S$ excitations for the Group 2 metals taken from Reference 17. 66

5.1 Spectroscopic constants for the Group 2 M^+–RG series. R_e is the equilibrium bond length, D_e and D_0 are the equilibrium and zero point dissociation energies respectively, ω_e is the harmonic vibrational frequency, $\omega_e x_e$ is the anharmonicity constant, and k the force constant from Hooke's law. ${D_e}^{\mathrm{Morse}}/D_e$ is calculated as outlined in Section 2.4.3. 77

5.2 Spectroscopic constants for the Group 12 M^+–RG series. R_e is the equilibrium bond length, D_e and D_0 are the equilibrium and zero point dissociation energies respectively, ω_e is the harmonic vibrational frequency, $\omega_e x_e$ is the anharmonicity constant, and k the force constant from Hooke's law. ${D_e}^{\text{Morse}}/D_e$ is calculated as outlined in Section 2.4.3. 82

5.3 Local energy densities $H(r)$ for the Group 2 M^+–RG complexes calculated at the BCPs in atomic units (E_h ${a_0}^{-3}$) . . . 91

5.4 Local energy densities $H(r)$ for the Group 12 M^+–RG complexes calculated at the BCPs in atomic units (E_h ${a_0}^{-3}$). . . 97

5.5 Partial atomic charges for the Group 12 M^+–RG complexes, calculated using NPA and AIM methodologies, in units of elementary charge e. 103

5.6 Partial atomic charges for the Group 2 M^+–RG complexes, calculated using NPA and AIM methodologies, in units of elementary charge e. 106

6.1 Spectroscopic constants for the HM^+ species. R_e is the equilibrium bond length, D_e is the equilibrium dissociation energy, and ω_e is the harmonic vibrational frequency. 118

6.2 Energies of the lowest $^2P \leftarrow {}^2S$ and $^2D \leftarrow {}^2S$ excitations for the Group 2 metal cations taken from Reference 15. 119

6.3 Partial atomic charges in atomic units (e) calculated using NPA and AIM theories from QCISD/aTZ density, and the total local energy density $H(r)$ at the BCPs in atomic units (E_h ${a_0}^{-3}$). 121

6.4 NBO data for the HOMOs for the HM^+ species. 121

6.5 Spectroscopic constants for the HM^+–RG species. 124

6.6 Equilibrium dissociation energies (/ cm^{-1}) for the HM^+–RG complexes both with (+ CP) and without full counterpoise correction using quadruple- and quintuple-ζ basis sets, and extrapolating to the basis set limit (EBS). 128

6.7 Partial atomic charges for the HM^+–RG series calculated using NPA and AIM theories from QCISD/aTZ density. . . 130

6.8 Total local energy densities $H(r)$ at the bond critical points BCP in the HM^+ HM^+–RG complexes. Values of less than zero indicate partial covalent character. 132

6.9 Ion/induced-dipole interaction terms (/ cm^{-1}) for the HM^+–RG complexes, and the ratio with the equilibrium dissociation energy. 135

6.10 Ratios of the dissociation energies for the M^+–RG, HM^+–RG, and M^{2+}–RG series. D_e^{R1+} is equal to $D_e(\frac{HM^+-RG}{M^+-RG})$, and D_e^{R2+} is equal to $D_e(\frac{M^{2+}-RG}{HM^+-RG})$ 139

8.1 Measured band positions for the $3d^{10}nd$ series, including previous positions reported by previous studies. 157

8.2 Assignments of the additional features observed in the (2 + 1) REMPI spectra. Energies of the states involved relative to the ground state are collected in Table 8.3. 161

8.3 Energetic positions of the states involved in the transitions from metastable states above the ground state. 161

9.1 Spectral parameters for the NO-alkane binary complexes. T_0 is the pure electronic transition, D_{L} is the dissociation limit, D_0' and D_0'' are the zero-point dissociation energies for the $\tilde{\mathrm{A}}$ and $\tilde{\mathrm{X}}$ states respectively, and D_{e} is the $\tilde{\mathrm{X}}$ state equilibrium dissociation energy from RCCSD(T) calculations at the UMP2 optimised geometry, using the 'best' result available. 175

9.2 Calculated $\tilde{\mathrm{X}}$ state equilibrium dissociation energies, D_{e}. All single-point calculations in the present study have been conducted at the optimised UMP2/aTZ energetic minimum structure. 179

9.3 Calculated spectroscopic constants for the higher-order NO–alkane$_n$ complexes. D_{L} is the measured dissociation limit, and ${D_0}^{\mathrm{All}}$ and ${D_0}^1$ are the dissociation energies with respect to loss of all and one alkane from the excited state, respectively. 186

Chapter 1

Introduction

1.1 Chemistry of Rare Gas Atoms

When one considers complexes of rare gas atoms, interactions in such species have often been presumed to be both predictable and uninteresting. The members of Group 18, helium, neon, argon, krypton, xenon, and radon, all possess closed shell ground state electronic configurations, along with high ionisation energies and negative electron affinities (i.e. the anion is unstable).[1] This makes any degree of 'chemical' interaction, typified by covalent bond formation, rather unlikely. Further, the unoccupied virtual orbitals of these elements are all quite high in energy, presenting a significant barrier to orbital hybridisation. As Group 18 is descended, the polarisability of these elements is seen to increase which paves the way for reasonably strong induction terms, along with the increasing numbers of electrons giving stronger dispersion interactions. Consequently, systems which involve rare gases are often thought of as being characterised by weak binding energies, with the interactions in these species being dominated by 'physical' forces, such as ion/induced-dipole, dispersion, and electron repulsion.

However, this is not always the case. In 1962, Neil Bartlett synthesised the first rare gas complex stable at room temperature, xenon hexafluoroplatinate $Xe^{+}[PtF_6]^{-}$.[2] Spectroscopic studies have subsequently been conducted on

a wide range of rare gas-containing species, and in some cases the binding energies with respect to loss of rare gas atom have been found to be fairly significant. A prominent example of this is the coinage metal-halide series of complexes, of the general form RGMX, where X = halogen (F—Br), M = coinage metal (Cu—Au), and RG = rare gas (He—Rn). The first preparations of some members of this series for RG = Ar were performed by Michael Gerry and coworkers,[3–6] by means of laser ablating metal into a pulsed jet of rare gas atoms seeded with a suitable halogen precursor, with the resulting complexes being characterised by Fourier transform microwave spectroscopy.

Despite these advances with the heavier rare gas atoms, there has yet to be experimental detection of a stable helium molecule. Theoretical predictions have been made for several candidates, the FMRG complexes in particular showing very high binding energies for even the lighter rare gases,[7,8] with the binding energy for the helium atom in the FCu–He complex having been calculated as 2270 cm^{-1} using CCSD(T) theory, and the Cu–He bond found to possess a small degree of covalency.[8] Of the neon complexes, the existence of the NeAuF complex was later verified in matrix isolation studies.[9,10]

Other possible candidates come from complexes with beryllium. Grandinetti and coworkers proposed a functional group of the form RNBeRG,[11,12] where the R group can range from atomic substituents such as H or F, to extensive organic groups. This RNBeRG moeity is effectively a functional group in which the binding energy of the RG atom is essentially independent of R. Binding energies for the rare gases are significant, with the value for loss of He coincidentally being $\sim$2270 cm^{-1}.[11]

The underlying principle behind these species is to provide a chemical environment in which the atom binding helium possesses a formal positive charge of +1 e or greater which facilitates a donor-acceptor type interaction,

with helium being the donor.[13] It follows from this that cationic systems would provide an ideal environment for binding helium atoms,[14] and there have been a great many studies published on such systems,[15,16] including the simplest such systems, the M^{n+}–He diatomics, as well as many studies on the heavier rare gas analogues.[17] Developing an understanding of these simpler diatomic systems also contributes to an understanding of how the binding of rare gas atoms proceeds in the larger systems.

Many of the above mentioned studies include a computational aspect, or are entirely theoretical studies. One of the chief advantages to performing computational studies comes from their flexibility. Experimental studies can often take a very long time in order to build the instrument, and even following this, results can be very slow to obtain. Conversely, theoretical methods allow access to arbitrary systems quite easily, although high-level calculations may become prohibitively expensive to perform on mid- to larger-sized systems. Thus, theoretical predictions can be used to guide experimental focus to the most promising systems.

Once the wavefunction for a species has been calculated, many properties can be deduced. Information on dissociation energies can be appraised along with geometric parameters, and in many cases these provide a direct route to comparison with experimental results in order to assess the accuracy of the calculations. On top of this, theory provides an avenue to investigate other properties of a system. This can include orbital hybridisation, with a breakdown of the individual contributing orbitals, or partial atomic charges which go beyond the strictures of simple Lewis structures and subdivide the electron density between the atoms. Energies of individual orbitals in a complex or molecule can be mapped out, and contour plots of orbital density produced to provide a visual representation of each orbital. Taken in combination, these various other analyses can give deep insight into the

interactions which are present in a system.

Information on the character of a system can be especially powerful when trends across various related systems are examined. If the underlying differences responsible for subtle (or not so subtle) differences in the characters of closely related systems can be elucidated, it becomes possible to attempt to predict systems which have certain properties. In the context of the chemistry of the rare gases, the driving force behind these efforts is to predict systems which will be able to bind rare gas atoms strongly. In this thesis, two chapters are devoted to theoretical results on metal cations interacting with the rare gas atoms. By developing a working understanding of the binding in these species, it is possible to highlight species in which the metal is chemically 'modified' to attempt to exaggerate the properties of those metals which give high dissociation energies in their rare gas complexes, with the aim of working towards discovering classes of species in which the rare gas atoms are bound by 'chemical'-type interactions, such as covalent bonding.

Other species suitable for intial investigation are those which are isoelectronic. An isoelectronic comparison to the BeHe system presents itself in BeH^-, with both species comprising interactions between two ground state ns^2 systems. Despite this similarity, there is an obvious difference in these species since the former is neutral and the latter anionic. The charged species will be subject to strong induction terms (chiefly an ion/induced-dipole interaction) that are not present in the BeHe neutral, along with strong Coulombic repulsion between the H^- anionic species and the electron density associated with the neutral beryllium atom. This can lead to quite significantly different forms of interaction in these seemingly similar species. Although the validity of isoelectronic reasoning has been questioned previously,[18,19] comparisons such as these still provide a means of investigating

the importance of Coulombic and induction terms.

Since experiments involving charged species are often challenging to perform, it is desirable to identify neutral species which may exhibit the same properties. To this end, experiments have been undertaken attempting to detect neutral complexes of copper with the rare gases, where laser ablation was the technique selected to produce gas-phase copper atoms from a solid metal target. Since the ablation process intially produces a copper plasma, many different electronic states are prepared. Aspects of these experimental results are also discussed in this thesis.

1.2 Nitric Oxide Complexes

Nitric oxide, NO, is a rare case of a stable ground state radical. Consequently, complexes of NO are often used as prototypical systems for the study of the interactions of radicals, and its doubly-degenerate ground $^2\Pi$ state can lead to interesting features in the electronic structure of its complexes. This, coupled with the fact that NO possesses a relatively low-lying series of Rydberg states, has lead to a rich history of spectroscopic study in a variety of complexes.[20–24]

As the value of n increases for the Rydberg states, the NO molecule begins to appear more like an NO^+ core with a distant electron, and the behaviour of the corresponding complexes converges toward cationic-like behaviour. Consequently, many of the terms important to the overall form of interaction are the same as those pertinent to the cationic M^+–RG complexes mentioned above. Whilst this is reasonably straightforward for the higher-n Rydberg states in which the ligand is situated 'inside' the Rydberg orbital, for the lower-n states which are intermediate between the neutral NO and high-lying Rydberg state $NO^+ + e^-$ regimes, there may be a significant interaction between the Rydberg electron and the ligand, which can also lead

to interesting consequences for the electronic structures of these complexes.

Complexes formed between radical and neutral species are somewhat unusual in that the interactions are not easily classified as either covalent bonding or van der Waals-type interactions.[20] These complexes are also of interest since they provide a model for studying how radicals and neutrals interact with one another, which is of particular importance in the context of chemical reactions. Such systems are termed 'pre-reaction' or 'encounter' complexes.

Nitric oxide is also important in many different roles. It is a key biological messenger molecule in many physiological[25] and neurological[26] pathways, and as such was named Molecule of the Year by Science in 1992.[27] As well as this, NO_x molecules are known atmospheric pollutants, and have been found as a cause of acid rain, making it important to develop an understanding of the atmospheric chemistry of NO and its complexes.

One of the key contributors of NO_x to the atmosphere is car exhausts. Another class of pollutants produced by this source is alkane molecules, providing a motivation for the study of NO–alkane complexes. As mentioned above, when considering the character of interaction in a complex, it is often instructive to investigate trends in closely related species. For the alkane molecules a series of similar species is readily available in short-chain, aliphatic species of varying length, making a systematic study possible.

For these NO–alkane complexes, there are a significant number of geometric factors to consider, as even the simplest member of this series, NO–methane$_1$, consists of seven atoms. Although the experiments described in this thesis do not provide any information pertaining directly to the geometries of the species under investigation, it is possible to employ *ab initio* methods in order to calculate such information. Experimental observations can provide a wealth of information relevant to binding energies

and the electronic states under investigation, and in combination with the results from calculations, a fairly complete description of these complexes is achievable.

Bibliography

[1] W. M. Haynes, *CRC Handbook of Chemistry and Physics*, CRC Press/Taylor and Francis, Boca Raton, FL, 2014.

[2] N. Bartlett, *Proc. Chem. Soc.*, 1962, 218.

[3] C. J. Evans and M. C. L. Gerry, *The Journal of Chemical Physics*, 2000, **112**, 1321–1329.

[4] C. J. Evans, A. Lesarri and M. C. L. Gerry, *Journal of the American Chemical Society*, 2000, **122**, 6100–6105.

[5] C. J. Evans, D. S. Rubinoff and M. C. L. Gerry, *Phys. Chem. Chem. Phys.*, 2000, **2**, 3943–3948.

[6] C. J. Evans and M. C. L. Gerry, *The Journal of Chemical Physics*, 2000, **112**, 9363–9374.

[7] W. Zou, Y. Liu and J. E. Boggs, *Chemical Physics Letters*, 2009, **482**, 207–210.

[8] C. J. Evans, T. G. Wright and A. M. Gardner, *The Journal of Physical Chemistry A*, 2010, **114**, 4446–4454.

[9] X. Wang, L. Andrews, K. Willmann, F. Brosi and S. Riedel, *Angewandte Chemie International Edition*, 2012, **51**, 10628–10632.

[10] X. Wang, L. Andrews, F. Brosi and S. Riedel, *Chemistry—A European Journal*, 2013, **19**, 1397–1409.

[11] P. Antoniotti, N. Bronzolino and F. Grandinetti, *The Journal of Physical Chemistry A*, 2003, **107**, 2974–2980.

[12] S. Borocci, N. Bronzolino and F. Grandinetti, *Chemistry A European Journal*, 2006, **12**, 5033–5042.

[13] G. Frenking, W. Koch, D. Cremer, J. Gauss and J. F. Liebman, *The Journal of Physical Chemistry*, 1989, **93**, 3397–3410.

[14] W. Koch, G. Frenking, J. Gauss, D. Cremer and J. R. Collins, *Journal of the American Chemical Society*, 1987, **109**, 5917–5934.

[15] P. Antoniotti, P. Facchini and F. Grandinetti, *International Journal of Mass Spectrometry*, 2003, **228**, 415–427.

[16] F. Grandinetti, *International Journal of Mass Spectrometry*, 2004, **237**, 243–267.

[17] D. Bellert and W. H. Breckenridge, *Chemical Reviews*, 2002, **102**, 1595–1622.

[18] G. Frenking and D. Cremer, *Noble Gas and High Temperature Chemistry*, Springer, 1990, pp. 17–95.

[19] G. Frenking, W. Koch and J. F. Liebman, *From Atoms to Polymers: Isoelectronic Analogies*, 1989, vol. 11.

[20] M. C. Heaven, *Annual Review of Physical Chemistry*, 1992, **43**, 283–310.

[21] Y. Kim and H. Meyer, *International Reviews in Physical Chemistry*, 2001, **20**, 219–282.

[22] S. R. Desai, C. S. Feigerle and J. C. Miller, *The Journal of Chemical Physics*, 1994, **101**, 4526–4535.

[23] D. E. Bergeron, A. Musgrave and T. G. Wright, *Phys. Chem. Chem. Phys.*, 2006, **8**, 4758–4765.

[24] S. E. Daire, J. Lozeille, S. D. Gamblin, T. G. Wright and E. P. F. Lee, *Phys. Chem. Chem. Phys.*, 2001, **3**, 917–924.

[25] D. S. Bredt and S. H. Snyder, *Annual Review of Biochemistry*, 1994, **63**, 175–195.

[26] S. R. Jaffrey and S. H. Snyder, *Annual Review of Cell and Developmental Biology*, 1995, **11**, 417–440.

[27] E. Culotta and D. Koshland, *Science*, 1992, **258**, 1862–1865.

Chapter 2

Computational Techniques

2.1 Computational Theories

Weakly-bound ion/neutral systems often have interaction potentials which are dominated by electrostatic or 'physical' interactions, including ion/induced-dipole, dispersion, and repulsive interactions. Covalent forces, which are responsible for 'chemical' bonding in 'normal' molecular systems, are usually either insignificant or completely absent. Consequently, these types of systems are often quite challenging to describe adequately using theoretical methods, and so the level of theory employed is highly important in these cases.

2.1.1 Configuration Interaction (CI) Theory

Configuration Interaction (CI) theory is an extremely powerful method which can give very good results. A Hartree-Fock reference wavefunction is used to generate excited Slater determinants by promoting electrons from ground state occupancies into virtual orbitals. The CI wavefunction is found as a weighted sum of these determinants, as represented by Equation 2.1;

$$\Psi_{\mathrm{CI}} = a_0 \Phi_{\mathrm{HF}} + \sum_{\mathrm{S}} a_{\mathrm{S}} \Phi_{\mathrm{S}} + \sum_{\mathrm{D}} a_{\mathrm{D}} \Phi_{\mathrm{D}} + \sum_{\mathrm{T}} a_{\mathrm{T}} \Phi_{\mathrm{T}} + \ldots = \sum_{i=0} a_i \Phi_i \quad (2.1)$$

where S, D, T... represent the order of excitation as singles, doubles, triples etc. The optimisation of the CI wavefunction comes from using the variational theorem to minimise the total energy of the system by variation of the expansion coefficients, under the restriction that the total wavefunction is normalised, with the orbitals held fixed.[1]

Different levels of excitation of the Slater determinants are classified by how many electrons are moved compared to the reference determinant, e.g. a one-electron excitation is referred to as singly excited, a two-electron excitation is doubly excited etc. The excited determinants invoked by CI allow electrons to use virtual orbitals which remain unoccupied in Hartree-Fock theory. This reproduces the effects of instantaneous electron-electron interactions, referred to as dynamic electron correlation. These effects are crucial to the modelling of dispersion forces, and so it is vital to employ an *ab initio* method which follows this framework when running calculations on weakly-bound systems in which such forces are important, or for applications where highly accurate results are required.

Full CI (FCI), using all types of excitations up to N_{elec}, the total number of electrons, will recover all of the correlation energy of a system (for a specific basis set). However, this method is very computationally expensive, restricting use of FCI to very small systems, and so it is more useful instead to truncate the order of excitations. Restricting the order of excitation to singles only (CIS) is not much better than conducting a HF calculation, as matrix elements connecting the ground state HF reference wavefunction and all singly-excited determinants are found to be zero, a conclusion known as Brillouin's theorem (although there may still be small off-diagonal contributions). Thus, the lowest *useful* truncation of CI is CID.

The results of truncated CI can be improved by including different levels of excitations, denoted systematically as CISDTQ... (singles, doubles, triples,

quadruples...) etc. These formulations of CI can still recover a significant amount of the correlation energy, but they all suffer from a significant issue in that they (unlike FCI) are not size-consistent, meaning that the correlation energy recovered is dependent on the total number of electrons, with less correlation energy being recovered for systems with more electrons. One ramification of this is that a calculation conducted on a bi-molecular system A_2 at long separation will not return the same energy as twice the value from a calculation carried out on one molecule A.[2]

2.1.2 Coupled-Cluster (CC) and Quadratic Configuration Interaction Singles and Doubles (QCISD) Theories

Coupled Cluster (CC) theory corrects the lack of size-consistency of truncated CI by generating excitations through use of the cluster operator $\boldsymbol{T}$. Instead of linearly generating excitations as in CI, it instead uses an exponential term, $e^{\boldsymbol{T}}$. As a result, not only are the 'true' or 'connected' excitations produced, but also 'disconnected' excitations resulting from the products of excitations. For example, using the cluster operator $\boldsymbol{T}_2$ to produce double excitations (i.e. CCD) results in the expression shown in Equation 2.2;

$$\begin{aligned} \Psi_{\mathrm{CCD}} &= e^{\boldsymbol{T}_2}\,\Psi_{\mathrm{HF}} \\ &= \left(1 + \boldsymbol{T}_2 + \frac{\boldsymbol{T}_2^2}{2!} + \frac{\boldsymbol{T}_3^2}{3!} + \dots\right)\Psi_{\mathrm{HF}} \end{aligned} \tag{2.2}$$

Here, double excitations are seen to give rise to the connected double excitations represented by the term $\boldsymbol{T}_2$, as well as the disconnected excitations arising due to products of double excitations, represented by the

higher order members of the Taylor expansion. These additional terms are equivalent to higher order excitations, e.g. the square of $\boldsymbol{T}_2$ results in some quadruple excitations, and it is the absence of such terms from a truncated CI treatment that renders it not size-consistent.[3]

A closely-related approach to CCSD is Quadratic Configuration Interaction Singles and Doubles (QCISD) theory. The motivation behind the development of this theory was similar to that of CC theory, i.e. to include additional higher-order excitation terms to correct the issues caused by truncation of CI. In practice, the excitations produced by both of these theories are largely the same with only a few extra terms present in CCSD, and so application of one theory over another comes down to considerations of availability and relative speeds of algorithms in different quantum chemical packages.[2]

As a less computationally-intensive way of including the effects of higher-order excitations, the effects can be approximatly accounted for by use of perturbation theory, denoted by inclusion of those terms in parenthesis. CCSD(T), which includes perturbative treatment of triple excitations, is a particularly common methodology. Perturbative treatment tends to over-predict the energy of the triples, but fortuitously it does so by an amount approximately equal to the underprediction in energy arising from the neglection of quadruple excitations. This cancellation of errors means that CCSD(T) is a highly accurate theory, whilst remaining computationally feasible for small to mid-sized systems.

2.2 Basis Sets

Equally important as the choice of an appropriate level of theory is the selection of basis sets appropriate to the system at hand. Ideally, a complete basis set consisting of infinite basis functions would be used, but clearly this

is computationally impossible and compromises must be made. In general, as more and more basis functions are added to the basis set, the quality of the results will increase up to the point at which addition of further basis functions does not affect the results, referred to as the basis set limit. However, larger basis sets will be more computationally costly to use, and so care must be taken to select strategically the fewest basis functions needed to describe well the properties of a given species.

2.2.1 Correlation-Consistent Basis Sets

It is important to use basis sets with functions appropriate to the orbitals involved. At the most basic level, a basis set will need to have one function to describe each occupied orbital, referred to as a minimal basis set. In practice however, the results obtained by use of such a basis set are often very poor, and instead multiple functions per orbital give a much better representation. For example, at the double–ζ level the number of basis functions is doubled, at triple–ζ it is tripled etc.

For the calculations presented within this thesis, Dunning-style basis sets have been used; more specifically of the correlation-consistent type, denoted by the letters 'cc'. The chief advantage of these basis sets is that due to the way in which they are constructed, as the size (or 'quality') of the basis set is increased, the amount of correlation energy recovered increases systematically; thus, if a calculation is performed multiple times using basis sets of systematically increasing quality, the energies can be extrapolated to the basis set limit. This extrapolation can be applied using the cubic two-point extrapolation procedure of Halkier *et al.*[4] as per Equation 2.3:

$$E_{\infty \mathrm{Z}} = \frac{E_{\mathrm{mZ}} \cdot m^3 - E_{\mathrm{nZ}} \cdot n^3}{m^3 - n^3} \tag{2.3}$$

where m and n refer to quality of the basis sets, e.g. for extrapolation from quadruple– and quintuple–ζ quality basis sets, $m = 4$ and $n = 5$. Tests have shown that the initial use of higher quality basis sets gives a more sensitive extrapolation to the basis set limit and so it is still desirable to use basis sets of high quality, although there is little to be gained in using basis sets of higher than 5Z quality in all but the highest accuracy calculations since the errors introduced by the extrapolation procedure can outweigh the improvement in the result.

Polarisation effects are often crucial to the description of a system, and this is most important for the valence orbitals which typically dominate atomic interactions. A basis set able to represent these effects is indicated by the symbol 'pV' in Dunning-style basis sets. For some applications the use of a polarisation-valence only basis set is sufficient, but when seeking highly accurate results the small effects from inclusion of polarisation of core orbitals also need to be accounted for, and so appropriate basis functions will need to be included in the basis set. The presence of such functions is denoted by the symbol 'C'. Since the effects of valence orbitals are typically more important than those of the core orbitals, it is advantageous to employ basis sets which are weighted for the description of core-valence (as opposed to the less important core-core) correlation effects; such basis sets are denoted by use of the letters 'wC'.[5]

Systems which contain a significant degree of dispersion require basis functions which are suited to the description of these effects. Augmenting the basis set with diffuse functions is an effective way of doing this, usually achieved by adding an extra function of each angular momentum already present in the basis set, with a low exponent. Such basis sets are denoted by the 'aug' prefix for Dunning-style basis sets. Without these diffuse functions, dispersion effects are effectively 'switched off', or at least significantly reduced.

For strongly bound covalent systems, these effects are often much weaker than other binding interactions, and exclusion of diffuse functions is more permissible.

2.2.2 Effective Core Potentials (ECPs)

Since larger systems with increasing numbers of electrons become very computationally expensive quite quickly, it is desirable to keep the number of electrons which need to be treated in a system as low as possible without impacting the quality of the results obtained. A common way of doing this for heavy atoms is use of effective core potentials (ECP), also referred to as pseudopotentials (PP).

Heavy atoms (typically from the third row and down) possess core electrons which are energetically well separated from the valence orbitals, as well as being well-shielded from their environment by the valence orbitals. Being largely unaffected by the molecular environment, these electrons do not contribute to atomic interactions. It is thus possible to use an effective core potential, or ECP, which is a fitted function designed to emulate the core orbitals, requiring only very inexpensive optimisation during calculations. It is also important to use a basis set which omits basis functions for (as well as being orthogonal to) those orbitals described by the ECP—such basis sets are denoted by the suffix 'PP'.

Use of an ECP will reduce the computational expense of the calculation. Furthermore, since the ECP is calculated separately, additional considerations can be taken into account which would be too expensive to include explicitly in an all-electron calculation, chief among these being relativistic effects. Due to the types of atoms and orbitals which are suitable for ECP treatment (i.e. core orbitals on heavy atoms) the electrons included are naturally susceptible to such effects, but these considerations can be

modelled in the ECP, thus obviating the need for expensive fully-relativistic calculations in many cases.

2.3 Population Analyses

2.3.1 Mulliken Population Analysis

A useful property of a system to consider is the charge associated with each atom. One computationally inexpensive way of achieving this is Mulliken population analysis.[1] Each molecular orbital can be expressed as the weighted sum of each basis function. Using the total occupancy of each MO and the coefficients for the basis functions, the electrons can be subdivided between centres based on the contributions of the atomic basis functions to the final optimised orbitals, and partial atomic charges allocated.

Although this methodology is quick, it does have limitations, one of the more important coming from the way in which subdivision of the overlap population (i.e. electrons found in orbitals which belong to more than one atom) is handled; in these cases, the electrons are split equally between contributing centres, ignoring the concept of electronegativity. The shortcomings of Mulliken analysis can be manifested as unphysical results, including orbital occupancies of more than two electrons, or negative occupancies.

2.3.2 Natural Bond Orbital (NBO) Theory

Natural Bond Orbital theory attempts to rationalise theoretical results in a chemically accessible way, under the frameworks of Lewis structures and hybridisation theory.[6] The first step is the transformation of the input basis functions into natural atomic orbitals (NAOs), by use of the first-order density matrix; this is organised such that all basis functions from a given centre are arranged in a block, and these blocks are then diagonalised to

give the non-orthogonal 'pre-NAOs'. Orthogonalisation of the pre-NAOs gives the NAOs. A Mulliken-type population analysis can be conducted on these NAOs within the basis of the pre-NAOs to give the 'natural charges', with the sum of the diagonal elements of the density matrix giving the population from each orbital on each centre. Strict orthonormalisation of the NAOs ensures that the results are physically relevant, correcting many of the problems present in Mulliken population analysis.

The NAOs can then be transformed into natural bond orbitals (NBOs) by analysis of off-diagonal blocks in the density matrix constructed with an NAO basis. Using occupancy thresholds to determine if an orbital should be classified as core or lone-pair, NAOs arising from only one centre are removed. Two-centre blocks of the density matrix are then checked for orbitals which have an occupancy which exceeds another adjustable threshold value. Any matches are determined to be bonding orbitals, with the percentage contribution of any atom involved with the formation of a particular NBO reported. Listing of atomic contributions is further subdivided to the NAOs of different angular momenta on an atom, thus providing additional information on any hybridisation occurring.

2.3.3 Atoms in Molecules

Bader's Atoms in Molecules theory[7] provides a methodology for the systematic subdivision of a molecule into its substituent atoms purely through analysis of the form of the electron density. The vector gradient, $\boldsymbol{\nabla}\rho$, is calculated at some arbitrary point r_0, this vector is then followed 'downhill' for a distance Δr before recalculating $\boldsymbol{\nabla}\rho$. Repeating this procedure will trace out lines of minimum electron density which separate atoms, with the mapping of these atomic boundaries becoming exact in the limit $\Delta r \rightarrow \mathrm{d}r$. Partial atomic charges for each atom can be obtained by integrating the

electron density over each atomic basin.

Further analysis of the electron density allows 'interaction lines' to be identified, linking atoms together. The second differential of the electron density characterises these lines as having a maximum in two dimensions. The point along the interaction line which possesses a minimum along the third (i.e. internuclear) axis is referred to as a (3, -1) critical point (since the second differentials characterise stationary points in the gradient of ρ in three dimensions, two of which are negative and one positive i.e. +1-1-1 = -1) or a bond critical point (BCP), which can be thought of as the point of contact between the two 'surfaces' of electron density associated with the interacting atoms.

Various properties of the electron density can be obtained at these BCPs which are useful for characterising the overall form of interaction. One parameter which can be considered is the local energy density, $H(r)$,[8] calculated as the sum of the kinetic energy density, $G(r)$, and the potential energy density, $V(r)$. The sign of $H(r)$ is considered at the BCPs, and in cases where it is found to be less than zero (i.e. the electron density is stabilised) there is assumed to be some degree of covalency in the form of interaction. This analysis is useful in borderline cases or cases where covalency would not be expected to be observed, as very weak covalent interactions can be inferred.

2.4 Derivation of Spectroscopic Constants

2.4.1 Dissociation Energies

A detailed description of a species *ab initio* often requires calculation of a potential energy surface (PES), obtained by systematically distorting the nuclear framework and calculating the energy of the system at different

geometries. For diatomic species, which have only one geometric parameter and thus a one-dimensional potential energy surface (or potential energy curve, PEC), this problem is quite tractable, whereas for larger systems with more complicated geometric parameters, a full-dimensional PES quickly becomes prohibitively expensive.

Conversion of the PEC from total energy of the system to interaction energy can be achieved in two different ways. The first is the supermolecule approximation, wherein the energies of the isolated substituents are subtracted from the total energy, as per Equation 2.4;

$$E_{\text{int}} = E_{\text{AB}} - E_{\text{A}} - E_{\text{B}} \tag{2.4}$$

where E_{int} is the interaction energy, E_{AB} is the total energy of the system, and E_{A} and E_{B} are the total energies of the substituents. If the theory used is not size consistent, as discussed in Section 2.1.1, this approximation can introduce significant errors. Another way of generating the interaction energies is to take the total energy at very long separation, where interactions between the substituents are negligible, and to subtract this energy from every point on the curve, thus shifting the energy of the dissociation asymptote to zero.

A good quality PEC requires sampling the internuclear separation at many different separations, including the long-range asymptote, the potential well, and up the repulsive wall at very short separations. On its own however, even the highest quality PEC gives very little information on the nature of a species, and so various spectroscopic constants can be evaluated from the potential in order to describe its behaviour. These constants also provide excellent means of comparing different results for a species, for both theoretical-theoretical comparison and, arguably more importantly, theoretical-experimental. Results can also be compared across different species so that trends in related species can be elucidated.

Two important spectroscopic parameters are the equilibrium dissociation energy, D_e, which can be read from the interaction potential as the energy at the bottom of the potential well, and the equilibrium bond length, R_e, which is similarly read directly from the PEC, as the internuclear separation at the well minimum.

2.4.2 Basis Set Superposition Error (BSSE)

Use of incomplete basis sets can lead to a problem in which electrons centred on one atom may use basis functions centred on another atom when the two centres are very close. This problem is referred to as basis set superposition error (BSSE), and leads to unphysical lowering of energies which in turn leads to inaccuracies in calculated dissociation energies. Use of larger basis sets will reduce the magnitude of this error, although this solution is imperfect for all but a complete basis set, and use of a larger basis set is not always practical or practicable.

For interaction energies calculated using the supermolecule approach, one method that can be applied to correct for this error is the counterpoise (CP) correction. The extent of BSSE per fragment of the supermolecule can be appraised by performing calculations both on the isolated fragments, and on the isolated fragments in the presence of the basis functions of the other fragments held at the supermolecule geometry, without the associated electrons or nuclear charges. The difference in energy between these results is the BSSE, and can be subtracted from the non-CP corrected interaction energy to obtain the CP corrected D_e. Calculating simply the CP-corrected D_e without knowledge of the magnitude of BSSE can also be achieved by simply using the fragment energies as calculated in the presence of the other

basis functions in the supermolecule equation, as per Equation 2.5;

$$E_{\text{int}}{}^{\text{CP}} = E_{\text{AB}} - E_{\text{A[B]}} - E_{\text{B[A]}} \tag{2.5}$$

where E_{AB} denotes the energy of the supermolecule, and e.g. $E_{\text{A[B]}}$ is the energy of fragment A calculated with the basis functions of fragment B present.

Application of counterpoise correction must be considered carefully, since the sharing of basis functions between atoms could be considered an expression of covalency, and as such the selection of appropriate fragments can be difficult in larger, covalently-bound systems. For diatomic species however, the choice of fragments is rather more straightforward, although the selection of oxidation states for the fragments still needs to be approached with caution.

Other spectroscopic constants can be calculated using standard Morse relationships as outlined below, but they require values for at least the lowest two bound vibrational levels $v = 0, 1$ and the lowest rotational level B_0 (as well as D_{e}). These can be calculated through use of the LEVEL code.[9]

Taking an *ab initio* PEC, LEVEL solves an effective one-dimensional Schrödinger equation;

$$-\frac{\hbar^2}{2\mu}\frac{d^2\,\Psi_{v,J}(r)}{dr^2} + V_J(r)\,\Psi_{v,J}(r) = E_{v,J}\,\Psi_{v,J}(r) \tag{2.6}$$

wherein μ is the reduced mass, J is the rotational quantum number, and $V_J(r)$ is the sum of the rotationless electronic potential and a centrifugal term. Solving this produces eigenvalues $E_{v,J}$ which are the (ro)vibrational energy levels, as well as the eigenfunctions $\Psi_{v,J}(r)$ which can be used for evaluating Franck-Condon factors, although the latter results are not used in this thesis.

2.4.3 Morse Relationships

Using the constants R_e and D_e in conjunction with the lowest two vibrational levels and the lowest rotational level, standard Morse expressions can be used to obtain more spectroscopic constants. Equations 2.7 and 2.8 are used to calculate the harmonic vibrational frequency, ω_e, and the anharmonicity constant, $\omega_e x_e$;

$$\omega_e = \frac{9v_0 - v_1}{3} \tag{2.7}$$

$$\omega_e x_e = \frac{6v_0 - 2v_1}{3} \tag{2.8}$$

Equation 2.9 shows calculation of the equilibrium rotational constant, B_e, from Planck's constant h, the speed of light c, the reduced mass μ, and R_e;

$$B_e = \frac{h}{8\pi^2 \cdot c \cdot \mu \cdot {R_e}^2} \tag{2.9}$$

Related is the vibration-rotation constant α_e, calculated as per Equation 2.10 (where B_0 is calculated using Equation 2.9, substituting R_e by R_0);

$$\alpha_e = 2(B_e - B_0) \tag{2.10}$$

Although these rotational constants are easily calculated, they are not included in this thesis due to spatial constraints on the tables; they are, however, tabulated in the corresponding publications.

In order to appraise how well a PEC fits ideal Morse-like behaviour, it is possible to calculate ${D_e}^{\text{Morse}}$ using Equation 2.11;

$${D_e}^{\text{Morse}} = \frac{{\omega_e}^2}{4\omega_e x_e} \tag{2.11}$$

and ${D_e}^{\text{Morse}}$ can be subsequently compared to the *ab initio* D_e in the ratio

$\frac{D_e^{\text{Morse}}}{D_e}$.

Consideration of the vibrational frequencies as indicators of strength of interaction presents a problem when comparing interactions across different species, as the mass effect from the different elements can complicate changes in electronic effects. In order to remove the mass dependency, the force constant, k, from Hooke's law can be appraised as per Equation 2.12 (although care must be taken with units!);

$$k = 4\pi^2 \cdot c^2 \cdot {\omega_e}^2 \cdot \mu \tag{2.12}$$

2.4.4 Birge-Sponer Plots

The curvature of a potential can also be investigated by use of Birge-Sponer plots, created by plotting the spacing between adjacent vibrational levels v and $(v + 1)$, ΔG, against the average of the vibrational level number $(v + \frac{1}{2})$.

The original formulation of Birge-Sponer plots was to allow calculation of the binding energy of a species from experimental data when only a limited range of its spectrum is observable due to Franck-Condon factors, by assuming Morse-like behaviour and extrapolating from recorded vibrational level spacings to dissociation. D_e can be found as the sum of all vibrational level spacings, and so integrating the area under the curve will give a value for the dissociation energy assuming Morse-like behaviour. When instead the plotted data comes from calculated values, the full range of vibrational levels is available. Since ω_e and $\omega_e x_e$ as ascertained from the lowest two vibrational levels can be used to calculate vibrational energy levels also, it becomes possible to make a comparison between the Morse-like Birge-Sponer plot, and that created directly from the calculated vibrational energy levels.

For higher values of v, the vibrational wavefunction will sample greater

internuclear separations, meaning that v is dependent on R. Consequently, the shape of the Birge-Sponer plot is an expression of the R-dependence of the potential. Curvature of the Birge-Sponer plots at different values of v can be related to the relative importance of the interaction terms, although if any sort of hybridisation process occurs as a function of R this can affect the constants involved in the terms, complicating matters further.

Bibliography

[1] F. Jensen, *Introduction to Computational Chemistry*, Wiley, 2007.

[2] I. N. Levine, *Quantum Chemistry*, Pearson, 2014.

[3] C. J. Cramer, *Essentials of Computational Chemistry, 2nd Ed.*, Wiley, 2009.

[4] A. Halkier, T. Helgaker, P. Jørgensen, W. Klopper and J. Olsen, *Chemical Physics Letters*, 1999, **302**, 437–446.

[5] K. A. Peterson and T. H. Dunning, *The Journal of Chemical Physics*, 2002, **117**, 10548–10560.

[6] A. E. Reed, L. A. Curtiss and F. Weinhold, *Chemical Reviews*, 1988, **88**, 899–926.

[7] R. F. W. Bader, *Atoms in Molecules: A Quantum Theory*, Oxford Science Publications, 1990.

[8] D. Cremer and E. Kraka, *Angewandte Chemie International Edition in English*, 1984, **23**, 627–628.

[9] R. J. LeRoy, Level 8.0: A Computer Program for Solving the Radial Schrödinger Equation for Bound and Quasibound Levels, University of Waterloo Chemical Physics Research Report No. CP-663, 2007; see http://leroy.uwaterloo.ca/programs/.

Chapter 3

Theoretical Results on the B^+–RG series

Metal cations interacting with rare gas atoms are often used as a simple model for solvation of metal cations. Rare gas atoms characteristically show little or no chemistry and so the interactions in these systems are usually largely electrostatic or 'physical' in nature, making them relatively simple to comprehend. Additionally, their atomic nature means that there are few geometric complications to consider, which makes them appealing from a standpoint of computational expense.

From a standpoint of fundamental interest, these seemingly simple ion-neutral systems can also provide some fascinating instances of the borders between electrostatically-bound complexes and covalent molecules. Often, what would be expected to be straightforward interactions between closed shell or pseudo-closed shell species can give rise to more complicated forms of interaction, far more nuanced than might be assumed of the rare gases.

This chapter presents one such case of these systems in the form of the boron cation–rare gas complexes, B^+–RG, where RG = He—Rn. The rare gases are all closed shell and the boron cation has a $2s^2$ valence electronic structure, meaning these interactions are between ^1S systems and could be expected to give rise to interactions dominated by dispersion and ion/induced-

multipole forces, and essentially non-covalent bonding character. This *ab initio* study investigates whether these assumptions are true or not by examining spectroscopic constants for these species, and undertaking several other kinds of analysis with the intent being to shed light on the types of interactions occurring here.

3.1 Computational Methodology

Potential energy curves (PECs) have been calculated for the six B^+–RG complexes (RG = He—Rn) using CCSD(T) theory in MOLPRO.[1] Basis sets of both quadruple- and quintuple-ζ quality were employed, allowing the pointwise extrapolation of the energies to the basis set limit. More specifically, for boron the aug-cc-pCVXZ (X = Q, 5) basis sets were employed,[2] and for helium,[3] neon,[4] and argon,[5] aug-cc-pVXZ (the basis sets are henceforth abbreviated as aXZ, where X = quality of basis set). For krypton, xenon, and radon, aug-cc-pwCVXZ-PP weighted-core-valence basis sets were used along with the appropriate fully relativistic ECPs, ECP10MDF, ECP28MDF, and ECP60MDF respectively. The frozen core approximation was used for the 1s electrons of neon, and the 1s and 2s of argon; all other electrons outside of ECPs were included in the correlation treatment.

LeRoy's LEVEL code[6] was used to interpolate the PECs and to obtain rovibrational levels. Equilibrium bond lengths, R_e, and dissociation energies, D_e, were read off directly from the interpolated curves, and used along with the lowest rotational level and two lowest vibrational levels in standard Morse relationships to obtain the various spectroscopic constants which are discussed in this chapter.

Furthermore, additional analyses were undertaken in order to gain a deeper understanding of these systems. Contour plots of the Hartree-Fock orbitals have been produced at the CCSD(T)/a∞Z R_e, the visualisation

being performed with MOLDEN;[7] these contour plots are correlated with molecular orbital plots, the energies of which are taken from HF/aTZ calculations conducted again at the CCSD(T)/a∞Z R_e. Partial atomic charges were calculated from QCISD densities with triple-ζ basis sets of the same designation as those used for the PECs. Three separate methodologies were employed—Mulliken, NPA, and AIM (see Section 2.3). The local energy densities $H(r)$ from AIM analyses are also considered.

	R_e / Å	D_e / cm^{-1}	D_0 / cm^{-1}	ω_e / cm^{-1}	$\omega_e x_e$ / cm^{-1}	k / Nm^{-1}	$\frac{D_e{}^{\text{Morse}}}{D_e}$	Ref.
B^+–He	2.762	185	136	106.4	17.28	1.96	0.89	a
	2.912	∼175	∼140	87				8[b]
	2.875	∼190						9[c]
	2.636	∼140						10[d]
B^+–Ne	2.660	426	376	104.5	7.005	4.57	0.91	a
	∼3	∼160						11[e]
	2.23	∼1300		234	27.3			12[f]
	2.474	∼420	∼350	144				13[b]
	2.518							13[g]
	2.451	∼1260						10[d]
B^+–Ar	2.433	2390	2289	203.6	4.49	21.08	0.97	a
	∼3	∼730						11[e]
	∼2.8	∼2400						11[h]
	2.37	∼2800		274	24.0			12[f]
	2.738	∼1960	∼1890	112				13[b]
	2.427							13[g]
	3.145	∼420		78	3.1			14[i]
	2.489	∼1340						14[j]
	2.437	∼1420						15[k]
	2.590	∼2520						10[d]
B^+–Kr	2.424	4059	3933	252.2	3.70	36.47	1.06	a
	∼2.6	∼4000						11[h]
	2.635	∼4020						10[d]
B^+–Xe	2.516	6519	6372	296.6	2.96	52.67	1.14	a
	∼2.6	∼6800						11[h]
	2.713	∼6470						10[d]
B^+–Rn	2.556	8034	7878	314.6	2.64	61.15	1.17	a

[a] This work
[b] MP4(SDTQ) energetics calculated at an MP2 geometry, from Frenking *et al.*
[c] MP4(SDQ) from Simpson *et al.*
[d] B3LYP from Koskinen and Cooks
[e] HF from Ding *et al.*
[f] CI from Iwata and Sato
[g] MP4(SDTQ) from Frenking *et al.*
[h] Scattering experiment from Ding *et al.*
[i] CASSCF from Wong and Radom
[j] MP3 from Wong and Radom
[k] ST4CCD with empirical corrections, from Wong and Radom

Table 3.1: Spectroscopic constant for the B^+–RG series. R_e is the equilibrium bond length, D_e and D_0 are the equilibrium and zero point dissociation energies respectively, ω_e is the harmonic vibrational frequency, $\omega_e x_e$ is the anharmonicity constant, and k the force constant from Hooke's law. $D_e{}^{\text{Morse}}/D_e$ is calculated as outlined in Section 2.4.3.

3.2 Previous Studies

The spectroscopic constants that have been calculated are tabulated in Table 3.1. Several studies have been previously undertaken on the B^+–RG series by various means which are now compared to the CCSD(T) results.

3.2.1 B^+–He

Three previous studies can be found in the literature which present results for B^+–He, the oldest of which was published by Frenking *et al.* in 1989[8] using 2nd and 4th order Møller-Plesset perturbation theory. The MP2 R_e value is 0.15 Å (5 %) longer than the CCSD(T) results, and so in fairly poor agreement. However, the MP4 D_e and D_0 values (calculated at the MP2 geometry) are in quite good agreement with the present results. Another perturbation theory study, this time by Simpson *et al.*.[9] using MP4(SDQ) gives a bond length which is in slightly better agreement, and a D_e value which agrees well.

Finally, in 1999, Koskinen and Cooks[10] published a density functional theory study which includes results for R_e and D_e on B^+–He, –Ne, –Ar, –Kr, and –Xe. For B^+–He, the DFT bond length is seen to be in fairly poor agreement with that from CCSD(T). Similarly, their D_e value is in quite poor agreement, being only ∼75% of ours. DFT using the B3LYP functional (as in Ref. 10) giving energetics which are in poor agreement with full electronic structure calculations is not surprising; although B3LYP is widely used and often reliable when applied to strongly bound organic molecules, the fact that it does not adequately describe dispersion effects means it is of only limited use when applied to weakly bound systems such as the present case.

3.2.2 B^+–Ne

The earliest B^+–RG study is from 1978 by Ding *et al.*[11] using HF. The bond length from that study is much longer compared to this, and the binding energy much lower, likely due to the absence of dynamic correlation in HF.

A configuration interaction study from Iwata and Sato[12] gives a bond length which is much shorter than predicted by CCSD(T), by almost 0.5 Å. More notably, however, the D_e from that study is *considerably* higher, at three times the CCSD(T) value. The values presented for ω_e and $\omega_e x_e$ are similarly much larger.

Another Møller-Plesset theory study from Frenking *et al.*[13] gives an MP2 geometry which is much shorter than that from CCSD(T), and a harmonic frequency which is higher by almost 50%. An MP4(SDTQ) bond length from the same study is seen to be a little longer than that from MP2, but is still significantly shorter than the present result. The values for D_e and D_0 have been calculated using MP4(SDTQ) at the MP2 bond length, and are seen to be in rather good agreement with the CCSD(T) results, with D_e in particular being very similar.

The results from the Koskinen and Cook DFT study[10] have a bond length shorter than the one presented here, similar to their B^+–He results. In contrast to those results though, the binding energy is seen to be much higher than that from CCSD(T), and is in fact more in line with the very high D_e from the CI study. It is surprising that these studies present values for D_e which are in good agreement, but it should be noted that the CI study employed MIDI4* basis sets, which are minimal basis sets with added diffuse functions. As such, results from that study could be expected to give inferior results, and the agreement with the B3LYP result is likely coincidental.

3.2.3 B^+–Ar

Rather more results are available for the B^+–Ar complex. HF results from Ding *et al.*[11] show poor agreement with the present results, with a much longer bond length and much smaller D_e. That paper included not only HF calculations, however, but also results from scattering experiments for B^+–Ar, B^+–Kr, and B^+–Xe. The B^+–Ar experimental result gives a bond length which is notably longer than CCSD(T) calculations predict, but a D_e value which is in very good agreement.

The CI study by Iwata and Sato[12] gives a bond length which is in fairly poor agreement with the present results. As was seen for B^+–Ne, the D_e value is seen to be higher than the result from the present study, as are both ω_e and $\omega_e x_e$. However, in contrast to what was seen previously, the MP4(SDTQ)//MP2 results from Frenking *et al.*. presented a longer R_e than that from CCSD(T), and the D_e is seen to be in much poorer agreement than it was for B^+–Ne, now being smaller than that from CCSD(T). The MP4(SDTQ) bond length from the same study is seen to be in excellent agreement with the CCSD(T) value, however.

A CASSCF study by Wong and Radom[14] presents many constants for comparison. The CASSCF bond length is drastically longer than that from CCSD(T), in line with a dissociation energy which is far smaller. Similarly, the value presented for ω_e in that work is seen to be much lower; $\omega_e x_e$ is also seen to be less than that predicted here. All of these present a consistent picture of the strength of interaction predicted by CASSCF theory being much less than that predicted by CCSD(T). In the same study, MP3 results were also presented. These present an R_e which is in fair agreement with the present results, but the agreement for D_e is worse, with the MP3 result being around half that of the CCSD(T). Another study by Wong and Radom[15]

using ST4CCD theory (equivalent to CCD(ST)) gives results that are seen to be in good agreement with their earlier MP3 results, and are consequently in poor agreement with the CCSD(T) calculations.

The DFT calculations by Koskinen and Cook[10] are in fair agreement for the B^+–Ar complex, with a slightly longer bond length and a slightly elevated dissociation energy compared to CCSD(T).

3.2.4 B^+–Kr, B^+–Xe, and B^+–Rn

In contrast to the lighter members of the series, very few studies have examined the heavier three complexes, B^+–Kr, B^+–Xe, and B^+–Rn. Only two sets of results are available for comparison for each of B^+–Kr and B^+–Xe; B3LYP calculations by Koskinen and Cooks[10], and the the scattering study from Ding *et al.*[11]

For both studies, R_e is seen to be rather longer than the present calculations would predict. For B^+–Kr, the D_e values are seen to be in good agreement, especially for the B3LYP results. B^+–Xe compares less favourably, with the B3LYP result being in fair agreement with the CCSD(T) results, and the scattering experiment giving a somewhat higher value.

In the case of B^+–Rn, there are seemingly no previous results available for comparison in the literature, and consequently the values here are the first such available.

3.3 Trends in Spectroscopic Constants

As the atomic number of the rare gas increases, the series shows a trend of increasing D_e. Several effects will be felt in the complex; the increasing number of electrons will lead to an increase in the strength of the electronic repulsion interaction, but as the total binding energy is seen to increase this

effect is evidently outstripped by increases in the attractive terms. The chief increase in attractive terms will originate from the ion/induced-dipole (IID) interaction, as this term exhibits a dependency on the polarisability of the rare gas, α_{RG}. Heavier elements in Group 18 possess higher polarisabilities, and consequently this term will increase as the group is descended. Since the highest interaction energy is seen for B^+–Rn despite the minimum R_e being at B^+–Kr, it would seem that the lengthening of equilibrium internuclear separation is not as important as the increasing α_{RG} despite the $1/R^4$ dependence of the IID interaction. Further to this, the increasing bond length will give a reduction in the repulsive interaction throughout the series. Of note is the overall magnitude of D_e for the heavier complexes in this series, which are surprisingly strongly bound for rare gas complexes.

The trend in R_e exhibits a decrease from B^+–He to B^+–Kr, and then a slight increase through to B^+–Rn. The equilibrium internuclear separation is a result of the different R dependencies of the attractive and repulsive forces between the two centres. As discussed above, both the electronic repulsion and IID forces will increase as Group 18 is descended, but from the non-monotonic trend in R_e it is clear that these forces do not increase at the same rate. Initially, the increase in the IID term is more important as seen from the decreasing bond lengths, but after B^+–Kr the bond begins to lengthen. This would imply that the repulsion term is now increasing more rapidly than the IID; the total interaction energy D_e continues to increase however, showing that the attractive terms are still greater in magnitude.

Values for the harmonic vibrational frequency ω_e are also seen to give a general increase across the series. One exception to this trend arises, as the vibrational frequency drops from B^+–He to B^+–Ne, but ω_e is affected not only by the strength of interaction between the atoms, but also by the masses of the atoms. In order to remove this mass dependency, the force

constant k is considered. As can be seen in Table 3.1, the value of k rises monotonically as Group 18 is descended, in line with the monotonic rise in total binding energy.

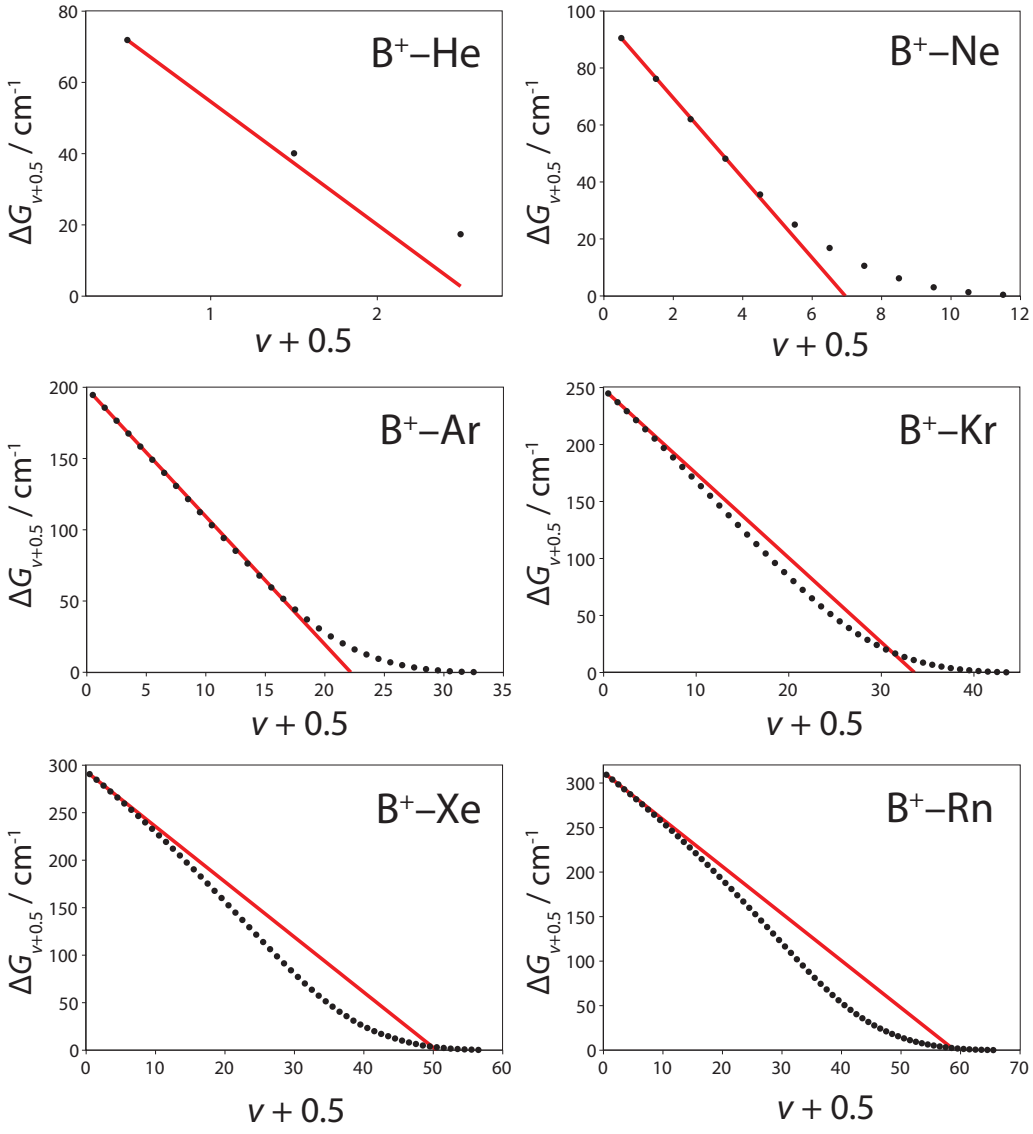


Figure 3.1: Birge-Sponer plots for the B^+–RG series. The lines plotted are linear extrapolations from the first two points, and represent Morse-like behaviour.

3.4 D_e^{Morse}/D_e Ratios and Birge-Sponer Plots

The values for D_e^{Morse}/D_e provide a good measure for how Morse-like a complex behaves, as discussed in Section 2.4.3. The present series of

complexes show values of less than unity for RG = He and Ne, around one for RG = Ar and Kr, and greater than one for RG = Xe and Rn.

Additionally, Birge-Sponer plots have been produced for these complexes and are shown in Figure 3.1. Superimposed on the Birge-Sponer plots are 'Morse lines' to indicate ideal Morse-like behaviour, which are essentially linear extrapolations of the first two points on each plot. Points on the curve at which the 'real' values deviate from this line indicate deviations from ideal Morse-like behaviour, as will be discussed below.

Although there are very few points for B^+–He, the plotted points are seen to depart immediately from linear behaviour, and thus give a low value for ${D_e}^{\mathrm{Morse}}/D_e$. B^+–Ne does follow the Morse line for the most part, with a 'tail' to high v also giving a result for ${D_e}^{\mathrm{Morse}}$ less than the true D_e.

The heavier complexes show more interesting deviations, with each of the plots dipping below the Morse line for moderate values of v, and then turning to intercept the x-axis. This effect is just barely observable in B^+–Ar, and is more apparent for B^+–Kr as seen in Figure 3.1. From this it can be deduced that the close to unity values of the ${D_e}^{\mathrm{Morse}}/D_e$ ratios for B^+–Ar and B^+–Kr are due to the different deviations cancelling out to give a total well depth close to that predicted by the Morse model from the lowest few vibrational levels. This demonstrates that when assessing how Morse-like a species behaves, it is important to consider the full potential instead of using only ${D_e}^{\mathrm{Morse}}$.

For B^+–Xe and B^+–Rn, the plotted points are seen to fall below the Morse line for a significant range of v. The number of points which are below the line are now more important than the 'tail' above the line at high v, which is now much smaller. Due to this, the ${D_e}^{\mathrm{Morse}}/D_e$ ratio becomes greater than unity.

3.5 Reduced Potential Plots

Reduced potential plots are presented in Figure 3.2. In order to create these plots for each complex, the interaction energy and internuclear separation of each point from the *ab initio* curve has been divided by the equilibrium dissociation energy and the equilibrium bond length respectively. Through this treatment, the PECs are essentially 'normalised' by their equilibrium parameters, facilitating a more direct comparison between individual PECs.

Immediately striking is the fact that the PECs fall very neatly into two groups; the top two plots, B^+–He and B^+–Ne, and the bottom four which correspond to the four heavier species. Within these groups, the PECs show very similar shapes. The correspondence between helium and neon can be explained by the relative polarisabilities; although the size of a neon

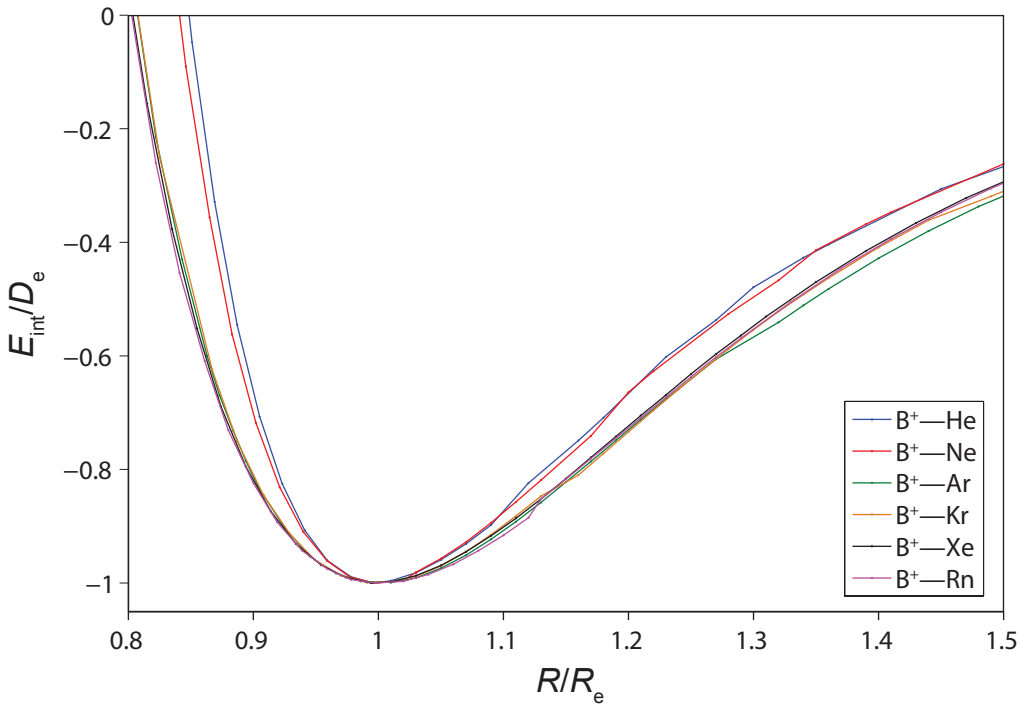


Figure 3.2: Reduced potential plots for the B^+–RG series. For each point of the *ab initio* potential, the internuclear separation R has been divided by R_e, and the interaction energy E_{int} has been divided by D_e of the respective species.

atom is larger than that of helium, the polarisability for each is very low, especially when considered in the larger framework of the relative sizes and polarisabilities of Group 18. Consequently, neon species are often seen to behave more similarly to analogous helium species than would perhaps be anticipated.[16] The heavier rare gases show more consistency in the relative IID and repulsion terms, leading to similarly shaped potentials.

These similarities are in line with the overall form of the two types of potential seen here. The lighter species are seen to possess a potential with a narrower potential well, corresponding to a less polarisable electron cloud. For the heavier four complexes, the electron density on the rare gas is seen to be more polarisable and 'softer', manifesting in a wider potential well with a repulsive wall starting at shorter R.

3.6 Molecular Orbital Diagrams and Orbital Contour Plots

Hartree-Fock calculations have been conducted at the CCSD(T)/a∞Z R_e value, and contour plots of the resultant orbitals have been plotted and are shown along with a corresponding MO diagram (the energies of which are taken from calculations at the same level of theory) in Figures 3.3 through 3.6.

3.6.1 Li^+–He

As a reference point for the molecular orbital diagrams and orbital contour plots, in addition to the diagrams for the B^+–RG series a plot has been produced for Li^+–He as shown in Figure 3.3. Previous research on this complex has shown the interactions to be almost completely electrostatic, 'physical' type interactions.[17] In that study, spectroscopic parameters for

the complex were fitted to a 'model potential' which included terms for the ion/induced-dipole, -quadrupole, and -octupole interactions, as well as dispersion and electronic repulsion. From this fit, an effective charge Z is found for the metal ion; if Z is found to be close to unity then these electrostatic interaction terms alone are found to be sufficient to describe the interaction. Li^+–He yielded a Z value of 1.03, and as such the interactions can be well explained in terms of physical interactions.

From the plotted energy levels, the He 1s orbital is seen to have lowered in energy in the complex (as orbital ϕ_1) due to Coulombic interactions with the nearby metal cation. Furthermore, the plotted contours show the form

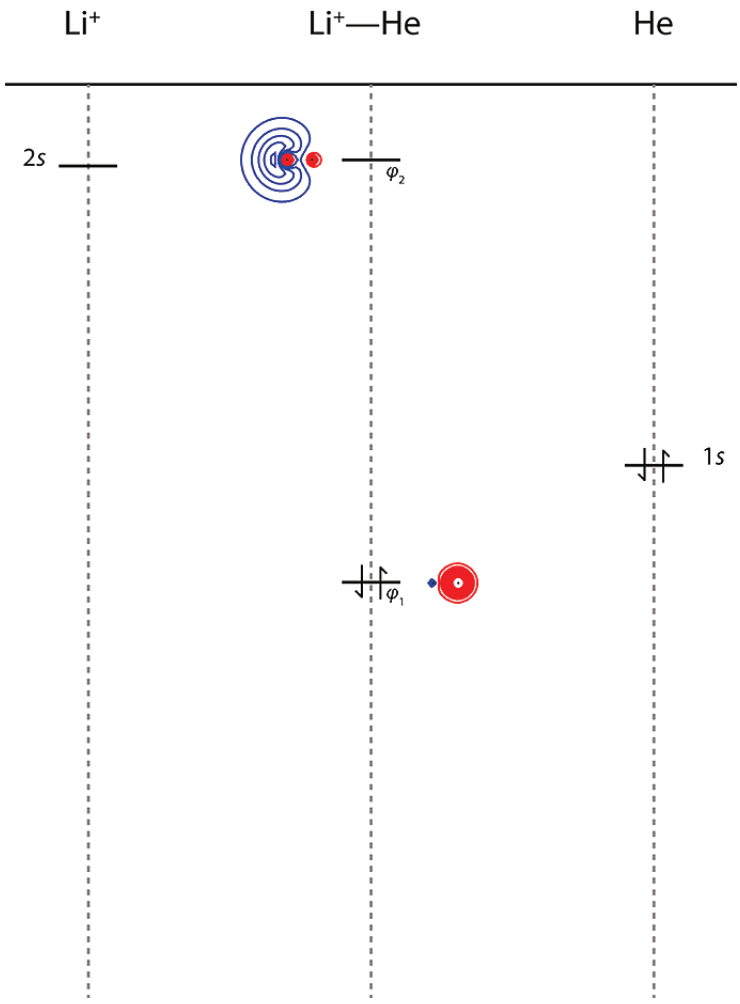


Figure 3.3: MO diagram for the Li^+–He complex. The energy levels and the contours are taken from a HF calculation using the CCSD(T)/a∞Z R_e value.

of the He 1s orbital to be largely preserved in the complex, with almost all of the orbital density being located on the helium atom. Some perturbation to the virtual Li^+ 2s orbital can be seen in ϕ_2, but since this orbital is unoccupied and the energy has not changed upon complexation, this should not influence the form of interaction significantly. As the binding energy of Li^+–He is quite low at 659 cm^{-1}, the extent of the Coulombic stabilisation is evidently largely counteracted by repulsive interactions.

3.6.2 B^+–He and B^+–Ne

Figure 3.4 shows the MO diagrams for the two lightest members of the B^+–RG series. For B^+–He, it can be seen that perturbation to the atomic orbitals is minimal. The energy of the B^+ 2s orbital remains unaffected upon complexation. The Coulombic stabilisation of the He 1s orbital is seen again, and is observed for all rare gas orbitals upon complexation throughout the series.

The orbital contours show very little perturbation, with ϕ_1 corresponding to the atomic helium 1s and ϕ_2 being the boron 2s. Very small contributions are seen to arise from the 'other' centre, but these effects are extremely slight, similarly to Li^+–He. Additionally, the virtual B^+ 2p orbitals are seen to remain as essentially degenerate, with no orbital density located on the rare gas atom for ϕ_3 and ϕ_4, and only a small amount for ϕ_5 (the virtual B^+ $2p_z$ orbital). Overall, the energetics and contours in this diagram are seen to be quite similar to those of Li^+–He, showing that this boron complex is quite 'physical' in nature.

B^+–Ne presents a similar picture—again, contours of the complex orbitals show the same localisation to a single centre for all ϕ, with only minor contributions arising from the other centre. The boron orbitals do not move in energy, and there is the same slight stabilisation effect seen in the rare gas

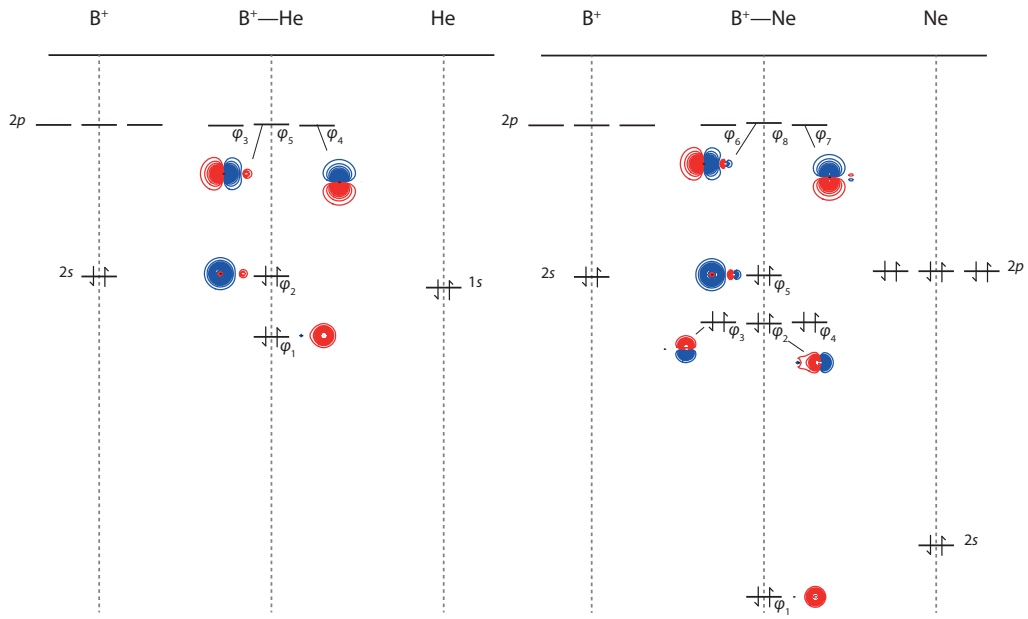


Figure 3.4: MO diagram for the B^+–He and B^+–Ne complexes. The energy levels and the contours are taken from a HF calculation using the CCSD(T)/a∞Z R_e value.

orbitals due to Coulombic interactions. It should be noted that although the Ne $2p_z$ orbital initially appears to show significant distortion, this effect is represented by only a single contour and as such is almost negligible.

3.6.3 B^+–Ar and B^+–Kr

Figure 3.5 shows the diagrams for the B^+–Ar and B^+–Kr species. These species both show a notable departure from Li^+–He and the two lighter boron complexes, with orbital energies changing more significantly upon complexation. For B^+–Ar, although the Ar 3s orbital is low enough in energy to remain non-interacting and is preserved in the complex as ϕ_1, the former B^+ 2s atomic orbital (ϕ_2 in the complex) has lowered in energy, and the contour plot now shows more significant contributions from both centres as some Ar $3p_z$ character is mixed in. This effect is echoed in the Ar 3p orbitals, which are now seen to become non-degenerate. Although the $3p_x$ and $3p_y$ orbitals remain degenerate and localised entirely to the Ar atom as complex orbitals ϕ_3 and ϕ_4, the $3p_z$ interacts with the B^+ 2s to form

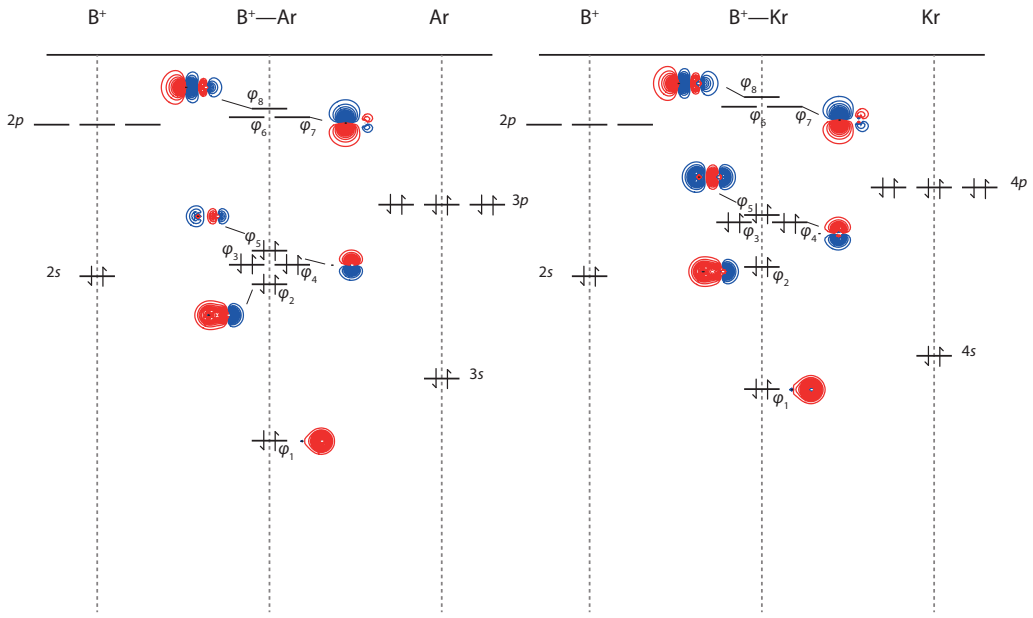


Figure 3.5: MO diagram for the B^+–Ar and B^+–Kr complexes. The energy levels and the contours are taken from a HF calculation using the CCSD(T)/a∞Z R_e value.

ϕ_5 which is higher in energy than the others. Due to the forms of their contours and their relative energetics, ϕ_2 and ϕ_5 appear to correspond to a traditional σ bonding and σ^* antibonding pair of orbitals arising from interactions between the atomic B^+ 2s and Ar $3p_z$ orbitals.

The virtual B^+ 2p orbitals are also seen to split in degeneracy as ϕ_6, ϕ_7, and ϕ_8 in the complex. All three have moved up in energy, but the B^+ $2p_z$ (ϕ_8) more so. These orbitals also exhibit some contributions from Ar p_x, p_y, and p_z atomic orbitals according to symmetry.

The B^+–Kr complex appears very similar to B^+–Ar. Mixing of atomic orbitals to form the orbitals in the complex is more exaggerated here, although the split in degeneracy of the Kr $4p_{x,y}$ and $4p_z$ orbitals ($\phi_{3,4}$ and ϕ_5 in the complex) is less here, due to the greater energetic separation between the atomic B^+ 2s and rare gas valence np orbitals compared to those of B^+–Ar.

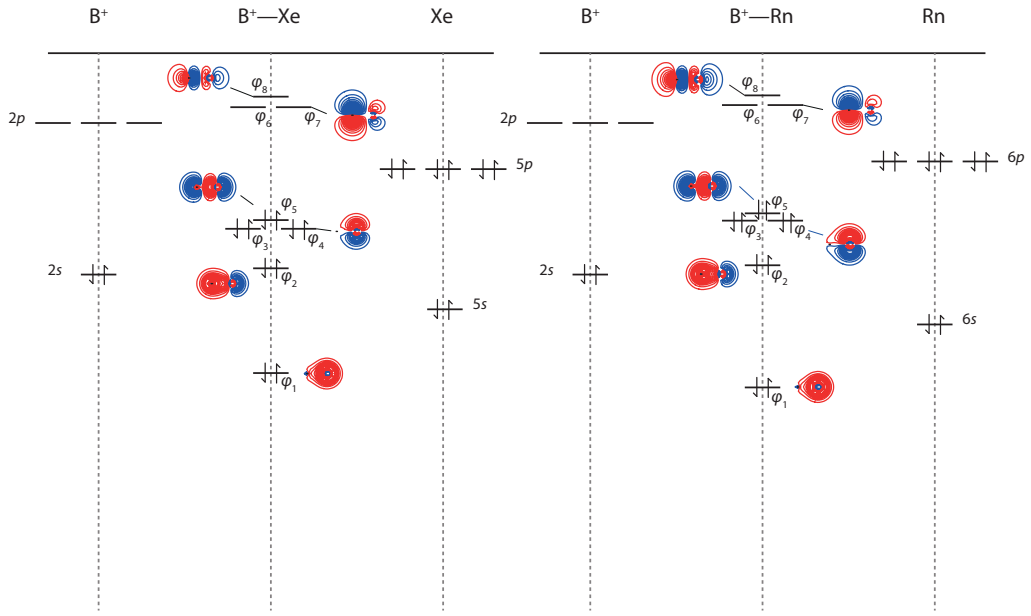


Figure 3.6: MO diagram for the B^+–Xe and B^+–Rn complexes. The energy levels and the contours are taken from a HF calculation using the CCSD(T)/a∞Z R_e value.

3.6.4 B^+–Xe and B^+–Rn

For the heaviest two complexes, B^+–Xe and B^+–Rn, shown in Figure 3.6, the behaviour of the orbitals upon complexation is largely the same as for the argon and krypton complexes, with heavy mixing of the atomic B^+ 2s and rare gas valence np orbitals in the complex. B^+–Xe shows a significant distortion of the atomic Xe 5s orbital in ϕ_1 as it becomes polarised by the nearby cation. ϕ_5, corresponding to the σ^* antibonding orbital, shows a more poorly defined nodal plane between the two atoms as destructive inteference between components of atomic orbitals with opposite signs of the wavefunction leads to depletion of orbital density in the internuclear region.

B^+–Rn shows the same behaviour as B^+–Xe. Again, the rare gas valence ns orbital shows significant distortion upon complexation. Depletion of orbital density in the internuclear region in ϕ_5 is more pronounced now, allowing favourable interaction between orbital components of the same phase.

3.7 Partial Charge Analyses

The results of the partial atomic charge analyses are collected in Table 3.2. The magnitude of charge on the rare gas atom is different depending on which methodology is used. When Mulliken population analysis is applied, the charge transfer is much higher than for the other two methods used here, being around twice the magnitude in all cases. As Mulliken population analysis is known to be unreliable as discussed in Section 2.3.1, and NPA and AIM are seen to be in much better agreement with each other, more weight is given to the latter two sets of results.

For all three methodologies, the partial charge on the rare gas atom for the B^+–He and B^+–Ne systems is negligible. Upon moving to B^+–Ar, the charge localised to the rare gas increases, with a similar increase seen for B^+–Kr and B^+–Xe. B^+–Rn shows a comparable charge on the rare gas to B^+–Xe.

These increases in partial atomic charge are thus seen to be monotonic throughout the group. This agrees with the trend in increasing orbital delocalisation across both centres seen from the contour plots. As such, the charge transfer effect seen here could be a consequence of incipient covalent bond formation.

		B^+–He	B^+–Ne	B^+–Ar	B^+–Kr	B^+–Xe	B^+–Rn
Q_{RG}	Mulliken	0.00	0.02	0.16	0.29	0.49	0.60
	NPA	0.00	0.01	0.08	0.16	0.30	0.34
	AIM	0.00	0.00	0.08	0.16	0.27	0.33
	$H(r)$	0.0013	0.0009	-0.0069	-0.0141	-0.0180	-0.0189

Table 3.2: Partial atomic charge analysis for the B^+–RG series in units of elementary charge e, and local energy density $H(r)$ from AIM analysis in atomic units. Q_{RG} is the partial atomic charge ascribed to the rare gas atom, and the corresponding charge on boron may be found as $+(1 - Q_{RG})$.

3.8 Local Energy Density $H(r)$

The local energy density $H(r)$ from AIM analysis provides an additional criterion by which one may judge the covalency of a system. Should $H(r)$ return a value which is negative, then a system can be considered as having at least partial covalent character.[18] The results of this anaylsis are presented along with the partial atomic charges in Table 3.2.

For both B^+–He and B^+–Ne, $H(r)$ is positive and so interactions can be considered as purely electrostatic. The heavier members of the series, however, all exhibit a negative value of $H(r)$ and as such may be considered to contain at least a small amount of covalency. This finding is in line with the orbital contour plots, in which the form of ϕ_2 was seen to change significantly between B^+–Ne and B^+–Ar, with neon exhibiting almost pure 2p orbitals and the argon complex (and the heavier complexes) possessing an orbital which demonstrates significant delocalisation of orbital density over both centres.

The magnitude of $H(r)$ is seen to increase down the series, in line with increasing amounts of orbital delocalisation seen as Group 18 is descended. As the 'shared' electronic density is more stabilised (i.e. a more negative $H(r)$), then the extent of covalency is seen to increase in the contour plots.

3.9 Conclusions

Counterpoise-corrected PECs have been calculated for the B^+–RG series at the CCSD(T) level of theory and extrapolated to the basis set limit. For the heavier rare gases, D_e is found to be significant, reaching over 8 000 cm^{-1} for B^+–Rn.

Inspection of contour plots and energetics of orbitals in the complexes

reveals that for B^+–Ar—B^+–Rn there is significant delocalisation of orbital density over both centres, along with the formation of a σ and σ^*, bonding and antibonding pair of orbitals. Partial atomic charge analysis has placed a significant positive charge on the rare gas in these cases, consistent with perturbation to the atomic orbitals upon complex formation. Additionally, the $H(r)$ parameter from AIM theory finds covalent character for these four heavier complexes.

The two lighter complexes B^+–He and B^+–Ne show no such effects, with negligible charge on the rare gas, preservation of atomic-like orbitals in the complex, and no covalency predicted from $H(r)$. Consequently, these two complexes are considered entirely 'physical' in nature, whilst the heavier members of the series possess partial covalent character.

Bibliography

[1] H.-J. Werner, P. J. Knowles, G. Knizia, F. R. Manby, M. Schütz *et al.*, MOLPRO , version 2012.1, a package of ab initio programs, 2012, see http://www.molpro.net.

[2] D. E. Woon and T. H. Dunning, *The Journal of Chemical Physics*, 1995, **103**, 4572–4585.

[3] D. E. Woon and T. H. Dunning, *The Journal of Chemical Physics*, 1994, **100**, 2975–2988.

[4] T. H. Dunning, *The Journal of Chemical Physics*, 1989, **90**, 1007–1023.

[5] D. E. Woon and T. H. Dunning, *The Journal of Chemical Physics*, 1993, **98**, 1358–1371.

[6] R. J. LeRoy, Level 8.0: A Computer Program for Solving the Radial Schrödinger Equation for Bound and Quasibound Levels, University of Waterloo Chemical Physics Research Report No. CP-663, 2007; see http://leroy.uwaterloo.ca/programs/.

[7] G. Schaftenaar and J. H. Noordik, *Journal of Computer-Aided Molecular Design*, 2000, **14**, 123.

[8] G. Frenking, W. Koch, D. Cremer, J. Gauss and J. F. Liebman, *The Journal of Physical Chemistry*, 1989, **93**, 3397–3410.

[9] R. Simpson, P. Harland, R. Maclagan, D. Smith and N. Adams, *International Journal of Mass Spectrometry and Ion Processes*, 1989, **90**, 193–196.

[10] J. T. Koskinen and R. G. Cooks, *The Journal of Physical Chemistry A*, 1999, **103**, 9565–9568.

[11] A. Ding, J. Karlau, J. Weise, J. Kendrick, P. J. Kuntz, I. H. Hillier and M. F. Guest, *The Journal of Chemical Physics*, 1978, **68**, 2206–2213.

[12] S. Iwata and N. Sato, *The Journal of Chemical Physics*, 1985, **82**, 2346–2351.

[13] G. Frenking, W. Koch, D. Cremer, J. Gauss and J. F. Liebman, *The Journal of Physical Chemistry*, 1989, **93**, 3410–3418.

[14] M. W. Wong and L. Radom, *The Journal of Physical Chemistry*, 1989, **93**, 6303–6308.

[15] M. W. Wong and L. Radom, *The Journal of Physical Chemistry*, 1990, **94**, 638–644.

[16] F. Grandinetti, *Nature Chemistry*, 2013, **5**, 438.

[17] W. Breckenridge, V. L. Ayles and T. G. Wright, *Chemical Physics*, 2007, **333**, 77 – 84.

[18] D. Cremer and E. Kraka, *Angewandte Chemie International Edition in English*, 1984, **23**, 627–628.

Chapter 4

Interactions in RG–H^- (RG = Rare Gas) and MH^- (M = Group 2 Metal) Species

Although chemical intuition can lead to succesful prediction of some properties of a system, this is not always true. In the case of BeH^-, consideration of relative electronegativities and electron affinities shows that the excess negative charge will reside on the hydrogen. Consequently, this system consists of two closed shell, ^1S constituents, and as such the overall form of interaction could be expected to be essentially electrostatic in nature, with a low binding energy. This viewpoint is further bolstered by isoelectronic arguments; the hydrogen anion has the same electronic structure as a helium atom. Consequently, the form of the interaction could be expected to be entirely non-covalent, and weakly bound.

However, a publication by Verdicchio *et al.* from 2013[1] showed that this was not the case. In that paper, the interatomic potential was evaluated using full CI theory and very large Dunning-style basis sets, yielding an equilibrium dissociation energy of over 2 eV.

This chapter explores the interactions in this somewhat unusual species in an attempt to rationalise exactly why the binding energy initially seems anomolously high. Additionally, the investigation is extended to include

analogous complexes incorporating the heavier elements of Group 2, MH^-, where M = Mg, Ca, Sr, Ba, and Ra. As a prelude to these systems, the related series of rare gas hydrides RG–H^- will be considered, which similarly consist of two closed shell, ^1S substituents.

4.1 Computational Methodology

Potential energy curves were calculated for the RG–H^- and MH^- series using CCSD(T) theory as implemented in the MOLPRO software package.[2] A wide range of internuclear seperations were sampled to account for short, medium, and long range interactions, covering the strong repulsive wall at very short R, and out to ∼30 Å. Basis sets of both quadruple- and quintuple-ζ quality were employed to facilitate the pointwise extrapolation of the potentials to the basis set limit. These basis set extrapolated PECs were then used as input to the LEVEL 8.0 code of LeRoy[3] in order both to interpolate the curves for a more accurate determination of R_e and D_e, as well as to calculate rovibrational energy levels. Standard Morse relationships can then be applied to these values in order to calculate more spectroscopic parameters (see Section 2.4.3).

The basis sets used for hydrogen were aug-cc-pVXZ (where X = Q, 5). For Be and Mg the all-electron aug-cc-pwCVXZ basis sets[4] were used. The heavier metals Ca, Sr, Ba, and Ra used ECPXXMDF pseudopotentials, where XX = 10, 28, 46, and 78 respectively,[5,6] along with the corresponding aug-cc-pwCVXZ-PP basis sets. By use of these fully relativistic ECPs, relativistic effects present in these heavier elements are accounted for.

For the rare gases, aug-cc-pVXZ basis sets were used for He, aug-cc-pwCVXZ for Ne and Ar, and aug-cc-pwCVXZ-PP for Kr, Xe, and Rn. Again, ECPs were used for the heavier elements of this series in the form of ECP10MDF, ECP28MDF, and ECP60MDF for Kr, Xe, and Rn respectively.

In addition to the PECs being calculated, additional analyses were conducted at the CCSD(T) R_e using QCISD wavefunctions. Partial atomic charges were calculated by Mulliken, NPA and AIM methodologies. $H(r)$ values were also extracted from the AIM analysis to help classify the bonding character, and NBO data has been examined with a similar aim. Finally, contour plots of the natural orbitals have been plotted for the HOMO and HOMO-1 (i.e. the orbital energetically 'below' the HOMO) for selected complexes using MOLDEN.[7] All of these analyses have been undertaken using basis sets corresponding to those stated above, but of triple-ζ quality.

4.2 Rare Gas Hydride Complexes

4.2.1 Previous Studies

Few studies exist in the literature for the RG–H^- series, and those that do are almost exclusively focussed on He–H^-. A 1998 study from Shalabi *et al.*[8] calculated PECs for He–H^- using QCISD(T) theory, both with and without bond centered functions; however, as these PECs consisted of no more than 20 points and were not interpolated, these parameters can hardly be considered 'equilibrium' and it is difficult to draw any conclusions as to how comparable any derived spectroscopic constants are to the present results. A 1997 study by Bendazzoli *et al.*[9] conducted primarily with full configuration interaction theory is found to be in fair agreement with the present results; in the same paper, CCSD(T) calculations were also carried out, the results of which are very close to those from the FCI.

In 2001, a study from Vallet *et al.* provided not only results for He–H^- with which to compare, but also Ne–H^- and Ar–H^-, all conducted using CCSD(T) theory.[10] In all cases, the dissociation energies are seen to be in good agreement with the present values for D_e, but the values of R_e do not

agree very well. These differences are not systematically longer or shorter.

There are no other studies in the literature for the three heavier rare gas species Kr–H^-, Xe–H^-, and Rn–H^-, with the values calculated here being seemingly the first for these three complexes.

4.2.2 Geometric Parameters

Derived spectroscopic parameters for the RG–H^- series are presented in Table 4.1. As shall be outlined in the following sections, these complexes are characterised by weak interactions, especially for the lightest two complexes He–H^- and Ne–H^-. The bond length for He–H^- in particular is extremely long, at almost 7 Å. Monotonically decreasing values of R_e are seen as group 18 is descended, contradicting the notion that the larger rare gas atoms would force the hydrogen anion out to longer internuclear seperation. Rather, it

	R_e / Å	D_e / cm^{-1}	D_0 / cm^{-1}	ω_e / cm^{-1}	$\omega_e x_e$ / cm^{-1}	k / Nm^{-1}	Ref.
HeH^-	6.871	3.9	0.7				This work
	6.652	3.7	0.5	9.047			10[a]
	∼7.9	∼2.4					8[b]
	∼5.3	∼23					8[c]
	6.826	3.17					9[d]
	6.821	3.23					9[e]
NeH^-	4.471	32.4	16.8				This work
	4.617	26.9	13.4	31.5			10[a]
ArH^-	3.784	275.0	217.0	124.0	15.96	0.89	This work
	3.058	272.8	215.9	120.9			10[a]
KrH^-	3.642	491.9	412.4	167.4	16.84	1.64	This work
XeH^-	3.626	789.8	690.4	206.8	15.97	2.52	This work
RnH^-	3.466	1170.6	1046.6	256.2	16.59	3.88	This work

[a] CCSD(T) from Vallet *et al.*
[b] QCISD(T) without bond functions, from Shalabi *et al.*
[c] QCISD(T) with bond functions, from Shalabi *et al.*
[d] FCI corrected for BSSE, from Bendazolli *et al.*
[e] CCSD(T) from Bendazzoli *et al.*

Table 4.1: Spectroscopic parameters for the RG–H^- series. R_e is the equilibrium bond length, D_e and D_0 are the equilibrium and zero point dissociation energies respectively, ω_e is the harmonic vibrational frequency, $\omega_e x_e$ is the anharmonicity constant, and k the force constant from Hooke's law.

would seem that as the interaction between RG and H^- becomes stronger down group 18 owing to the increasing polarisability of the heavier rare gases, there is an increasing impetus for the two centres to draw closer together; in this way, the strength of the ion/induced-dipole interaction is increased with its inverse dependence on R.

XH^-	$\alpha_d X$ / $a_0{}^3$	$\frac{-\alpha_d}{2R^4}$ / cm^{-1}	$\frac{IID}{D_e}$
HeH^-	1.38	5.34	1.36
NeH^-	2.66	57.30	1.77
ArH^-	11.08	464.75	1.69
KrH^-	16.77	820.19	1.67
XeH^-	27.29	1358.61	1.72
RnH^-	35.77	2132.38	1.82
BeH^-	37.79	82 042	5.12
MgH^-	74.91	54 204	4.55
CaH^-	161.96	71 254	4.53
SrH^-	186.25	61 328	3.97
BaH^-	267.91	74 952	4.28
RaH^-	258.46	59 754	4.15

Table 4.2: Ion/induced-dipole terms for the XH^- complexes. α_d is the polarisability of the metal or rare gas atom X, $-\alpha_d/2R^4$ is the ion/induced dipole interaction term, and IID/D_e is the ratio of the ion/induced-dipole to the equilibrium dissociation energy.

4.2.3 Dissociation Energies

In line with the long equilibrium internuclear seperations, the D_e values are seen to be quite low across the series. Once again, this is particularly notable for the two lightest complexes, with the binding energy of the helium complex being only 3.9 cm^{-1}. In fact, for both the helium and neon complexes, once zero point effects are taken into account, the potential well does not support vibrational levels above $v = 0$, and as such no data is presented for ω_e or any other spectroscopic parameter which considers excited vibrational levels. As the group is descended the number of bound vibrational levels increase, with Ar–H^- having 6, Kr–H^- 7, Xe–H^- 10, and Rn–H^- 11.

The binding energies are seen to increase monotonically as Group 18 is descended, in line with the shortening bond lengths. To quantify the importance of the ion/induced-dipole (IID) interaction in these systems, the

terms have been calculated and are presented in Table 4.2. It can be seen that, with the exception of HeH^-, the ratio between the ion/induced-dipole and equilibrium binding energy is fairly consistent, the implication being that the form of interaction is the same down the group. Helium's polarisability is the lowest of all the rare gases, and consequently the magnitude of the IID force would be expected to be lowest for that complex. It should also be noted that the magnitude of the IID interaction is higher than the binding energy of these complexes in all cases, meaning that electronic repulsion is also playing an important role in the determination of the equilibrium parameters.

4.2.4 Partial Atomic Charges

The results of the partial atomic charge analyses are collected in Table 4.3. The partial charge located on the rare gas is indicative of any charge transfer between the two centres. Some minor movement of charge is not unexpected for the heavier rare gases owing to their increased polarisabilities, and this is what is observed from the present results. All three methodologies employed here give results for the RG–H^- series which are essentially in agreement as regards magnitude, with some slight variations.

Mulliken analysis predicts a positive charge on the rare gas, which seems quite surprising; however, it is generally accepted that Mulliken populations

	HeH^-	NeH^-	ArH^-	KrH^-	XeH^-	RnH^-
Mulliken	0.00	0.00	0.02	0.02	0.02	0.01
NPA	0.00	0.00	0.00	0.00	-0.01	-0.01
AIM	0.00	-0.01	-0.03	-0.05	-0.06	-0.08
	BeH^-	MgH^-	CaH^-	SrH^-	BaH^-	RaH^-
Mulliken	-0.990	-0.711	-0.355	-0.266	-0.205	-0.202
NPA	-0.345	-0.219	-0.180	-0.160	-0.178	-0.153
AIM	-0.060	-0.104	-0.117	-0.113	-0.178	-0.109

Table 4.3: Partial atomic charge analysis for the RG–H^- and MH^- series in units of elementary charge *e*. For RG–H^- the charge on the RG atom is considered, and for MH^- the charge on M.

are known to give inaccuracies in many systems. The NPA and AIM results both ascribe a small and negative charge to the rare gas atoms, with the size of this charge increasing as Group 18 is descended, in line with increasing polarisabilities. AIM gives a slightly higher charge transfer than NPA, although this reaches a maximum of only -0.08 e for Rn–H$^-$. Overall, it would appear that the form of interaction in these complexes entails no sharing of electrons, i.e. total non-covalency.

Another value which can be obtained from AIM analysis is the $H(r)$ parameter, which is considered to be a direct test of covalency in a system, and one which is particularly suited to cases with only slight covalency. If the sign of this value is negative, then the system is considered as having some covalent character[11] (see Section 2.3.3)—for the present series of complexes this is not true, with a positive value for $H(r)$ at the BCP for all complexes. This analysis reinforces the above findings: with weak interaction energies, long bond lengths, negligible charge transfer, and positive $H(r)$ values, these complexes appear to be clear cut cases of 'physical' type interactions, with the constituents interacting in a manner typical of closed shell species.

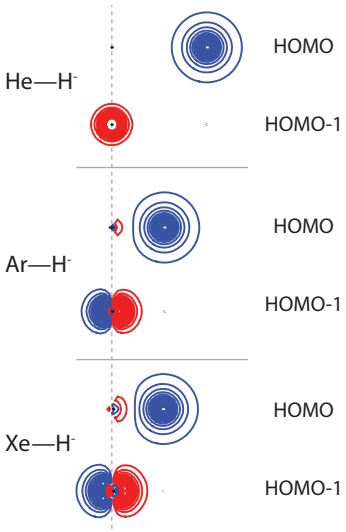


Figure 4.1: Natural orbital contour plots for selected members of the RG–H$^-$ series.

4.2.5 Orbital Contour Plots

Natural orbital contour plots of the HOMO and HOMO-1 are displayed for the He–H^-, Ar–H^-, and Xe–H^- complexes in Figure 4.1. Overall, the form of these contours is seen to be highly atomic in nature, especially so for the helium complex. The HOMO is seen to correspond to the 1s orbital of the hydrogen anion, with very slight contributions from the outermost occupied rare gas p_z-orbital for Ar– and Xe–H^-. Additionally, the outermost contours of the hydrogen density in these cases is slightly distorted by the nearby rare gas atom, but both of these effects are very slight and the orbitals are essentially atomic. Again, this corresponds to 'physical'-type interactions, with negligible perturbation to the electronic structure of the atomic constituents.

4.3 Metal Hydride Complexes

4.3.1 Multireference Calculations

Focus is now turned to the MH^- series. As the BeH^- system seems to exhibit unusual properties, the possibility of multireference behaviour in the MH^- series should be addressed before a full discussion. The T_1 diagnostics were collected for the six species, and although the value for BeH^- fell below the commonly accepted threshold of 0.02, the other members of the series were found to have values at or above this as listed in Table 4.4. As such, CASSCF + MRCI calculations were undertaken including the Davidson correction and using quintuple-ζ basis sets to examine the BaH^- potential (which was found to have the greatest value of T_1 at 0.049).

A PEC was calculated and the spectroscopic parameters from this were found to compare favourably with those from the CCSD(T)/aug-cc-pwCV5Z-

PP PEC, with the MRCI+Q R_e of 2.349 Å being only 0.007 Å greater than the CCSD(T) value. The values for D_e are also in good agreement, with the MRCI+Q result of 16 813 cm^{-1} being only 3 % less than the CCSD(T)/a5Z value.

Table 4.4 examines these differences in more depth through comparison of the binding energies from the various levels of theory employed, all calculated at the CCSD(T)/a∞Z R_e. The difference between the CCSD(T) and MRCI+Q levels is seen to be quite small across the series. As such, the contribution of multireference nature to the present species is seen to be very small at the minimum of the potential well, and as such use of a single reference method seems justified. It is also of note that the binding energies from QCISD theory are seen to agree quite well with the CCSD(T) values for the various basis sets employed, validating the QCISD method for use in the further analyses.

4.3.2 Previous Studies

There are several studies in the literature which have focussed on BeH^-, but none before that of Verdicchio *et al.*[1] had remarked upon the unusual nature of this species. Along with the aforementioned publication, there has been another very recent study, from Koput in 2013[12] in which multi-reference average coupled-pair functional (MR-ACPF) calculations were

	T_1	MRCI+Q/5Z	CCSD(T)/5Z	CCSD/5Z	CCSD/TZ	QCISD/5Z	QCISD/TZ
BeH^-	0.012	15 588	15 995	15 595	15 438	15 616	15 420
MgH^-	0.020	12 137	11 928	11 672	11 704	11 696	11 725
CaH^-	0.037	15 665	15 681	15 473	15 207	15 564	15 274
SrH^-	0.041	15 197	15 368	15 196	14 938	15 290	15 010
BaH^-	0.049	17 295	17 377	17 165	16 649	17 323	16 771
RaH^-	0.046	14 175	14 309	14 136	13 750	14 271	13 858

Table 4.4: Values for the T_1 diagnostic for the MH^- series from CCSD(T) calculations, along with interaction energies in units of cm^{-1} calculated using MRCI+Q, CCSD(T), CCSD, and QCISD levels of theory with triple- and quintuple-ζ basis sets outlined in Section 4.1. The geometry has been fixed as the CCSD(T) R_e in each case.

performed with aug-cc-pCVXZ basis sets of up to septuple-ζ quality, the results of which are in Table 4.5. These results show very good agreement with the present CCSD(T) results. The results of Verdicchio's calculations, however, are seen to be in fairly poor agreement with ours, with a higher R_e and D_e obtained from their full CI calculations using septuple-ζ basis sets. From test calculations at the CCSD(T)/cc-pwCVXZ level of theory, it was found that the discrepancy between the present results and Verdicchio's are attributable to the absence of diffuse functions in the latter study, a conclusion which is supported by similar findings by Koput from his own MR-ACPF/cc-pV6Z calculations which essentially reproduced the constants of Verdicchio.

Other work includes a study by Rosmus and Meyer from 1978[13] using PNO-CI and CEPA methodologies, where the CCSD(T) calculations are seen to be in excellent agreement with the latter set of calculations. Two different studies have used Møller-Plesset theory, one published by Frenking and Koch in 1986[14] and the other by Polášek and Zahradník in 1995.[15] It is curious that these results are not in greater agreement with each other given their similar methodologies. The current results are in much better agreement with the bond length of the 1995 paper, and it is noted that as that study used basis sets with diffuse functions and the earlier Frenking and Koch paper did not, it seems likely that the discrepancies can be explained by choice of basis functions. However, it is of note that the vibrational frequency published by Polášek and Zahradník is much greater than ours and their equilibrium bond length a little shorter. One other study can be found using equations of motion by Kenney and Simons in 1975[16] which, despite calculating a bond length in very good agreement with the present results, gives a much greater value of D_e. This difference could be explained by the rather small basis sets employed by those workers.

Studies which have looked at MgH^- are limited to a single case; the same publication from Rosmus and Meyer which included BeH^-.[13] As above, the CCSD(T) results show excellent agreement with the constants from the CEPA calculations.

As for the remaining members of the MH^- series, there are no other results experimentally or theoretically. Consequently, the present values are the only ones available for M = Ca—Ra.

	R_e / Å	D_e / cm^{-1}	D_0 / cm^{-1}	ω_e / cm^{-1}	$\omega_e x_e$ / cm^{-1}	k / Nm^{-1}	Ref.
BeH^-	1.411	16 020	15 203	1660	51.1	147	This work
	1.430	17 070					1[a]
	1.415	15 837					1[b]
	1.430	17 056		1507			12[c]
	1.413	16 041					12[d]
	1.422		13 230	1650	48		13[e]
	1.426		14 520	1620	49		13[f]
	1.406			1755			15[g]
	1.479		15 730	1520			14[h]
	1.413	17740		1820			16[i]
MgH^-	1.857	11 910	11 356	1125	34.4	72	This work
	1.858		10 000	1141	34		13[e]
	1.860		11 210	1129	34		13[f]
CaH^-	2.103	15 730	15 199	1075	24.3	67	This work
SrH^-	2.261	15 430	14 935	999	19.9	59	This work
BaH^-	2.335	17 520	17 031	987	16.7	57	This work
RaH^-	2.470	14 396	13 947	907	17.4	49	This work

[a] Full CI/cc-pV6Z basis set from Verdicchio *et al.*
[b] MRCI/aug-cc-pVQZ from Verdicchio *et al.*
[c] MR-ACPF/cc-pV6Z from Koput.
[d] MR-ACPF/aug-cc-pCV7Z(i) with corrections, from Koput.
[e] PNO-CI from Rosmus and Meyer.
[f] CEPA from Rosmus and Meyer.
[g] MP2/6-31++G** (MP4/6-31++G** for ω_e) from Polášek and Zahradník.
[h] MP2/6-31G(*d*,*p*)//MP4(SDTQ)/6-311++G(*df*,3*pd*) from Frenking and Koch.
[i] EOM from Kenney and Simons.

Table 4.5: Spectroscopic parameters for the MH^- series. R_e is the equilibrium bond length, D_e and D_0 are the equilibrium and zero point dissociation energies respectively, ω_e is the harmonic vibrational frequency, $\omega_e x_e$ is the anharmonicity constant, and k the force constant from Hooke's law.

4.3.3 Geometric Parameters

The calculated spectroscopic parameters for the MH^- series of complexes have been collected in Table 4.5. Contrary to the RG–H^- complexes, the metal-containing analogues show a monotonic increase in R_e as the group is descended. Since these complexes show much shorter bond lengths, the position of the hydrogen anion will be more susceptible to the increasing radius of the other atom.

The harmonic vibrational frequencies also show an increase in strength of interaction, with higher values of ω_e than were seen for the RG–H^- complexes. The force constant, k, also shows a dramatic increase of around an order of magnitude for the entire series. Notably, the force constant for BeH^- is seen to be more than twice the value of the any other complex in the series, as will be addressed in Section 4.3.7.

4.3.4 Dissociation Energies

As stated in the introduction to this chapter, the D_e of BeH^- has been previously characterised by other groups as being high, at around 16 000 cm^{-1}. CCSD(T) results in Table 4.5 are seen to agree very well with the previous studies. Other complexes in the series are seen to possess similarly high binding energies, although the trend down the group deviates from monotonicity as will also be addressed in Section 4.3.7.

4.3.5 Partial Atomic Charges

The same partial atomic charge analyses have been used for the MH^- complexes as for RG–H^-, and the outcome is presented along with the RG–H^- charges in Table 4.3. Charges located on the metal atom are seen to be much higher than those for the rare gases. Additionally, descrepancies between

the different methodologies are rather more noticeable.

Mulliken analysis gives negative charges in all cases here, but the magnitudes are unexpectedly high, with essentially the whole excess negative charge placed on the beryllium atom in the case of BeH^-. Both the electronegativities for Be and H (1.57 and 2.20 respectively) and the unstable nature of the beryllium anion[17] imply that this is extremely unlikely. NPA and AIM are both more in line with expectations in their predictions of charge transfer, although the analyses differ for the lighter complexes, with NPA predicting a much larger charge for the lighter metals. Differences between the two methods settle down for the heavier complexes. It is possible that the natural orbital transformation algorithms are struggling to separate out the atomic contributions given the very short bonds of the lightest complexes—if this were to be the case then the AIM results could be considered as more reliable. These differences will be further discussed in the context of the forms of the orbitals in Section 4.3.7.

4.3.6 Orbital Contour Plots

Figure 4.2 shows the natural orbital contour plots of the HOMO and HOMO-1 for selected members of the MH^- series, BeH^-, CaH^-, and BaH^-. In stark contrast to the RG–H^- complexes, the MH^- complexes show significant perturbation from atomic orbitals at R_e. For both of the displayed orbitals there is significant orbital density on both centres.

Contour plots for the same species are additionally plotted at a variety of internuclear separations, expressed in terms of R_e. At around $4R_e$, the atoms are seen to be essentially non-interacting, with the HOMO and HOMO-1 having contributions from only a single centre. Consequently, it can be seen that the HOMO corresponds to the singly-occupied outermost metal valence ns orbital, and the HOMO-1 to the doubly occupied hydrogen 1s orbital.

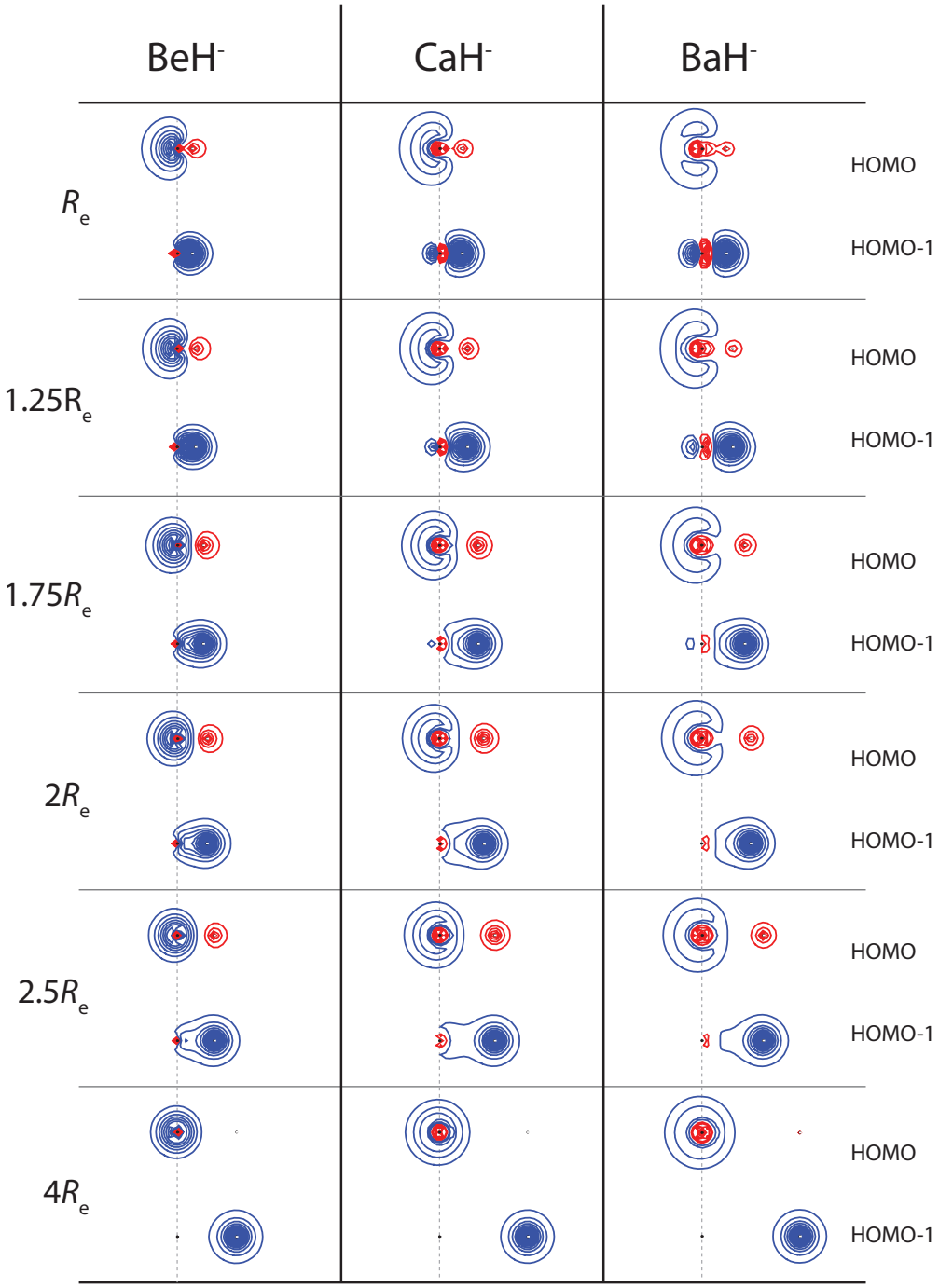


Figure 4.2: Natural orbital contour plots for selected members of the MH^- series at varying internuclear separations.

As the two nuclei draw closer together, each orbital is seen to have density over both centres, and a continuous evolution can be followed through to the resulting mixed-character orbitals at R_e.

4.3.7 Group 2 Metal Hybridisation

From previous analyses, there are strong indications of molecular orbitals being formed between the metal and hydride anion for these species, and the precise nature of these orbitals can be more accurately characterised through NBO data. The atomic contributions to these molecular orbitals are listed in Table 4.6. The composition of the HOMO is entirely metal based, which is seen to be further subdivided into contributions from orbitals of different angular momenta. In the case of beryllium and magnesium, this subdivision is mostly s character, with some contribution from p orbitals. For CaH^- onwards, there are seen to be further contributions from d orbitals. As these HOMOs began as the metal valence ns orbitals at long R, it is seen that these orbitals have undergone hybridisation due to the presence of the nearby anion, the exact form of each orbital depending on the specific metal.

The differences in hybridisation schemes are explained by the differences in energetic accessibility of orbitals of each angular momentum for the individual metals. As an indication of these energetics, the energies of the $^1P \leftarrow {}^1S$ and $^1D \leftarrow {}^1S$ excitation processes are given in Table 4.7. For the two lighter metals the virtual np orbital is seen to be more easily accessible, and for the heavier four the virtual nd orbital becomes lower in energy.

The HOMO-1, which at long R was seen to be the H 1s atomic orbital, shows clear contributions from both metal and hydrogen, with NBO analysis declaring this to be a bonding orbital. Again, the metal contributions are not from a single atomic orbital, but instead from a mix of different atomic orbitals of differing angular momenta. Here, the same regimes of

MH^-	Occupancy	% H s	% M	% M s	% M p	% M d
			HOMO			
BeH^-	1.735	0.0	100.0	65.2	34.6	0.2
MgH^-	1.635	0.0	100.0	58.2	41.5	0.2
CaH^-	1.646	0.0	100.0	64.8	26.9	8.4
SrH^-	1.640	0.0	100.0	66.0	23.0	11.0
BaH^-	1.689	0.0	100.0	73.3	13.2	13.4
RaH^-	1.653	0.0	100.0	68.9	15.9	15.3
			HOMO-1			
BeH^-	1.951	81.5	18.5	40.8	58.8	0.4
MgH^-	1.943	87.4	12.6	48.2	51.3	0.6
CaH^-	1.941	91.1	8.9	37.4	29.2	33.4
SrH^-	1.940	92.2	7.8	36.0	21.8	42.1
BaH^-	1.941	91.6	8.4	27.6	8.8	61.7
RaH^-	1.940	92.8	7.2	34.1	10.8	52.7

Table 4.6: NBO data for the HOMO and HOMO-1 orbitals for the MH^- series.

hybridisation are seen, with beryllium and magnesium being predominantly sp-hybridised, and calcium onwards being more complex spd-hybrids.

Non-monotonic trends in the interaction energies of these complexes also appear to be explicable by the extent to which these species are able to hybridise, regardless of whether said hybridisation is sp or sd in nature. From Mg, the cost of hybridisation decreases to Ca and there is a corresponding increase in D_e of CaH^- compared to that of MgH^-. Sr has a similar excitation energy to Ca, and CaH^- and SrH^- are seen to be similar in their dissociation energies. There is then a sizeable increase in D_e to BaH^- which is explained by the notably low energetic cost of hybridisation, before a drop in strength of binding for RaH^- with an increase in the cost of hybridisation.

Clearly, however, there are other effects at play, since for example RaH^- is bound by less than would be expected on the basis of this argument alone, the strength of interaction is expected to be ameliorated as the group is descended by an increasingly important electronic repulsion term, as well as in the case of RaH^- the lanthanide contraction and relativistic effects playing

	Be	Mg	Ca	Sr	Ba	Ra
$^1P \leftarrow {}^1S$ / cm^{-1}	42 565	35 051	23 652	21 698	18 060	20 715
$^1D \leftarrow {}^1S$ / cm^{-1}	56 882	46 403	21 850	20 150	11 395	17 081

Table 4.7: Energies of the $^1P \leftarrow {}^1S$ and $^1D \leftarrow {}^1S$ excitations for the Group 2 metals taken from Reference 17.

a role, causing deviations from monotonicity.

The final outlier to this trend would be BeH^- which has a significantly higher D_e than its high-lying virtual np and nd orbitals would imply. When these MH^- complexes are considered at their equilibrium seperations, it is important to consider the *hybridised* form of the metal and not its atomic electronic structure. Every other metal in Group 2 possess a doubly occupied $(n\text{-}1)p_z$ orbital which is partially exposed when electron density is moved from the valence ns orbital. Beryllium has no such occupied p_z orbital, and as such the repulsion terms in BeH^- would be expected to be considerably lower, since the directionality of the p_z orbital will give a more directed repulsive interaction than the isotropic s orbital. This smaller repulsive interaction means that the hydrogen anion can approach the beryllium nucleus much more closely than for other metals, resulting in a much higher ion/induced-dipole term. These effects combine to give an extremely strongly bound BeH^- unit.

4.4 Conclusions

PECs have been calculated for the RG–H^- and Group 2 MH^- series using CCSD(T) theory. The rare gas hydride series is shown to be completely non-covalent, characterised by weak binding energies and long bond lengths. The attractive interactions here seem to be primarily limited to ion/induced-dipole terms, along with an important repulsion term. Orbital contour plots and partial atomic charge analysis reveals that the electronic character of the constituents of these complexes are atomic-like, with only small perturbations seen to the density in the cases of even the heavier, more polarisable rare gases. These findings are supported by the total energy density $H(r)$ from AIM analysis, which asserts that these complexes are entirely non-covalent.

Conversely, the MH^- series are strongly bound molecules which demon-

strate formation of a bonding orbital facilitated *via* sp- or spd-hybridisation of the metal at R_e, something which the RGs are not capable of due to the much higher energetic costs. The trend in strength of these binding energies is fairly convoluted, and is due to a delicate balance increasing electronic repulsion terms and reducing ion/induced-dipole terms (due to the increasing bond lengths), as well as the energetic cost of hybridisation for the Group 2 metals, as inferred by inspection of electronic excitation energies from Table 4.7. Orbital contour plots show strong delocalistaion of density over both centres, with partial atomic charges showing significant movement of electrons, and $H(r)$ showing covalent character in all cases. These interactions are clearly at odds with those present in the RG–H^- series, despite the two series both arising from closed shell, anion-neutral interactions.

Bibliography

[1] M. Verdicchio, G. L. Bendazzoli, S. Evangelisti and T. Leininger, *The Journal of Physical Chemistry A*, 2013, **117**, 192–199.

[2] H.-J. Werner, P. J. Knowles, G. Knizia, F. R. Manby, M. Schütz *et al.*, MOLPRO , version 2012.1, a package of ab initio programs, 2012, see http://www.molpro.net.

[3] R. J. LeRoy, Level 8.0: A Computer Program for Solving the Radial Schrödinger Equation for Bound and Quasibound Levels, University of Waterloo Chemical Physics Research Report No. CP-663, 2007; see http://leroy.uwaterloo.ca/programs/.

[4] B. Prascher, D. Woon, K. Peterson, J. Dunning, ThomH. and A. Wilson, *Theoretical Chemistry Accounts*, 2011, **128**, 69–82.

[5] I. S. Lim, H. Stoll and P. Schwerdtfeger, *The Journal of Chemical Physics*, 2006, **124**, 034107.

[6] M. Kaupp, P. v. R. Schleyer, H. Stoll and H. Preuss, *The Journal of Chemical Physics*, 1991, **94**, 1360–1366.

[7] G. Schaftenaar and J. H. Noordik, *Journal of Computer-Aided Molecular Design*, 2000, **14**, 123.

[8] A. Shalabi, K. Eid, M. Kamel and A. El-Barbary, *Physics Letters A*, 1998, **239**, 87–93.

[9] G. L. Bendazzoli, S. Evangelisti and F. Passarini, *Chemical Physics*, 1997, **215**, 217–225.

[10] V. Vallet, G. Bendazzoli and S. Evangelisti, *Chemical Physics*, 2001, **263**, 33–40.

[11] D. Cremer and E. Kraka, *Angewandte Chemie International Edition in English*, 1984, **23**, 627–628.

[12] J. Koput, *The Journal of Chemical Physics*, 2013, **139**, 104309.

[13] P. Rosmus and W. Meyer, *The Journal of Chemical Physics*, 1978, **69**, 2745–2751.

[14] G. Frenking and W. Koch, *The Journal of Chemical Physics*, 1986, **84**, 3224–3229.

[15] M. Polášek and R. Zahradník, *International Journal of Quantum Chemistry*, 1995, **54**, 93–98.

[16] J. Kenney and J. Simons, *The Journal of Chemical Physics*, 1975, **62**, 592–599.

[17] W. M. Haynes, *CRC Handbook of Chemistry and Physics*, CRC Press/Taylor and Francis, Boca Raton, FL, 2014.

Chapter 5

Trends in the Group 2 and Group 12 M^+–RG series

Many theoretical studies have been undertaken previously by the Wright group on M^+–RG systems, covering groups 1,[1–5] 2,[6–8] 11,[9,10] 12,[11,12] and 13.[13–16] These studies used CCSD(T) or RCCSD(T) theory with large basis sets to calculate PECs and subsequently derive spectroscopic constants, in a manner analogous to that presented in Chapter 3. From such a wealth of data, it is possible to conduct systematic comparisons between different groups, identifying commonalities and differences between modes of interaction between metal cations and rare gas atoms. Since the rare gas atoms tend to behave in a predictable fashion, for a consistent rare gas atom these trends can be thought of as idiosyncratic to the metal cations involved.

Of the groups previously studied, the metal cations belonging to groups 1, 11, and 13 all possess $^1\Sigma^+$ ground states, and as such it could be anticipated that the interactions between those M^+–RG complexes would be of essentially the same character. However, as previous investigations have highlighted, interactions in the Group 11 M^+–RG complexes exhibit rather strong binding energies,[9] with Au^+–Xe in particular being very strongly bound and proposed as exhibiting covalency.[10,17] Conversely, the Group 1 complexes are comparatively weakly bound and can be described well

by a 'physical' model potential which includes only induction, dispersion, and repulsion terms.[5] Group 13 is a different case again, with the heavier members of the group showing similar behaviour to the Group 1 complexes,[15] and the lighter members, especially B^+,[16] showing strong binding energies with some covalent effects.

Another logical comparison presents itself in the case of the Groups 2 and 12 M^+–RG complexes. For these complexes, both groups possess common $^2\Sigma^+$ ground states, with a single unpaired electron in a valence ns orbital. Consequently, owing to isoelectronic arguments, these groups would be expected to exhibit close similarities in their interactions. However, as has been seen in previous chapters, the interactions of the Group 2 elements are often heavily influenced by the energetic availability of low-lying ^{2}P or ^{2}D orbitals, and the corresponding states for the Group 12 M^+–RG complexes are much less energetically accessible with much higher orbital energies. In this chapter, a comparison between the interactions in these two series is presented.

5.1 Computational Methodology

The previous studies from the Wright group on the Groups 2 and 12 M^+–RG complexes used custom-designed basis sets produced by Edmond Lee of the University of Southampton, of the same overall construction as the Dunning-style basis sets and of approximately quintuple-ζ quality. Obviously results obtained using only a single quality of basis set cannot be extrapolated to the basis set limit, and so, since appropriate basis sets have subsequently been developed by Kirk Peterson of Washington State University for all relevant metals,[18–20] PECs for these species have been recalculated, some in conjunction with Anna Andrejeva and William Tuttle.

Similarly to the treatment given in Chapter 3, PECs for each of the 54

complexes have been calculated using RCCSD(T) theory, covering a wide range of internuclear separations. Both quadruple- and quintuple-ζ quality basis sets have been used, the results of which were extrapolated to the basis set limit using the method of Halkier *et al.*[21] as discussed in Section 2.2.1. These basis set-extrapolated curves are then used with LeRoy's LEVEL 8.0 code,[22] which both interpolated the curves to give more accurate equilibrium separations and dissociation energies, and calculated rovibrational levels. Further spectroscopic constants were calculated by use of standard Morse expressions, as outlined in Section 2.4.3.

Exact designations of basis sets employed for the metals are as follows; for beryllium and magnesium, aug-cc-pwCVXZ; for Ca—Ba, aug-cc-pCVXZ-PP basis sets along with effective core potentials ECP10MDF, ECP28MDF, ECP46MDF respectively; and for Zn, Cd, Hg, and Ra, aug-cc-pwCVXZ-PP basis sets with effective core potentials ECP10MDF, ECP28MDF, ECP60MDF, and ECP78MDF. For the rare gases, an aug-cc-pVXZ basis set was used for He, and for Kr—Rn aug-cc-pwCVXZ-PP basis sets with effective core potentials ECP10MDF, ECP28MDF, and ECP60MDF respectively. As for Ne and Ar, either aug-cc-pCVXZ or aug-cc-pwCVXZ basis sets were used to match whether a core-weighted basis set was used or not for the metal cation. The use of either core-valence or weighted-core-valence basis sets is not expected to impact the results significantly, as the weighting of the core functions in the basis sets is merely intended to give a better description of the core-valence correlation (albeit at the expense of the quality of the less important core-core correlation). Although the weighted-core valence basis sets have also been found to recover slightly more correlation energy compared to a core valence basis set of equivalent quality, this effect is very slight and should not significantly affect the interaction energies.

The frozen core approximation has also been employed for the correlation

treatment in order to speed up these calculations. All of the Group 2 calculations correlated all electrons on the metal not described by the ECPs. For the rare gas atoms, the Ne 1s orbitals and Ar 1s, 2s, and 2p orbitals were frozen. Each of the heavier rare gases RG = Kr—Rn had the inner-valence (n-1)s and (n-1)p orbitals frozen. As regards Group 12, each of the metals Zn—Hg had only their inner-valence (n-1)s orbitals frozen, since the (n-1)p orbitals for these cations are higher in energy than the analogous Group 2 cation orbitals, and all others (save for those described by the ECP) were correlated. The same correlation scheme that was used for the rare gas atoms in the Group 2 complexes was also used for Zn^+–RG and Cd^+–RG, and also for the Hg^+–He, Hg^+–Ne, and Hg^+–Ar complexes, but the 5p orbitals on the mercury cation are energetically closer to the inner-valence orbitals for RG = Kr—Rn. As such, for those three complexes only the inner-valence Hg^+ 5s orbital was frozen, and all others outside of ECPs (including those on the rare gas) were correlated.

Birge-Sponer (BS) plots were created using the spacings between the vibrational levels calculated by LEVEL; additionally, a line was included for each BS plot computed using spacings between the energies of vibrational levels calculated using the values of ω_e and $\omega_e x_e$ obtained from the lowest two vibrational levels. Orbital contour plots were also produced for these complexes, the orbital energies being taken from HF calculations performed at the CCSD(T)/EBS R_e using triple-ζ weighted-core basis sets of the same designation as those used for the PEC calculations, and the contours being taken from the same calculations and visualised using MOLDEN.[23] Partial atomic charges were also appraised using Mulliken, AIM, and NPA theories to analyse the density from QCISD calculations performed with Gaussian 09[24] using the same triple-ζ basis sets as above. The NPA analysis used the NBO6 software,[25] whilst the AIM analysis used T. A. Keith's AIMAll.[26]

5.2 Previous Studies

Owing to the large number of complexes this chapter encompasses, a full survey of previous studies is not provided here. All of these complexes have been previously studied by the Wright group,[6–8,11,12] the results of which showed overall good agreement with other studies which had been conducted at higher levels of theories. Generally good agreement was also observed with experimental results, where available. In some cases, these experimental results were spectroscopic studies which reported spectroscopic constants with which to compare. In other cases, these were ion mobility studies examining the movement of metal cations through a rare gas bath, reporting transport coefficients. Since the PECs calculated within the Wright group were used by Larry Viehland of Chatham University to model ion mobility data, this provided another avenue of comparison by which to evaluate the quality of the calculated potentials.

Since the publication of those earlier works, there are seemingly only two subsequent studies which have been published on the Group 2 M^+–RG complexes, focussing on Ba^+–Xe[27] and Be^+–Ar.[28] The former study, by Abdessalem *et al.*[27], used a pseudopotential for the Ba^{2+}–Xe 'core' with the remaining one (or two for the neutral) electrons treated by full CI (with a (8s 6p 6d) basis set for Ba and (3s 4p) for Xe) to calculate several electronic states of both Ba^+–Xe and Ba–Xe. For the ground state of Ba^+–Xe, the spectroscopic constants stated show poor agreement in R_e with their value being 3.77 Å compared to the present CCSD(T) result of 3.581 Å. Similarly poor agreement is seen in the values for D_e, as the value reported by Abdessalem is 1971 cm^{-1}, higher than the result given here of 1731 cm^{-1}.

The 2014 study on Be^+–Ar by Niu *et al.*[28] used CASSCF/internally-contracted MRCI+Q in conjunction with both triple- and quadruple-ζ quality

Dunning-style basis sets, allowing extrapolation to the basis set limit. Again, several electronic states were calculated and spectroscopic constants derived for each state. For the ground state, D_e was reported as ~4030 cm^{-1}, which is in fairly poor agreement with the value reported here of 4405 cm^{-1}, though the agreement in R_e is fairly good, with a value of 2.065 Å compared to that reported here of 2.086 Å.

No subsequent studies seem to have been published for M = Zn—Hg.

5.3 Trends in the Spectroscopic Constants of the Group 2 M^+–RG Series

5.3.1 Equilibrium Internuclear Separations

Firstly, trends in the equilibrium bond length, R_e, for a given rare gas as the metal atom is changed shall be discussed. Values for R_e show an overall increase with increasing size of metal cation. For RG = Ne, Kr, Xe, and Rn, this increase is monotonic, but for RG = He there is a slight decrease from Ba^+–He to Ra^+–He, and for RG = Ar a small decrease is seen between Sr^+–Ar and Ba^+–Ar. These slight deviations from monotonicity are also in line with results for the rest of the series, since the neon complexes show a plateauing in R_e for M = Ba to Ra in line with the helium result, and the heavier three rare gases show a similar plateau for M = Kr to Xe, where the argon complexes experience their 'dip'.

Examining now the trends throughout each metal series as the rare gas atom is changed, there is more uniform behaviour seen for all series, marked by a decrease for RG = He through Ar, followed by an increase thereafter. With the heavier members of each series, the attractive and repulsive terms are close to equal (evinced by the weak binding energies) leading to a delicate

balance between these competing terms, the relationship between which changes as the rare gas is varied. Evidently, from helium through argon, the rate at which the attractive terms increase with R outpaces the increase in repulsive terms, leading to successively contracting bond lengths. From argon onwards however, the repulsive terms are seen to be becoming more important and so the bonds lengthen in response.

	R_e / Å	D_e / cm^{-1}	D_0 / cm^{-1} [a]		ω_e / cm^{-1}	$\omega_e x_e$ / cm^{-1}	k / Nm^{-1}	$\frac{D_e{}^{\text{Morse}}}{D_e}$
Be^+–He	2.923	133.3	98.8	(26)	74.7	11.17	0.96	0.94
Be^+–Ne	2.437	424.4	393.1	(7)	63.1	1.05	1.67	2.23
Be^+–Ar	2.086	4 405.3	4 239.6	(4)	335.1	7.68	57.10	0.83
Be^+–Kr	2.217	6 072.4	5 906.3	(3)	334.7	4.93	64.24	0.93
Be^+–Xe	2.403	8 272.6	8 103.2	(2)	340.5	3.40	69.42	1.03
Be^+–Rn	2.489	9 491.6	9 323.6	(2)	337.4	2.79	70.33	1.08
Mg^+–He	3.482	72.9	51.4	(29)	47.4	8.50	0.45	0.91
Mg^+–Ne	3.244	187.9	168.3	(10)	40.2	2.04	1.04	1.05
Mg^+–Ar	2.825	1 291.2	1 239.6	(4)	104.5	2.70	9.65	0.78
Mg^+–Kr	2.875	2 000.9	1 941.6	(3)	119.6	2.14	15.73	0.84
Mg^+–Xe	3.010	3 012.0	2 944.4	(2)	135.9	1.57	22.07	0.98
Mg^+–Rn	3.057	3 666.0	3 595.4	(2)	142.1	1.41	25.74	0.97
Ca^+–He	4.240	37.1	24.3	(35)	28.8	6.16	0.18	0.91
Ca^+–Ne	3.744	111.4	100.1	(10)	23.2	1.10	0.42	1.10
Ca^+–Ar	3.108	876.7	841.1	(4)	72.5	2.43	6.19	0.62
Ca^+–Kr	3.174	1 375.5	1 336.1	(3)	79.6	1.70	10.12	0.68
Ca^+–Xe	3.330	2 034.3	1 991.1	(2)	87.1	1.17	13.72	0.80
Ca^+–Rn	3.378	2 493.1	2 448.4	(2)	89.9	0.96	16.12	0.84
Sr^+–He	4.524	30.1	19.3	(36)	24.4	5.49	0.13	0.90
Sr^+–Ne	3.979	93.0	84.2	(9)	18.0	0.73	0.31	1.20
Sr^+–Ar	3.327	711.7	685.0	(4)	54.3	1.90	4.77	0.55
Sr^+–Kr	3.385	1 119.6	1 092.3	(2)	55.1	1.03	7.67	0.66
Sr^+–Xe	3.535	1 659.6	1 630.6	(2)	58.3	0.62	10.56	0.83
Sr^+–Rn	3.576	2 051.8	2 022.8	(1)	58.4	0.48	12.65	0.86
Ba^+–He	4.913	22.6	14.0	(38)	19.6	4.65	0.09	0.91
Ba^+–Ne	4.250	76.3	69.1	(9)	14.6	0.64	0.22	1.10
Ba^+–Ar	3.319	810.9	777.6	(4)	67.7	2.23	8.37	0.63
Ba^+–Kr	3.416	1 214.9	1 185.5	(2)	59.3	0.97	10.83	0.75
Ba^+–Xe	3.581	1 731.3	1 703.3	(2)	56.2	0.18	12.53	2.52
Ba^+–Rn	3.635	2 099.5	2 072.8	(1)	53.5	0.44	14.35	0.78
Ra^+–He	4.871	23.7	14.8	(38)	20.3	4.79	0.10	0.90
Ra^+–Ne	4.268	79.1	71.2	(10)	16.2	0.73	0.28	1.12
Ra^+–Ar	3.704	525.8	507.4	(3)	37.5	1.14	2.82	0.59
Ra^+–Kr	3.735	831.1	812.9	(2)	36.8	0.64	4.87	0.64
Ra^+–Xe	3.871	1 234.9	1 216.2	(2)	37.6	0.42	6.93	0.68
Ra^+–Rn	3.897	1 546.0	1 528.2	(1)	35.8	0.15	8.48	1.34

[a] The value in parentheses is the ZPVE expressed as a percentage of D_e

Table 5.1: Spectroscopic constants for the Group 2 M^+–RG series. R_e is the equilibrium bond length, D_e and D_0 are the equilibrium and zero point dissociation energies respectively, ω_e is the harmonic vibrational frequency, $\omega_e x_e$ is the anharmonicity constant, and k the force constant from Hooke's law. $D_e{}^{\text{Morse}}/D_e$ is calculated as outlined in Section 2.4.3.

5.3.2 Dissociation Energies

Moving onto the equilibrium dissociation energies, D_e, there is a general trend of decreasing dissociation energy with increasing atomic number of metal cation, although again there are some exceptions to this general trend which can (again) be subdivided into two different types of behaviour, for RG = He and Ne, and for RG = Ar—Rn. In the case of the lightest two rare gas series, there are much sharper decreases in energy seen for the lighter metal cations which eventually gives way to the interaction energies remaining more constant for M = Ca—Ra (there is in fact a slight increase in dissociation energy between Ba^+–RG and Ra^+–RG, but this is only by 1 and 3 cm^{-1} for RG = He and Ne respectively). For the heavier rare gas series, the dissociation energies are generally much higher than for the helium and neon analogues, and on top of the same overall decrease with increasing atomic number of metal the trends now show an inflection at M = Ba, which shows a slight rise relative to the binding energy of the Sr^+–RG complexes, before a decrease again to Ra^+–RG. There is, despite this less subtle non-monotonic behaviour, still a fair consistency between the Ca^+–RG and Ra^+–RG complexes compared to the Be^+–RG and Mg^+–RG series. Interpreting this in terms of the balance between the attractive and repulsive effects, it would seem as though the initial short bond lengths (increased induction terms) and low electron counts (reduced repulsion terms) on the lightest metals gives rise to high dissociation energies, which are quickly ameliorated by the lengthening bonds and increasing electronic repulsion with the heavier metal cations. The relative changes in these competing effects seem to be more or less consistent from M = Ca onward, as the overall interaction energy remains fairly consistent, although small fluctuations still occur.

When the trends in D_e are viewed for each metal series varying the RG atom, completely different trends are observed, with monotonically increasing values. This effect is far more straightforward in origin; since the leading term in the attractive potential is expected to be the ion/induced-dipole term, it would be expected that the successively more polarisable heavier rare gases would give consistently increasing attractive terms, and it is seen to be the case that these attractive terms also increase more than does the electronic repulsion.

Examining the zero point vibrational energy (ZPVE) for each complex, the ZPVE as a percentage of the equilibrium dissociation energy (tabulated in parentheses next to D_0 in Table 5.1) is seen to be very consistent throughout each rare gas series. Further, the relative percentage of ZPVE decreases monotonically with increasing mass of rare gas, in line with the reduced mass effect stating that increasing reduced mass leads to a decrease in vibrational frequency, including that of $v = 0$.

5.3.3 Harmonic Vibrational Frequencies and Force Constants

Examination of the harmonic vibrational frequencies, ω_e, reveals trends similar to those seen in D_e for both the metal series and the rare gas series, although there are some nuanced differences. However, since the harmonic vibrational frequencies can be considered as a consequence of two effects, the electronic interaction and the reduced mass of each system, trying to disentangle these different effects is not necessarily instructive. Instead, trends in the force constant from Hooke's law, k, are considered. Freed from the mass effect, trends are now seen to be much simpler.

Within a metal series, the force constant increases monotonically with increasing atomic number of the rare gas partner, consistent with the trends

observed in D_e for these species. Agreement with trends in D_e also extends to the behaviour of the force constant within the rare gas series. These similarities are evident down to even slight details, with the same division into two behaviours seen for light and heavy rare gas groups (He—Ne and Ar—Rn), with the former group showing an overall decrease as size of metal increases, with a slight increase in value for the radium complexes, and the latter group showing an overall decrease with a slight inflection at M = Ba.

With regards to the ${D_e}^{\text{Morse}}/D_e$ ratio, the trends are more erratic, making it difficult to draw any firm conclusions. It is interesting to note that the general trend throughout each metal series (of an increase from M^+–He to M^+–Ne, a decrease towards M^+–Ar, then an increase after) is roughly similar despite a few notable exceptions (in particular, Be^+–Ne), and also that the values for the M^+–He complexes are near uniform at ~ 0.9. As will be discussed in Section 5.5, the ${D_e}^{\text{Morse}}/D_e$ ratio taken in isolation is of limited utility, although it is clear that there are strong deviations from Morse-like behaviour seen in many of these complexes.

5.4 Trends in the Spectroscopic Constants of the Group 12 M^+–RG Series

5.4.1 Equilibrium Internuclear Separations

Trends within a rare gas series with the different metals show the same behaviour for all series, in that the Cd^+–RG complexes show the longest bond lengths in each case and the Zn^+–RG complexes the shortest. An obvious reason for this effect is found through consideration of the ionic radii of the metal cations, especially using the Wright-Breckenridge radius,[29] wherein the ionic radius of a cation is found by subtracting half the He_2

dimer R_e (1.49 Å) from that of M^+–He. In this case, this treatment leads to the ordering of the ionic radii being Cd>Hg>Zn, a result which is predicted by the lanthanide contraction experienced by mercury, and straightforwardly explains each rare gas series showing consistent trends in R_e.

Examining a specific metal series as the rare gas atom is varied shows a rather different picture, which is closer to the trends seen for Group 2. For all three series, there is an initial decrease in bond length as the atomic number of the rare gas increases, followed by a rise for the heavier rare gases, with the turning point being at M^+–Ar for M = Zn and Hg, and at M^+–Kr for M = Cd. The same logic as was used for the similar trends in Group 2 is also applied here, namely that there exists a delicate balance between the attractive and repulsive terms in each complex. Consistency in the behaviour of the Zn^+–RG and Hg^+–RG complexes implies that due to the lanthanide and relativistic contractions of the mercury cation its behaviour ends up being quite similar to that of the zinc cation. The larger cadmium cation experiences a different balance between the competing terms and so a minimum value is observed for R_e with a different rare gas partner compared to the other two series.

5.4.2 Dissociation Energies

For each rare gas series, a decrease in binding energy is seen between the Zn^+–RG and Cd^+–RG complexes, then an increase for Hg^+–RG. Comparison of the binding energies for Zn^+–RG and Hg^+–RG also shows fairly similar values for a given rare gas. As seen for the Group 2 series, increasing the size of the metal cation will generally lead to a longer bond length which will in turn lead to reductions in attractive terms; however, as discussed above for the bond lengths, the lanthanide contraction results in shorter than expected bond lengths for the Hg^+–RG complexes. This gives a stronger ion/induced-

	R_e / Å	D_e / cm^{-1}	D_0 / cm^{-1} [a]		ω_e / cm^{-1}	$\omega_e x_e$ / cm^{-1}	k / Nm^{-1}	$\frac{D_e{}^{\text{Morse}}}{D_e}$
Zn^+–He	3.014	131.2	99.3	(24)	68.8	10.01	1.05	0.90
Zn^+–Ne	2.879	312.1	285.7	(8)	54.1	2.57	2.62	0.91
Zn^+–Ar	2.627	2 061.6	2 002.2	(3)	119.7	2.04	20.77	0.85
Zn^+–Kr	2.656	3 290.7	3 229.2	(2)	123.6	1.25	32.66	0.93
Zn^+–Xe	2.759	5 197.0	5 131.0	(1)	132.4	0.87	44.49	0.97
Zn^+–Rn	2.806	6 371.9	6 306.6	(1)	130.9	0.68	50.08	0.99
Cd^+–He	3.205	113.8	84.6	(26)	63.2	9.88	0.91	0.89
Cd^+–Ne	3.057	281.5	257.3	(9)	49.7	2.55	2.48	0.86
Cd^+–Ar	2.914	1 496.8	1 452.3	(3)	89.8	1.61	14.04	0.83
Cd^+–Kr	2.922	2 390.0	2 345.6	(2)	89.2	0.94	22.63	0.88
Cd^+–Xe	2.995	3 885.9	3 837.9	(2)	96.3	0.60	33.41	0.99
Cd^+–Rn	3.025	4 870.0	4 823.0	(1)	94.2	0.43	39.40	1.05
Hg^+–He	3.077	149.1	112.7	(24)	78.7	11.78	1.43	0.88
Hg^+–Ne	3.003	351.4	322.0	(8)	60.3	3.09	3.90	0.84
Hg^+–Ar	2.876	1 802.0	1 753.63	(3)	97.4	1.35	18.66	0.98
Hg^+–Kr	2.856	3 110.6	3 068.8	(1)	83.8	0.69	24.55	0.82
Hg^+–Xe	2.905	5 546.2	5 494.3	(1)	104.1	0.42	50.92	1.17
Hg^+–Rn	2.938	7 140.4	7 091.4	(1)	98.2	0.42	60.12	0.80

[a] The value in parentheses is the ZPVE expressed as a percentage of D_e

Table 5.2: Spectroscopic constants for the Group 12 M^+–RG series. R_e is the equilibrium bond length, D_e and D_0 are the equilibrium and zero point dissociation energies respectively, ω_e is the harmonic vibrational frequency, $\omega_e x_e$ is the anharmonicity constant, and k the force constant from Hooke's law. $D_e{}^{\text{Morse}}/D_e$ is calculated as outlined in Section 2.4.3.

dipole interaction for Hg^+–RG than would otherwise be expected, with the end result being that the Cd^+–RG complexes are the most weakly bound.

As was the case for the Group 2 complexes, looking at trends for each metal series with the different rare gases shows a monotonic increase. Again, the rationale for this is the increase in polarisability with increasing atomic number of rare gas. Also as was seen above for the ZPVE, the amount of ZPVE relative to the equilibrium dissociation energy is greatest for the helium complex in each metal series, and shows a monotonic decrease with increasing atomic number of rare gas owing to the mass effect.

5.4.3 Harmonic Vibrational Frequencies and Force Constants

Trends in ω_e for Group 12 are also similar to what was seen for Group 2, in that they resemble the trends in D_e for the corresponding complexes with additional complications and inflections. Further, analysing trends

in the force constants shows excellent correspondence with the trends in D_e, reproducing accurately the subtleties seen in the relative dissociation energies.

As was true for Group 2, trends in the ${D_e}^{Morse}/D_e$ ratio are more complicated, without any particular patterns being evident. A more in-depth discussion of how Morse-like these complexes are is presented in Section 5.5, below.

5.5 Birge-Sponer Plots

Birge-Sponer plots have been created for the Group 2 and Group 12 M^+–RG complexes, and are presented in Figures 5.1—5.9, with each figure displaying the plots for a particular M^+–RG series. On each graph, the black points indicate the spacing between adjacent calculated vibrational levels, and the dashed red line corresponds to spacing between vibrational levels calculated from the vibrational constants ω_e and $\omega_e x_e$ (referred to here as the 'Morse line'). Derivation of the constants ω_e and $\omega_e x_e$ relies on only the lowest two vibrational levels as calculated by LEVEL, and so

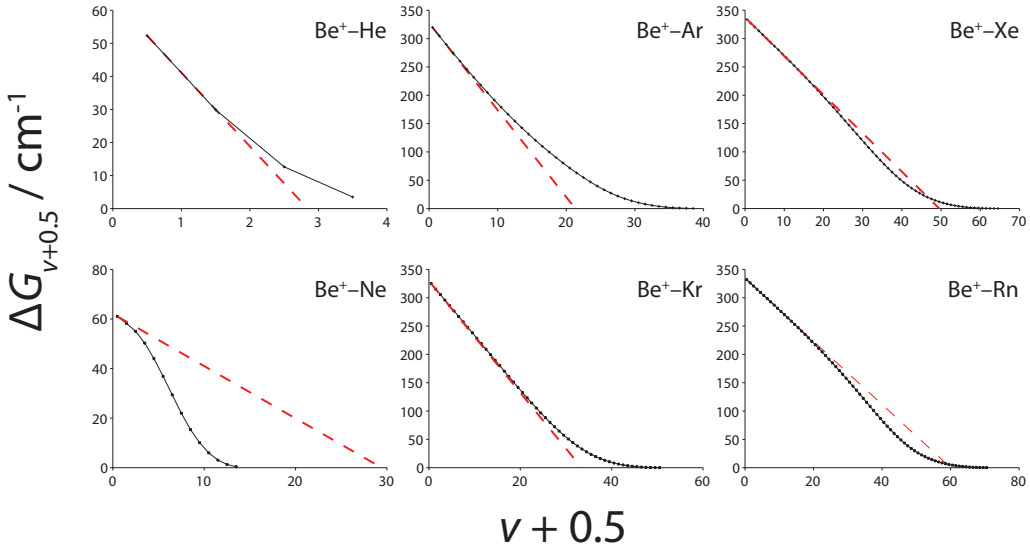


Figure 5.1: Birge-Sponer plots for the Be^+–RG series.

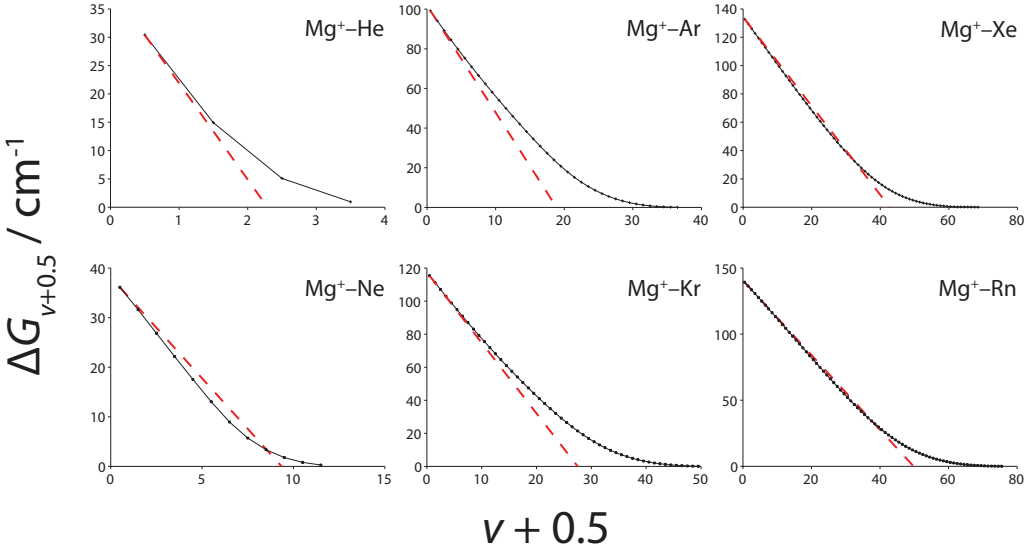


Figure 5.2: Birge-Sponer plots for the Mg^+–RG series.

this latter series give an indication of how well ω_e and $\omega_e x_e$ describe the shape of the rest of the PEC. Comparing the two series essentially gives an indication of how Morse-like each complex is, similar to the values of ${D_e}^{\text{Morse}}/D_e$ presented in Tables 5.1 and 5.2. The advantage of using the Birge-Sponer plots, however, is apparent from the form of many of the plots; for example, ${D_e}^{\text{Morse}}/D_e$ for Mg^+–Ne is 1.05 and so the two sets of spacings are expected to agree, but the Birge-Sponer plot for this complex shows that some vibrational levels fall below the expected value whilst others are

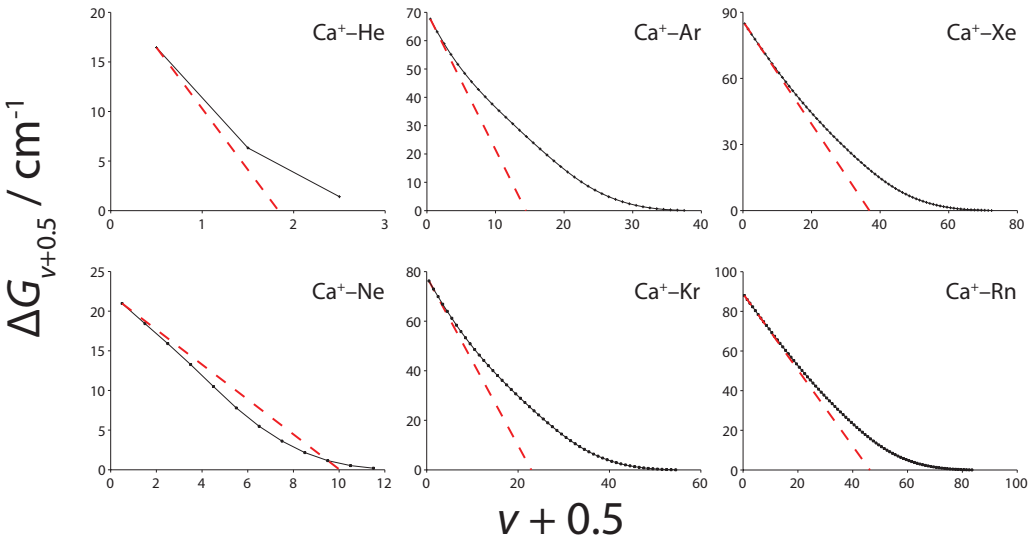


Figure 5.3: Birge-Sponer plots for the Ca^+–RG series.

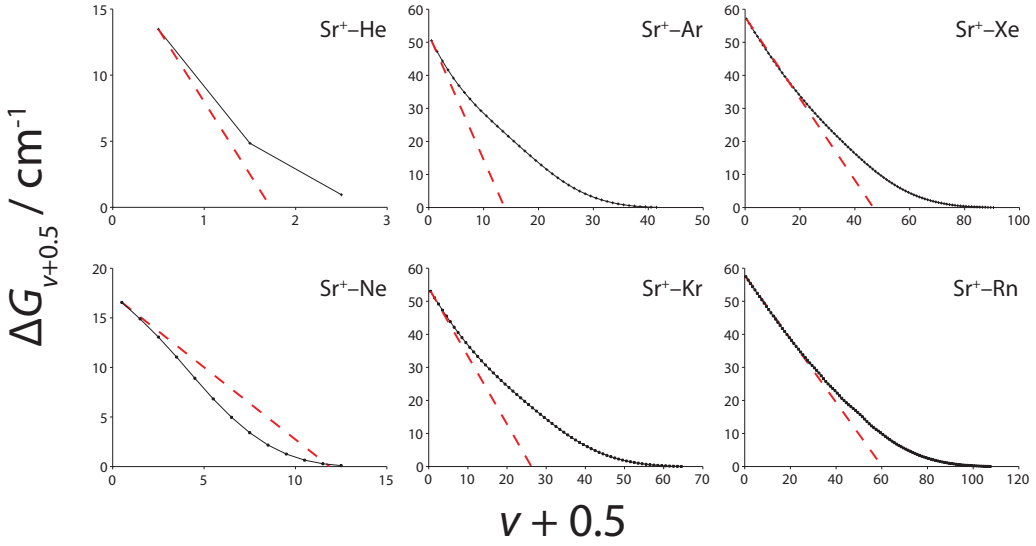


Figure 5.4: Birge-Sponer plots for the Sr^+–RG series.

above. These competing deviations essentially cancel out across the whole of the plot, necessitating the use of these plots to examine how closely the complexes follow Morse-like behaviour as a function of v (and thus R).

Each of the plots follows one of several different types of behaviour, with a few complexes lying outside of these categories. Many of the complexes (for example, Be^+–Kr) show the calculated points and the Morse line to be in good agreement for many vibrational levels, with the only significant deviation from Morse-like behaviour seen for higher vibrational levels as the actual

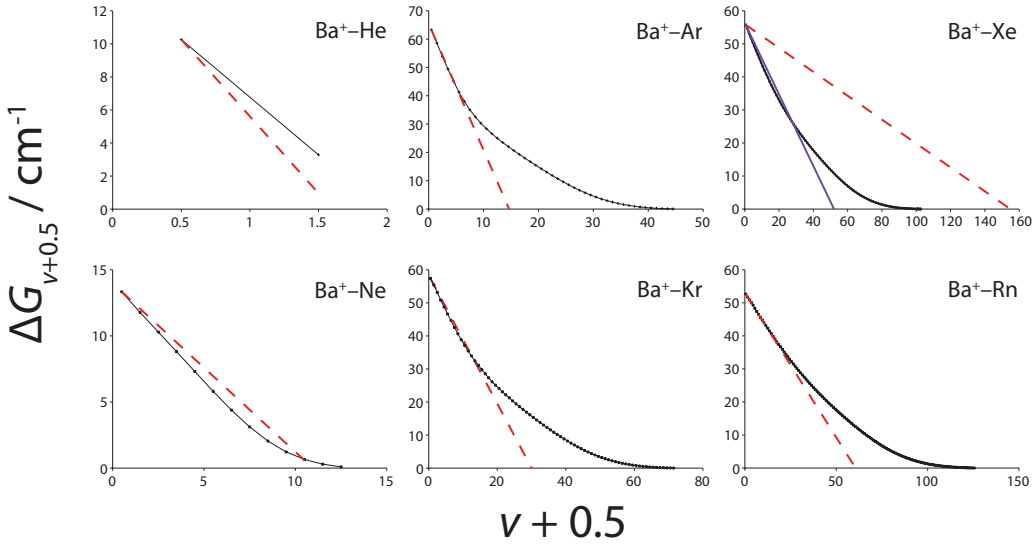


Figure 5.5: Birge-Sponer plots for the Ba^+–RG series.

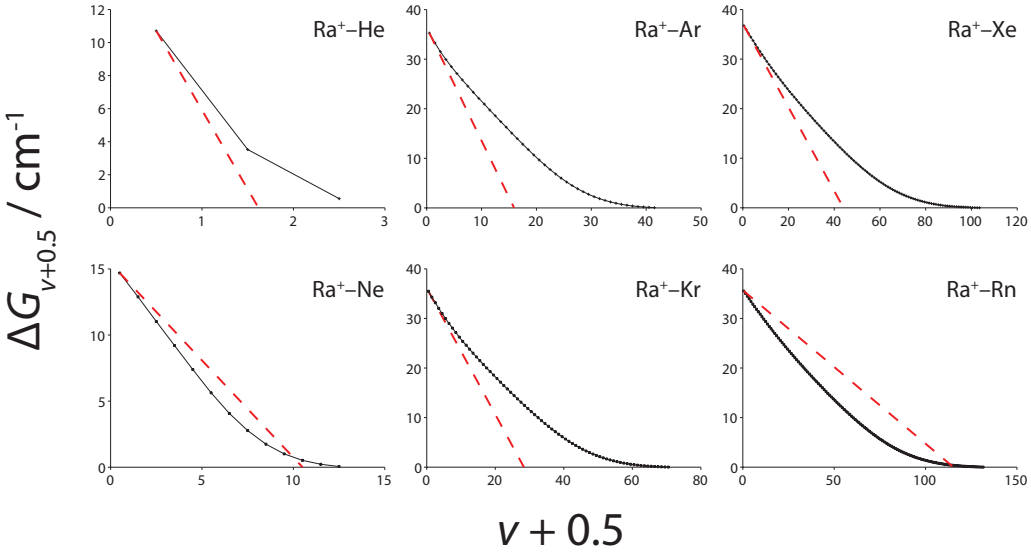


Figure 5.6: Birge-Sponer plots for the Ra^+–RG series.

vibrational level spacings tail off more gradually than expected from Morse behaviour. In addition to Be^+–Kr, both Mg^+–Xe and Mg^+–Rn produce plots that fit this description, as well as many of the Group 12 M^+–RG complexes in Figures 5.7—5.9. Since the different vibrational levels sample different parts of the potential energy curve, this deviation towards higher v arises from the R-dependence of the attractive terms. Since these complexes are chiefly bound by ion/induced-dipole (plus less important higher order terms) and dispersion forces, the drop-off of interaction strength is more gradual than

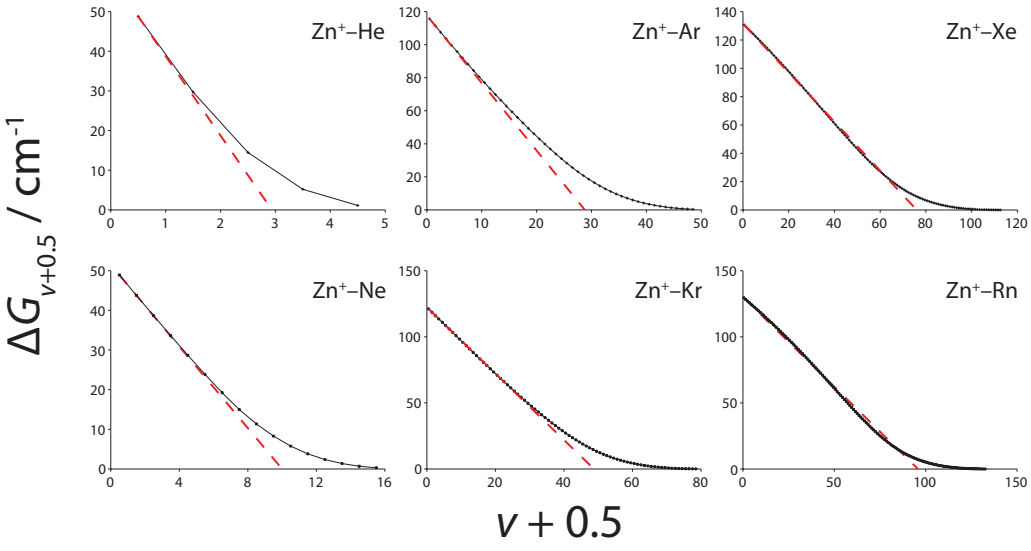


Figure 5.7: Birge-Sponer plots for the Zn^+–RG series.

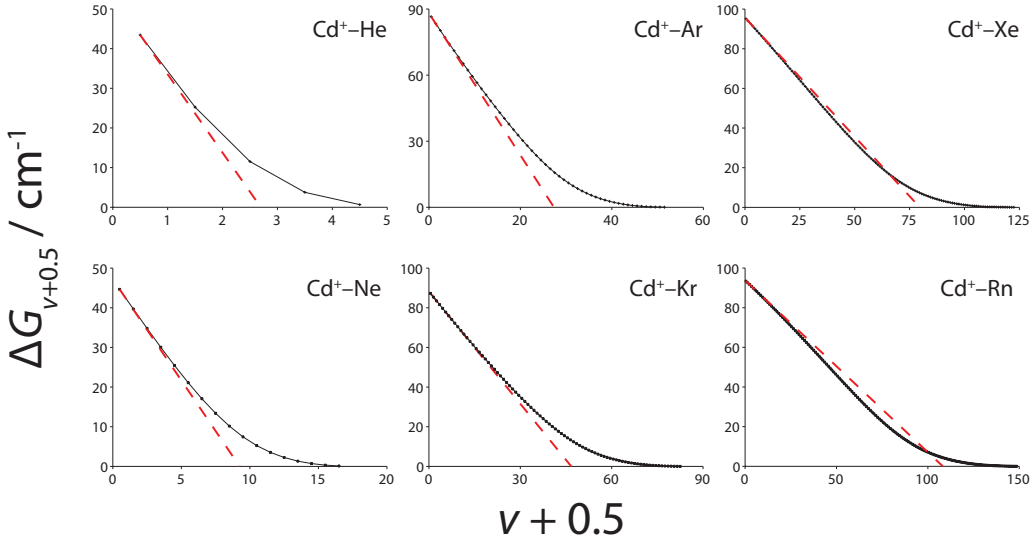


Figure 5.8: Birge-Sponer plots for the Cd^+–RG series.

it would be for a species with strong covalent contributions. Consequently, there are more bound vibrational states for these complexes than would be expected for a covalently bound species with a similar dissociation energy, a known limitation of BS analysis.[30]

Several examples are also seen of plots that show a similar but more pronounced deviation of the above type, characterised by a much earlier departure of the calculated points from the Morse line than in the examples stated above, such as for Ca^+–Ar. It should be noted that the M^+–He plots are of this type, but for those complexes the number of bound vibrational levels is so few that it is difficult to draw clear conclusions.

In some cases, the plotted points dip below the Morse line for moderate values of v as in the case of, for example, Be^+–Rn. These complexes also show the same tailing behaviour toward higher values of v as discussed above. For the cases where there is seen to be a more pronounced dip below the Morse line, the resulting ${D_e}^{\text{Morse}}/D_e$ ratio is greater than unity. At these regions where the points dip below, the gradient of the PEC must be steeper than expected by the Morse potential, indicating that at the corresponding values of R, the attractive terms are becoming less prominent relative to the

repulsive ones.

Most of the complexes exhibit behaviour according to one of the two regimes discussed above. A few of the complexes, however, produce plots notably different to the others. Hg^+–Rn shows plotted points which are above the Morse line for all but the first few vibrational levels. More peculiar is the plot for Be^+–Ne. In that case, the plotted points fall below the Morse line for almost all values of v. In fact, both of these species show plots which are quite similar in shape, with a greater difference seen in the Morse line. This effect could be due to a difference in the form of the potential at the well minimum. Since hybridisation is expected to play a role (especially for Group 2 metals) and only at short R, the values of ω_e and $\omega_e x_e$ for the well minimum will not necessarily describe the longer-range part of the potential. This leads to the Morse line, which is essentially an extrapolation of the first two points, showing poor agreement with the BS plot towards higher v.

Finally, Ba^+–Xe also presents an interesting case, as its Morse line is seen to deviate from the calculated spacings far more severely than for any other species. To address this, another (purple, solid) line has been plotted using similar logic to the Morse line, but taking ω_e and $\omega_e x_e$ from independently

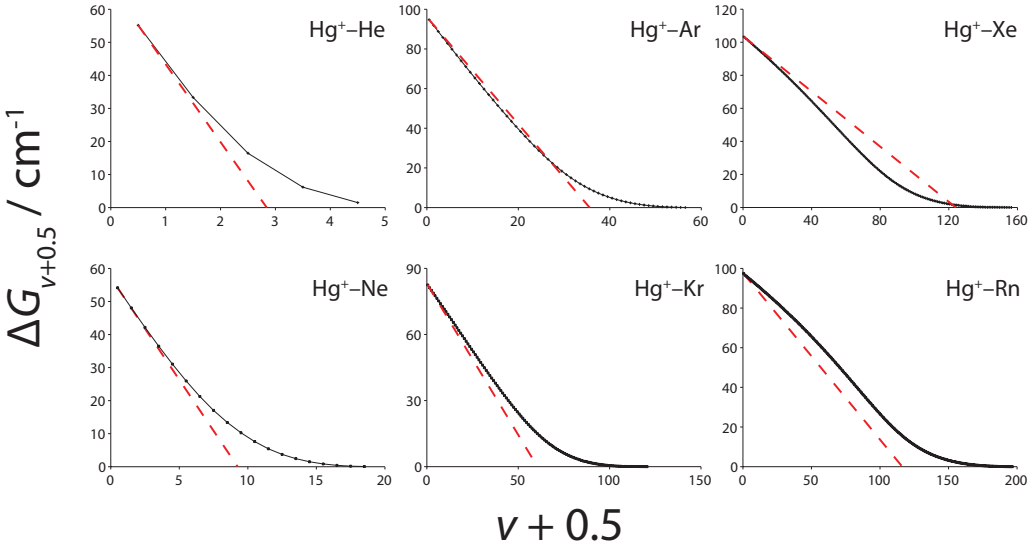


Figure 5.9: Birge-Sponer plots for the Hg^+–RG series.

fitting the lowest *three* vibrational levels $v = 0$, 1, 2 in a Birge-Sponer-type analysis to simultaneously obtain the two constants. The latter line clearly shows a better fit with the *ab initio* calculated points, demonstrating the sensitivity of those constants, and it is likely that the very bottom of the potential well has a slightly different form for this complex.

5.6 Orbital Contour Plots

Orbital contour plots have been produced for the Group 2 and 12 M^+–RG complexes, and selected plots are displayed in Figures 5.10—5.18. Specifically, the helium, argon, and xenon complexes for each metal have been displayed, with these particular complexes selected as being representative of each M^+–RG series, with the trends in these diagrams being quite systematic with increasing atomic number of rare gas (the corresponding Ne, Kr, and Rn plots have also been examined and the trends across the whole series follow what would be expected, i.e. the behaviour of the M^+–Ne complex falls between those of M^+–He and M^+–Ar etc.).

Each plot shows both an MO energy diagram as calculated at the RHF/aTZ level, and each orbital in the complex is paired with an orbital density contour plot, calculated at the same level of theory and with the same basis sets. Not all of the orbitals are plotted on these diagrams, as many of these orbital contours show completely atomic-like behaviour, and so only the valence orbitals and certain inner-valence orbitals are plotted.

5.6.1 Be^+–RG Orbital Contours

Starting with the Be^+–RG complexes in Figure 5.10, the Be^+–He plot shows almost no interaction between the metal cation and the rare gas atom, with the Be^+ and He orbitals being essentially unchanged in the complex.

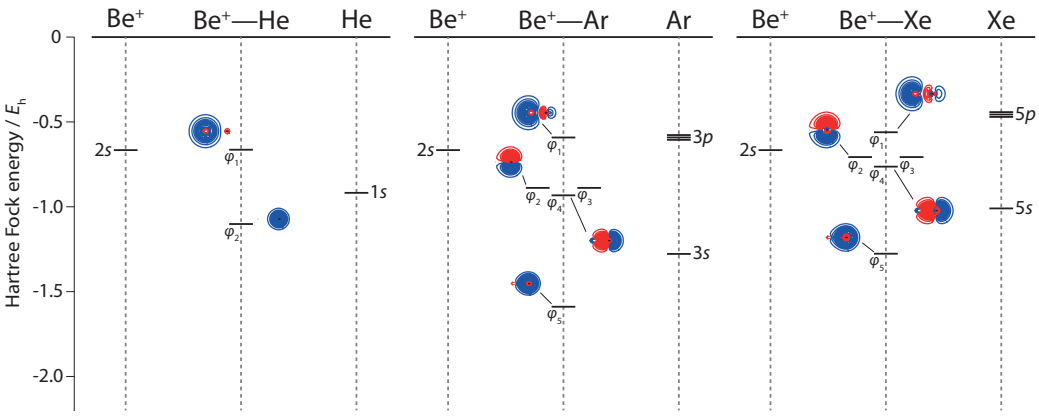


Figure 5.10: Orbital energy plots for selected members of the Be^+–RG series (see text for details).

The Be^+ 2s orbital is seen to be at almost exactly the same energy as the ϕ_1 HOMO orbital; additionally, the orbital density is almost entirely localised to the beryllium centre with only a very small amount found on the helium. The ϕ_2 contour plot shows this orbital to be completely centred on the helium, with the energy of this orbital being quite notably more negative than the atomic He 1s orbital, demonstrating the stabilisation of the helium atom upon complexation. The origin of this effect was discussed in the context of Li^+–He in Chapter 3, and is ubiquitous in these M^+–RG diatomics; throughout all of these plots, it can be seen that the rare gas orbitals are always lowered in energy upon complexation due to Coulombic stabilisation by the nearby cation. Although this effect is quite energetically significant, it is not indicative of any form of chemical interaction between the two centres, as confirmed by the close energetic correspondence between the Be^+ 2s and ϕ_1 orbitals. Overall, the plot for the Be^+–He complex is very representative of a complex bound by 'physical' interactions, a conclusion which is supported by other analyses for this complex including a value for $H(r)$ of greater than zero, as presented in Table 5.3.

Turning now to Be^+–Ar, as mentioned above, the argon orbitals upon complexation are seen to lower in energy due to Coulombic stabilisation. ϕ_5 has the form of the Ar 3s orbital, with only a small amount of density

delocalised to the beryllium centre. Inspection of ϕ_2—ϕ_4 (which correspond to the uncomplexed Ar 3p orbitals) shows an orbital contour for ϕ_2 which is essentially an argon $3p_{x/y}$ orbital (where z is the internuclear axis) with a very small amount of polarisation toward the nearby cation (ϕ_3 is the other argon $3p_{x/y}$ orbital, but the contour plot shows no change in density across the plane in which these two dimensional plots have been created). ϕ_4, which is mostly the argon $3p_z$ orbital, shows a small amount of orbital density located on the metal cation, and is also seen to have split in degeneracy from the argon $3p_{x/y}$ orbitals. In addition to this, the ϕ_1 HOMO orbital, which is mostly composed of the Be^+ 2s, shows some fairly significant contributions from the argon $3p_z$ orbital, as well as having risen in energy compared to the uncomplexed Be^+ 2s. These energetic perturbations will be due to several effects.

Addressing first the split in degeneracy of the argon 3p orbitals, since the strength of the Coulombic field will have an inverse square dependence on R, the $3p_z$ orbital, which is aligned along the internuclear axis, will feel the effect of Coulombic stabilisation more strongly since one lobe is notably closer to the cation. Destabilisation of the Be^+ 2s orbital occurs as a consequence of the presence of the nearby rare gas atom, with electronic repulsion driving the energy of this orbital up in the complex compared to in the isolated ion. There is an R dependence on the strength of both of these effects, meaning that for those complexes with shorter bond lengths these changes to orbital energies will be more pronounced. However, although these changes in energy

M^+–RG	M^+–He	M^+–Ne	M^+–Ar	M^+–Kr	M^+–Xe	M^+–Rn
Be^+–RG	0.0006	-0.0022	-0.0029	-0.0076	-0.0119	-0.0137
Mg^+–RG	0.0003	0.0001	-0.0001	-0.0004	-0.0012	-0.0017
Ca^+–RG	0.0001	0.0002	0.0019	0.0015	0.0009	0.0005
Sr^+–RG	0.0001	0.0002	0.0015	0.0013	0.0008	0.0006
Ba^+–RG	0.0001	0.0002	0.0020	0.0013	0.0008	0.0005
Ra^+–RG	0.0001	0.0002	0.0010	0.0010	0.0007	0.0005

Table 5.3: Local energy densities $H(r)$ for the Group 2 M^+–RG complexes calculated at the BCPs in atomic units (E_h $a_0{}^{-3}$)

will be present in all of these systems, they could also be taken as indicative of some chemical interaction occurring in the complex, as the symptoms of bonding/anti-bonding orbital formation appear largely the same, with one orbital rising in energy and the other lowering. Care must be taken when interpreting such situations as resulting from covalency. In the present case of Be^+–Ar, covalency is also intimated by other analyses, especially $H(r)$ seen in Table 5.3, and so the energetic perturbations seen in this complex are quite feasibly due to the formation of a bonding/anti-bonding pair of orbitals, at least partially.

As for the Be^+–Xe complex, the overall picture is similar to that of Be^+–Ar. The xenon 5s orbital is largely unchanged upon complexation as ϕ_5. Again, contour plots show that the rare gas valence np orbitals are also mostly preserved in the complex, with some density of the $5p_z$ found on Be^+ and the degeneracy lifting due to the $5p_z$ orbital lowering in energy, along with a concomitant increase in the energy of the singly occupied Be^+ orbital in ϕ_1. This destabilisation of the beryllium orbital is slightly greater in the xenon complex than it was for the argon complex and coincides with a more negative result for total local energy density for the xenon complex, which shows that this effect is due to increasing covalency. There is also seen to be a fair amount of orbital density of the ϕ_1 orbital on the rare gas atom, again similar to what is true for the Be^+–Ar complex. From this, it would seem that although the perturbations to the spatial distribution of the orbitals are not extensive, the energetic effects on these systems are quite clear, and there is fairly clear evidence of some component of covalency to these interactions.

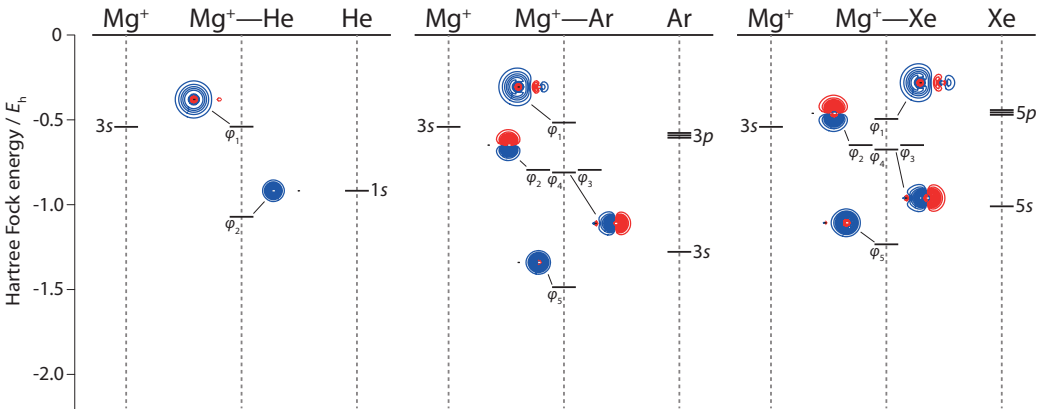


Figure 5.11: Orbital energy plots for selected members of the Mg^+–RG series (see text for details).

5.6.2 Mg^+–RG Orbital Contours

Comparing the plot for the Mg^+–He complex seen in Figure 5.11 to that of the Be^+–He complex shows strong consistency. No other method of analysis gave an indication of anything other than weak interactions in any of the Group 2 M^+–He complexes and this is borne through by these plots, with very little delocalisation of orbital density away from the orbitals of the isolated cation and rare gas, and the only energetic shift being due to the Coulombic stabilisation of the RG orbitals.

The Mg^+–Ar complex also seems similar to its beryllium-containing counterpart. Although the extent of energetic perturbation is notably less here, the extent of orbital delocalisation is similar in orbitals ϕ_1 and ϕ_4 (again being the metal cation HOMO and the highest occupied rare gas p_z orbital respectively). This difference once again falls in line with the results of $H(r)$ analysis seen in Table 5.3, with the Mg^+–Ar complex possessing a negative but extremely small value.

This relationship between beryllium and magnesium containing complexes is also true for the xenon complexes, with Mg^+–Xe yielding a plot which is similar to that of Be^+–Xe in delocalisation of orbital density across both centres (arising from interaction between the Mg^+ HOMO and the highest

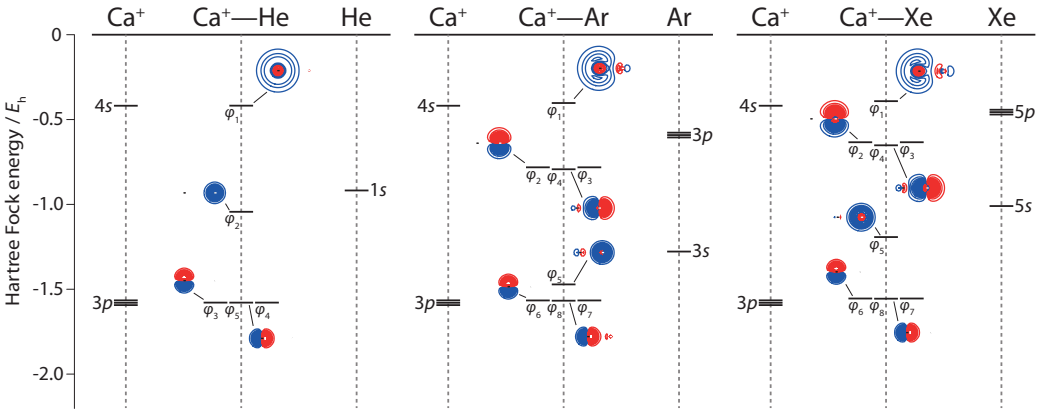


Figure 5.12: Orbital energy plots for selected members of the Ca^+–RG series (see text for details).

occupied rare gas p_z orbital), but more subtle in terms of energetics. Once more the value of $H(r)$ for this complex is seen to concur with this analysis, producing a negative but small result.

5.6.3 Ca^+–RG and Sr^+–RG Orbital Contours

As with the Be^+–He and Mg^+–He complexes, the orbitals in the Ca^+–He complex show very little in the way of deviation from atomic-like behaviour save for the Coulombic stabilisation of the helium 1s orbital—this is also seen to be true for the M^+–He complexes for M = Sr—Ra in Figures 5.13—5.15. The only difference between these complexes is the extent of Coulombic stabilisation of the He 1s orbital, which is seen to decrease with increasing atomic number of metal cation due to the increasing bond lengths. Evidently the internuclear separations in these complexes are sufficiently long to make the splitting of degenerate rare gas orbitals by the Coulombic field and the destabilisation of the M^+ valence ns orbital by electronic repulsion negligible.

For Ca^+–Ar, the outer core Ca^+ 3p orbitals are largely unaffected by the presence of the rare gas atom, showing only very slight splitting in degeneracy of the $3p_{x/y}$ and $3p_z$ orbitals, and only very slight delocalisation of orbital density from the Ca^+ centre to the argon. The Ca^+ 4s orbital is seen to

rise slightly in energy in the complex (ϕ_1) and shows some delocalisation in its contour plot; further, the Ar $3p_z$ orbital (ϕ_4) is seen to lower in energy slightly relative to the $3p_{x/y}$ orbitals ($\phi_{2/3}$). It seems as though there is some slight but meaningful interaction between the Ca^+ 4s and Ar $3p_z$ orbitals; however, there is no prediction of covalency for this complex from $H(r)$.

The plot for the Ca^+–Xe complex appears largely similar to that for the Ca^+–Ar complex. Again, there is some delocalisation of orbital density seen in ϕ_1 and some perturbation to the energies of ϕ_1 and ϕ_4, although again the sign of $H(r)$ indicates no covalency in this interaction.

Plots produced for the Sr^+–RG complexes show the same behaviour as the Ca^+–RG complexes, with orbital contours of the same form, and the lifting of degeneracies occurring to approximately the same extent. Furthermore, the values of $H(r)$ for these complexes are comparable, with both sets of values being consistently positive and of similar magnitudes. What sets apart the Ca^+–RG and Sr^+–RG contours from those of Be^+–RG and Mg^+–RG is the form of the HOMO—for the beryllium and magnesium complexes, the orbital density on the metal cation is seen to be 'pushed' away from the incoming rare gas atom along the internuclear axis. The calcium and strontium HOMOs also show this along with an additional slight build-up of orbital density off-axis, which is a result of the polarisation of the electron

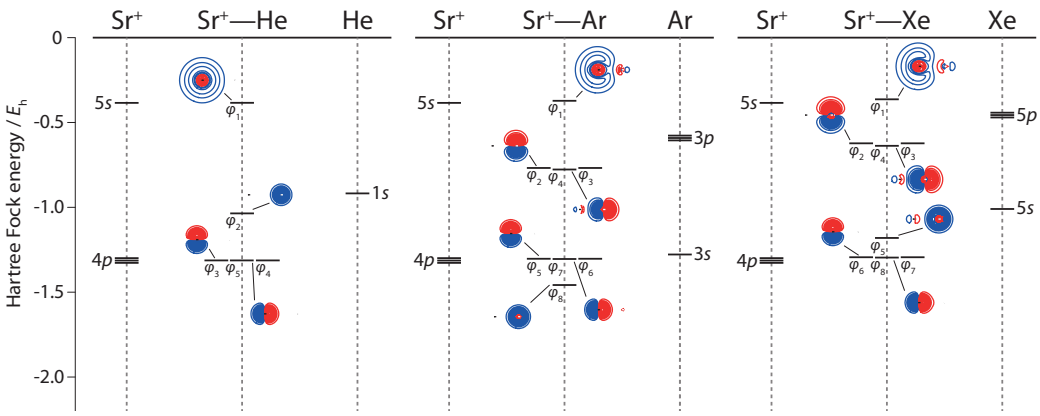


Figure 5.13: Orbital energy plots for selected members of the Sr^+–RG series (see text for details).

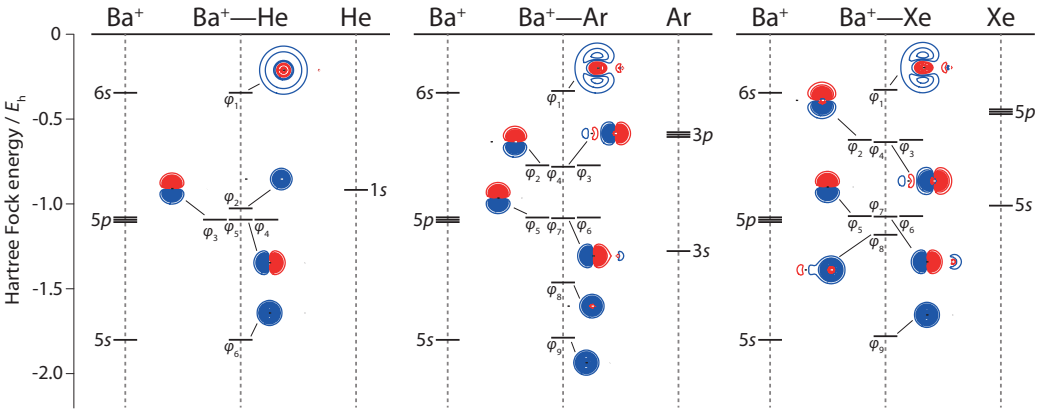


Figure 5.14: Orbital energy plots for selected members of the Ba^+–RG series (see text for details).

density into orbitals of different angular momenta—specifically, Be^+ and Mg^+ use p orbitals, and Ca^+ and Sr^+ instead use d orbitals.

5.6.4 Ba^+–RG and Ra^+–RG Orbital Contours

Moving on to the heaviest two members of Group 2, barium and radium, the Ra^+–Ar and Ra^+–Xe complexes seen in Figure 5.15 show nothing that was not seen for the Ca^+–RG and Sr^+–RG complexes, with some delocalisation of orbital density over both centres, along with slight lifting of the degeneracy of the RG valence np orbitals. The Ra^+ 6p orbitals also move apart in energy, but the energetic difference of the resulting orbitals in the complexes, ϕ_5—ϕ_7, is rather small. The form of the ϕ_1 orbitals is also similar to those of the Ca^+–RG and Sr^+–RG complexes, with slight off-axis contributions seen.

Off-axis contributions to the ϕ_1 orbitals in the Ba^+–Ar and Ba^+–Xe complexes are more marked than for the other metal series, as seen in Figure 5.14. Furthermore, the Ba^+ outer core $5p_z$ orbital shows slight delocalisation to the rare gas atoms, and slightly more delocalisation of xenon 5s density to the metal cation is seen in ϕ_8 than was seen for the Ca^+–RG or Sr^+–RG complexes.

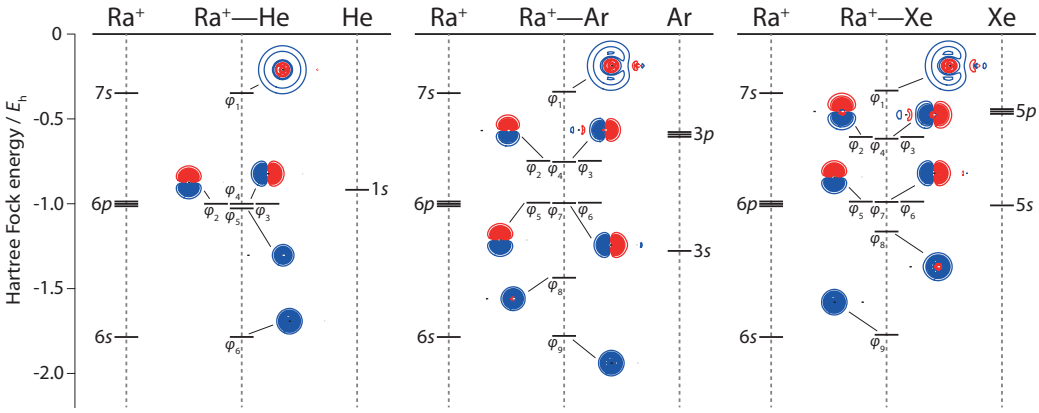


Figure 5.15: Orbital energy plots for selected members of the Ra^+–RG series (see text for details).

Overall, these effects for these two series are still very subtle, with the small amounts of delocalisation and slight energetic perturbations giving no strong argument for the formation of a bonding orbital. Once again taking the results of $H(r)$ analysis (which are all greater than zero) into consideration in conjunction with this, there appears to be no element of covalency to these interactions, with the complexes being bound entirely by 'physical' terms.

5.6.5 Zn^+–RG Orbital Contours

We now turn our attention to the Group 12 M^+–RG complexes, starting with the lightest member of the group, zinc, the orbital contour plots for which are seen in Figure 5.16. The form of the ϕ_1 orbital in Zn^+–He, which corresponds to the uncomplexed Zn^+ 4s orbital, is highly similar to those of the Group 2 M^+–He complexes, with some small delocalisation of orbital density to the helium seen and essentially no change in energy occurring

M^+–RG	M^+–He	M^+–Ne	M^+–Ar	M^+–Kr	M^+–Xe	M^+–Rn
Zn^+–RG	0.0008	0.0006	-0.0029	-0.0062	-0.0085	-0.0090
Cd^+–RG	0.0008	0.0007	0.0005	-0.0018	-0.0038	-0.0045
Hg^+–RG	0.0013	0.0011	-0.0002	-0.0037	-0.0071	-0.0080

Table 5.4: Local energy densities $H(r)$ for the Group 12 M^+–RG complexes calculated at the BCPs in atomic units (E_h a_0^{-3}).

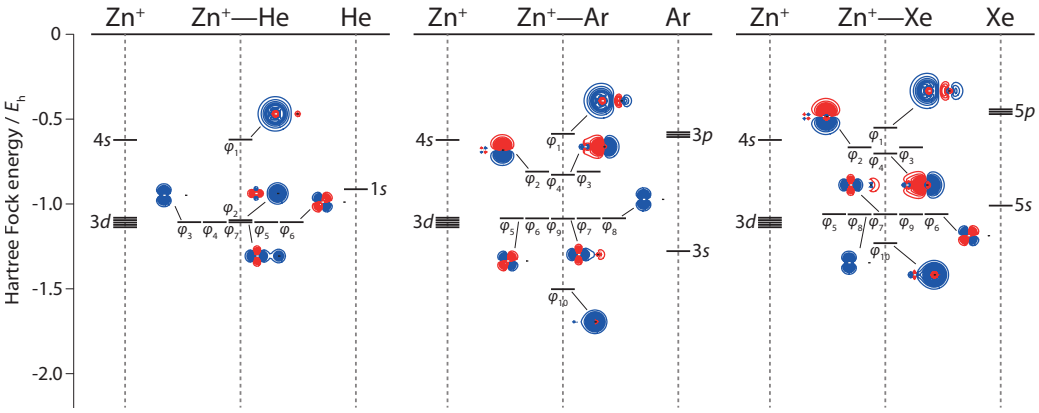


Figure 5.16: Orbital energy plots for selected members of the Zn^+–RG series (see text for details).

upon complexation. Coulombic stabilisation of the He 1s orbital leads to the analogous orbital in the complex, ϕ_2, being energetically very close to the Zn^+ 3d orbitals, ϕ_3—ϕ_7. Surprisingly for a helium complex, ϕ_2 and ϕ_7 appear very similar to one another from their contours, with both orbitals showing large amounts of density from both the Zn^+ $3d_{z^2}$ and the He 1s orbital. The phase of the lobes of the zinc orbital are of the same phase as the helium orbital in ϕ_7 and of opposite phases in ϕ_2, creating an impression of a bonding/anti-bonding pair of orbitals. Despite this seemingly strong interaction, the splitting in degeneracy of the Zn^+ 3d orbitals is close to zero. Taking into account the positive value of $H(r)$ for this complex as presented in Table 5.4, it seems that despite some delocalisation of the outer core orbitals, there is no covalent character to this interaction. It is likely that the mixed character of ϕ_2 and ϕ_7 is purely due to the energetic match, and it is noteworthy that the contributions from each atom look as they would be expected to in the corresponding atoms, with no change in shape effected by complexation.

Interactions between Zn^+ and Ar show quite notably different results. A negative value for $H(r)$ is obtained for this particular complex, and this intimation of covalency is sustained by the orbital contour plot. The Ar 3p orbitals are seen to drop in energy below the Zn^+ 4s orbital, and there

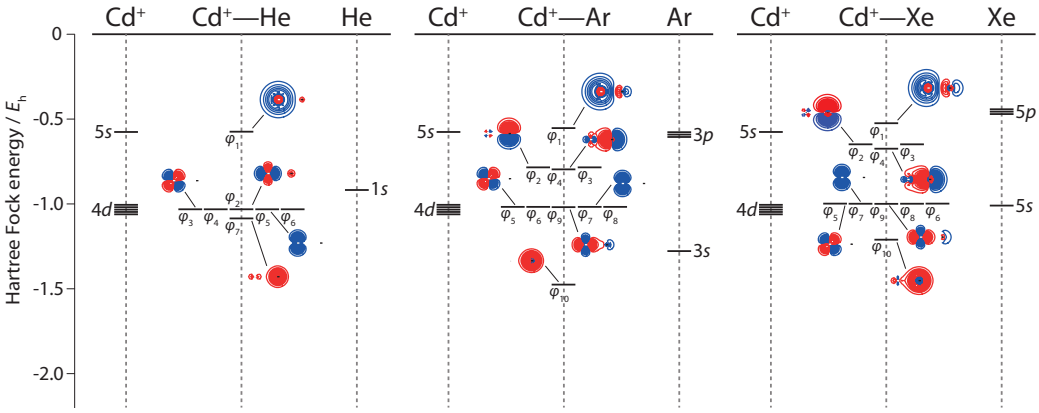


Figure 5.17: Orbital energy plots for selected members of the Cd^+–RG series (see text for details).

is a noticeable split in degeneracy seen between $\phi_{2/3}$ and ϕ_4, along with a roughly commensurate rise in energy of the Zn^+ 4s orbital in the complex. There is a fair degree of delocalisation in ϕ_1 and ϕ_4, and unlike what was seen for the Group 2 M^+–Ar complexes, the Ar $3p_{x/y}$ orbitals ($\phi_{2/3}$) also show very small amounts of delocalisation to the metal cation as they can now interact with a d orbital of appropriate symmetry. Information gleaned from this plot is thus seen to agree well with the result of $H(r)$, in that there is a degree of covalency in the form of this interaction.

The heaviest Zn^+–RG complex shown here, Zn^+–Xe, has a plot similar to that of Zn^+–Ar. Contour plots for all orbitals show similar albeit more extensive delocalisation in the Zn^+–Xe complex, and similarly the energetic perturbations to ϕ_1 and ϕ_4 are greater for the xenon complex. There is also an increase seen in the magnitude of $H(r)$, with the value for the Zn^+–Xe complex being more negative, the ramification being that the increasing energetic disturbances in this complex are due to increasing strength of covalency.

5.6.6 Cd^+–RG Orbital Contours

Orbital delocalisation in the Cd^+–He complex in Figure 5.17 is essentially the same as for Zn^+–He. The form of ϕ_1 is largely the same with both metal cations, and similar interactions are seen between the metal cation outer core d_{z^2} and helium 1s orbitals in the complex in orbitals ϕ_2 and ϕ_7 (although it should be noted that the ordering of these orbitals is now reversed), although with Cd^+ this effect is less pronounced. Also similar to Zn^+–He is the result of $H(r)$ in Table 5.4, which is equal to that of Zn^+–He in sign and very similar in magnitude.

Cd^+–Ar also shows essentially the same behaviour as Zn^+–Ar, with the same patterns of orbital delocalisation and energetic perturbations seen. In this case, however, the value of $H(r)$ is positive, highlighting the necessity of caution in assigning covalency; although there are the expected effects of covalency observed in the contours, there does not seem to be the requisite stabilisation of electron density at the bond critical point.

Changing the rare gas atom to xenon is seen to make very little change to the form of the contour plots from those of Cd^+–Ar, with the same delocalisation patterns seen. The energetics are also highly similar, with the only substantial difference being an increase in splitting in the Xe 5p orbitals in orbitals $\phi_{2/3}$ and ϕ_4. Despite these similarities, $H(r)$ analysis returns a result of less than zero. It seems that for these complexes the balance of whether the interaction contains a degree of covalency or not is very sensitive, and the very small magnitudes of $H(r)$ mean that even when covalency is present the extent of its effects are only very slight, with the leading term of the attractive forces still being the induction terms.

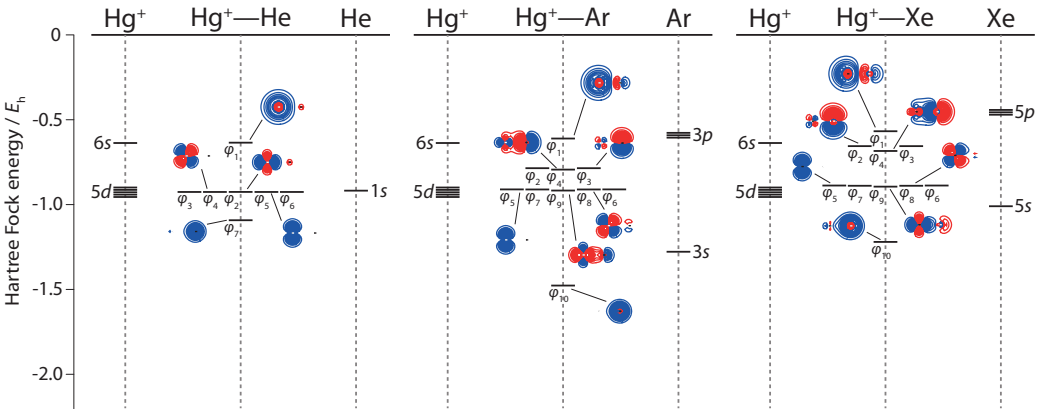


Figure 5.18: Orbital energy plots for selected members of the Hg^+–RG series (see text for details).

5.6.7 Hg^+–RG Orbital Contours

Changes seen between the Zn^+–RG and Cd^+–RG complexes are continued with the Hg^+–RG series presented in Figure 5.18. Less orbital delocalisation occurs in Hg^+–He, and delocalisation in Hg^+–Ar and Hg^+–Xe is more extensive than was seen for the zinc and cadmium complexes. Effects on orbital energetics upon complexation are also more exaggerated in Hg^+–Ar and Hg^+–Xe, with the splitting in degeneracy of the rare gas valence np orbitals being greater than for the other Group 12 complexes.

Interestingly, there is some involvement of the inner-valence 5d orbitals in Hg^+–Ar. Although some delocalisation was noted for Zn^+–He and regarded as purely due to good energetic matching, for Hg^+–Ar the $5d_{z^2}$ orbital in particular shows strong mixing with a RG p_z orbital in ϕ_9, with obvious overlapping of orbitals. There is slightly greater lifting in degeneracy of the Hg^+ 5d orbitals in this complex than any other, suggesting the possibility that this is a stronger interaction than that discussed for Zn^+–He. The fairly low (yet negative) value of $H(r)$ for this complex shows that this effect is still only weak, however, which is perhaps surprising given the strong mixing in many of the orbitals for this complex. Again, this demonstrates the importance of considering the results of complementary analyses when

divining the form of interaction in these complexes.

Values of $H(r)$ for the mercury complexes are closer to those of the corresponding zinc complexes, especially so for the heavier rare gases. This is a consequence of the relativistic and lanthanide contractions experienced by mercury which brings its properties more into line with those of zinc, as was also discussed for the spectroscopic constants.

5.7 Partial Atomic Charge Analyses

5.7.1 Group 12 Partial Atomic Charges

Partial atomic charges have been calculated using NPA and AIM analyses, as well as Mulliken analysis, and are collected in Tables 5.5 and 5.6. There is good agreement between all three methodologies for M = Zn—Hg, especially so between NPA and Mulliken. AIM charges are seen to diverge slightly for the heavier of these species, although the maximum discrepancy between NPA and AIM (seen for Hg^+–Rn) is only 0.08 *e*. Most importantly, all sets of results give the same trends of increasing partial charge on the rare gas atom as its atomic number increases.

Data for the Group 12 partial atomic charges supports what was seen for the orbital contour plots. The helium complexes, where there is close to zero charge placed on the rare gas atom, showed very little splitting of degenerate d orbitals on the Group 12 cation, indicating that there is largely atomic-like electronic structure preserved in the complex. Although there is some orbital delocalisation seen, especially for ϕ_2 and ϕ_7 in Zn^+–He, the constituent atomic orbitals are doubly occupied as are the resulting orbitals in the complex, leaving no impetus for movement of charge. Further, ϕ_1 shows that the metal cation valence *n*s orbital is essentially non-interacting, leaving the excess positive charge on the metal centre. A similar outcome is

obtained for the neon complexes, wherein the charge apportioned to neon is also close to zero.

Calculated charges show there is some slight migration of charge taking place in the argon complexes, and accordingly there is a more obvious delocalisation of orbital density in the orbital contours for ϕ_1 and ϕ_4. This small movement of charge also coincides with a prediction of covalency by $H(r)$ for the zinc and mercury complexes—although this is not also true for Cd^+–Ar, this complex does appropriately have the lowest charge on the rare gas. The metal cation valence ns orbital is singly occupied, and ϕ_4, which seemingly contains some metal ns orbital character, is doubly occupied, which would necessitate some movement of electron density from the RG orbitals into M^+ ones. Thus, although these partial atomic charges could be describing a true charge transfer effect, it is more likely that they are describing mixing of orbital character upon complexation—where this effect is significant, this results in a prediction of covalency by $H(r)$ analysis. In fact, the possibility of this being a true charge transfer effect without covalency is not supported by the relative ordering of the orbitals, since the

			M^+–He	M^+–Ne	M^+–Ar	M^+–Kr	M^+–Xe	M^+–Rn
Zn	NPA	Q_{Zn}	1.00	1.00	0.96	0.92	0.86	0.82
		Q_{RG}	0.00	0.00	0.04	0.08	0.14	0.18
	AIM	Q_{Zn}	1.00	1.01	0.95	0.91	0.83	0.78
		Q_{RG}	0.00	-0.01	0.05	0.09	0.17	0.22
	Mulliken	Q_{Zn}	1.00	0.99	0.96	0.93	0.86	0.79
		Q_{RG}	0.00	0.01	0.04	0.07	0.14	0.21
Cd	NPA	Q_{Cd}	1.00	1.00	0.97	0.95	0.90	0.86
		Q_{RG}	0.00	0.00	0.03	0.05	0.10	0.14
	AIM	Q_{Cd}	1.00	1.01	0.97	0.93	0.86	0.81
		Q_{RG}	0.00	-0.01	0.03	0.07	0.14	0.19
	Mulliken	Q_{Cd}	1.00	0.99	0.96	0.95	0.90	0.85
		Q_{RG}	0.00	0.01	0.04	0.05	0.10	0.15
Hg	NPA	Q_{Hg}	1.00	1.00	0.96	0.91	0.81	0.74
		Q_{RG}	0.00	0.00	0.04	0.09	0.19	0.26
	AIM	Q_{Hg}	1.00	1.00	0.95	0.88	0.74	0.66
		Q_{RG}	0.00	0.00	0.06	0.13	0.26	0.34
	Mulliken	Q_{Hg}	1.00	0.99	0.96	0.92	0.83	0.75
		Q_{RG}	0.00	0.01	0.04	0.08	0.17	0.25

Table 5.5: Partial atomic charges for the Group 12 M^+–RG complexes, calculated using NPA and AIM methodologies, in units of elementary charge e.

doubly occupied RG atomic orbital is closer to the complex orbital ϕ_4 than it is to the singly occupied ϕ_1 complex orbital.

As the rare gas is varied from Ar through to Rn, the charge on the rare gas atom increases. Again, this coincides with delocalisation of orbital density in the orbital contour plots, an increase in splitting of formerly degenerate atomic orbitals in the complex, and increasingly negative values of $H(r)$. Inspection of the orbital contour plots reveals that this is in part due to the energetic match between orbitals on the cation and the rare gas. The RG valence np orbitals (ϕ_2—ϕ_4 for RG = Ar and Xe in Figures 5.16—5.18) are seen to approach more closely the energy of the singly occupied valence ns orbital of the metal cation for M^+–Xe than M^+–Ar, facilitating a stronger interaction between centres as Group 18 is descended.

Magnitude of charge transfer as a function of metal proceeds Hg>Zn>Cd, and this follows the ordering of the position of the singly-occupied orbital (which is energetically lowest for Hg^+). Relative magnitudes of $H(r)$ do not quite follow this ordering however, as the magnitudes of $H(r)$ are largest for the Zn complexes (although they are lowest for the Cd complexes, corresponding to the above discussion). Attempting to invoke only energetic similarities to explain strengths of covalent interactions would be an over-simplification, and it is also probable that the shorter bond lengths for the zinc complexes will give more efficient orbital overlaps, contributing to a stronger covalent interaction in those cases.

5.7.2 Group 2 Partial Atomic Charges

The results from the different methods of charge analysis for Group 2 are in somewhat poor agreement, with the three data sets becoming more divergent with increasing atomic number of rare gas atom. NPA and AIM give very similar results for M = Ca—Ra, as does Mulliken (although

this agreement becomes more imperfect for the heavier rare gases). These complexes all show very low charge on the rare gas atom, which increases slightly as the size of rare gas increases. As was concluded from other analyses, it seems that these complexes are bound entirely by 'physical' effects without any covalency.

For M = Be and Mg, more obvious differences between the results creep in for the heavier rare gases. For the magnesium series, NPA and AIM furnish reasonably consistent results of small amounts of charge transfer (with a larger transfer coming from NPA), although Mulliken predicts a notably larger transfer of charge. These effects are magnified significantly in the beryllium series. Examining the largest differences seen, for the case of Be^+–Rn, AIM yields only a very small charge of 0.03 e on the rare gas, NPA results give a rather more significant movement of 0.22 e, and Mulliken charges place more than 0.5 e on radon.

In contrast to what was seen for Group 12, it seems that describing the partial atomic charges for the Group 2 M^+–RG complexes is rather more challenging, especially so for the beryllium and magnesium complexes with the heavier rare gases, since NPA, AIM, and Mulliken give significantly different results. It is perhaps unsurprising that Mulliken charges provide the most questionable result with an unexpectedly high charge on the rare gas atom, since Mulliken analysis has known weaknesses as outlined in Section 2.3.1. Large differences between NPA and AIM charges are more puzzling. On the grounds of energetic match between M^+ and RG orbitals, the low charge transfer of the M = Ca—Ra complexes relative to the Group 12 analogues is quite understandable as there is clearly a greater separation of the M^+ ns and RG np orbitals in the Group 2 M^+–RG complexes. Along the same line of reasoning, the Mg^+–RG and Be^+–RG series exhibit a closer energetic match between the same orbitals, and so the results in those cases

			M^+–He	M^+–Ne	M^+–Ar	M^+–Kr	M^+–Xe	M^+–Rn
Be	NPA	Q_{Be}	1.00	0.99	0.91	0.87	0.82	0.78
		Q_{RG}	0.00	0.01	0.09	0.13	0.18	0.22
	AIM	Q_{Be}	1.00	1.02	1.02	1.00	0.98	0.97
		Q_{RG}	0.00	-0.02	-0.02	0.00	0.02	0.03
	Mulliken	Q_{Be}	1.00	0.98	0.85	0.80	0.56	0.47
		Q_{RG}	0.00	0.02	0.15	0.20	0.44	0.53
Mg	NPA	Q_{Mg}	1.00	1.00	0.98	0.96	0.94	0.92
		Q_{RG}	0.00	0.00	0.02	0.04	0.06	0.08
	AIM	Q_{Mg}	1.00	1.01	1.02	1.01	0.99	0.98
		Q_{RG}	0.00	-0.01	-0.02	-0.01	0.01	0.02
	Mulliken	Q_{Mg}	1.00	0.99	0.98	0.93	0.85	0.77
		Q_{RG}	0.00	0.01	0.02	0.07	0.15	0.23
Ca	NPA	Q_{Ca}	1.00	1.00	0.99	0.98	0.97	0.96
		Q_{RG}	0.00	0.00	0.01	0.02	0.03	0.04
	AIM	Q_{Ca}	1.00	1.01	1.02	1.01	1.00	1.00
		Q_{RG}	0.00	-0.01	-0.02	-0.01	0.00	0.01
	Mulliken	Q_{Ca}	1.00	0.99	0.97	0.96	0.93	0.89
		Q_{RG}	0.00	0.01	0.03	0.04	0.07	0.11
Sr	NPA	Q_{Sr}	1.00	1.00	0.99	0.99	0.98	0.97
		Q_{RG}	0.00	0.00	0.01	0.01	0.03	0.03
	AIM	Q_{Sr}	1.00	1.01	1.02	1.02	1.00	1.00
		Q_{RG}	0.00	-0.01	-0.02	-0.02	0.00	0.00
	Mulliken	Q_{Sr}	1.00	0.99	0.98	0.98	0.95	0.90
		Q_{RG}	0.00	0.01	0.02	0.02	0.05	0.10
Ba	NPA	Q_{Ba}	1.00	1.00	0.99	0.99	0.98	0.97
		Q_{RG}	0.00	0.00	0.01	0.01	0.02	0.03
	AIM	Q_{Ba}	1.00	1.01	1.01	1.01	0.99	0.99
		Q_{RG}	0.00	-0.01	-0.01	-0.01	0.01	0.01
	Mulliken	Q_{Ba}	1.00	0.99	0.98	0.98	0.97	0.93
		Q_{RG}	0.00	0.01	0.02	0.02	0.03	0.07
Ra	NPA	Q_{Ra}	1.00	1.00	1.00	0.99	0.98	0.98
		Q_{RG}	0.00	0.00	0.00	0.01	0.02	0.02
	AIM	Q_{Ra}	1.00	1.01	1.02	1.02	1.01	1.00
		Q_{RG}	0.00	-0.01	-0.02	-0.02	-0.01	0.00
	Mulliken	Q_{Ra}	1.00	0.99	0.97	0.97	0.97	0.94
		Q_{RG}	0.00	0.01	0.03	0.03	0.03	0.06

Table 5.6: Partial atomic charges for the Group 2 M^+–RG complexes, calculated using NPA and AIM methodologies, in units of elementary charge *e*.

could be expected to be closer to what was seen for Group 12. Results from NPA seem to concur with this, with charge transfer for the beryllium series being comparable to that of the zinc series, but AIM calculations predict close to zero charge transfer across the entire range of Group 2 M^+–RG complexes. Despite these partial charges, $H(r)$ from the same AIM calculations shows some covalency for the Be^+–RG series (save for Be^+–He), as well as Mg^+–RG for RG = Ar—Rn; further, for the Be^+–RG complexes, the magnitude of $H(r)$ is generally larger than for the corresponding Group 12 complexes.

5.8 Comparison of Interactions in Groups 2 and 12 M^+–RG Complexes and Concluso ry Remarks

The $H(r)$ parameter from AIM implies that for M = Ca—Ra, these complexes are non-covalent, and although the orbital contour plots show some slight orbital delocalisation and small energetic perturbations in the form of formerly degenerate orbitals moving apart in energy, these effects are only slight and can be explained without invoking covalency. Further, the contours show the electron density on the metal centre distorting through sp- or sd-hybridisation in order to move electron density away from the internuclear region. This reduces the repulsion interaction and allows the rare gas atom to move closer, concurrently increasing the strength of the ion/induced-dipole force (as well as higher-order induction terms). In this way, moderately high binding energies are achieved in these 'physically'-bound complexes, although it has been suggested previously that hybridisation effects on the metal centre could be described as 'chemical' in nature.[7,8]

The lighter two members of Group 2, Be and Mg, exhibit some covalency in their complexes with the heavier rare gases, quite notably so for beryllium. Along with a negative sign of $H(r)$, this is manifested as quite strong orbital delocalisation and large splitting of the rare gas atomic np orbitals upon complexation, with a bonding/antibonding pair of orbitals forming between the singly-occupied metal cation ns orbital and the highest occupied rare gas $n\mathrm{p}_z$. Closer energetic matching between these sets of orbitals for M = Be and Mg facilitates this interaction, and is what sets these complexes apart from M = Ca—Ra. Induction terms in these complexes will also be stronger than for M = Ca—Ra due to the shorter bond lengths, further increasing

the overall dissociation energy.

Analysis of the Group 12 M^+–RG complexes gives clear indications of covalency in their interactions with the heavier rare gases. Total local energy density analysis yields a negative sign, indicating covalency. Orbital contour plots concur with this as delocalisation effects are stronger here, with interactions between the M^+ ns and RG $n\mathrm{p}_z$ orbitals resulting in the formation of bonding/antibonding orbitals, similar to the beryllium and magnesium complexes with the heavier rare gases. This comparability is due in part to the energetics of the cation ns orbital, which is energetically similar to the Be^+ ns orbital.

There is also, as seen from the orbital contour plots, some distortion of the electron density on the metal centre, although the extent of this hybridisation is rather less than that of the heavier members of Group 2. As was mentioned above, the energetic accessibility of the np or nd orbitals in Group 2 makes hybridisation in those complexes easily achieved, whereas for Group 12 this becomes significantly more energetically expensive.

Interestingly, contour plots for Group 12 also show some interaction in the inner-valence (n-1)d orbitals. Whilst this effect is quite minimal for the majority of these complexes, the delocalisation appears significant between the M^+ (n-1)d_{z^2} and the He 1s orbital in Zn^+–He, and also for the metal (n-1)d_{z^2} and a RG p_z orbital in Hg^+–Ar. This effect is seen to be much more significant for the mercury complex, since the individual atomic contributions appear unperturbed in Zn^+–He and the orbital energetics are largely unaffected by complexation. Conversely, Hg^+–Ar shows much more distortion to the shape of the orbitals involved, as well as the orbital energies responding to the presence of the other atom. These additional effects are not seen in the Group 2 complexes, where the M^+ (n-1)p orbitals are unaffected by the presence of the RG atom.

Covalent effects are reflected in the equilibrium dissociation energies of the Group 12 complexes, which are much higher than for the M = Ca—Ra complexes with the heavier rare gases, and more in line with the M = Be and Mg complexes. Of the series which exhibit covalency, the magnesium complexes are the most weakly bound, as the position of the M^+ ns orbital is energetically furthest from the RG np orbitals there. Of the Group 12 complexes, the Cd^+–RG series is the least strongly bound, which is again in line with the energetic position of the M^+ ns orbital relative to the highest occupied rare gas p_z orbital. The Be^+–RG series is the most strongly bound out of both Groups 2 and 12, due in part to favourable energetics in that case, along with decreased repulsion owing to the low electron count on Be^+, and the subsequent increase that this produces in the induction terms due to decreased bond length.

Bibliography

[1] J. Lozeille, E. Winata, P. Soldan, E. P. F. Lee, L. A. Viehland and T. G. Wright, *Phys. Chem. Chem. Phys.*, 2002, **4**, 3601–3610.

[2] L. A. Viehland, J. Lozeille, P. Soldan, E. P. F. Lee and T. G. Wright, *The Journal of Chemical Physics*, 2003, **119**, 3729–3736.

[3] L. A. Viehland, J. Lozeille, P. Soldan, E. P. F. Lee and T. G. Wright, *The Journal of Chemical Physics*, 2004, **121**, 341–351.

[4] H. L. Hickling, L. A. Viehland, D. T. . Shepherd, P. Soldan, E. P. F. Lee and T. G. Wright, 2004, **6**, 4233–4239.

[5] W. Breckenridge, V. L. Ayles and T. G. Wright, *Chemical Physics*, 2007, **333**, 77–84.

[6] M. F. McGuirk, L. A. Viehland, E. P. F. Lee, W. H. Breckenridge, C. D. Withers, A. M. Gardner, R. J. Plowright and T. G. Wright, *The Journal of Chemical Physics*, 2009, **130**, 194305.

[7] A. M. Gardner, C. D. Withers, T. G. Wright, K. I. Kaplan, C. Y. N. Chapman, L. A. Viehland, E. P. F. Lee and W. H. Breckenridge, *The Journal of Chemical Physics*, 2010, **132**, 054302.

[8] A. M. Gardner, C. D. Withers, J. B. Graneek, T. G. Wright, L. A. Viehland and W. H. Breckenridge, *The Journal of Physical Chemistry A*, 2010, **114**, 7631–7641.

[9] A. Yousef, S. Shrestha, L. A. Viehland, E. P. F. Lee, B. R. Gray, V. L. Ayles, T. G. Wright and W. H. Breckenridge, *The Journal of Chemical Physics*, 2007, **127**, 154309.

[10] W. H. Breckenridge, V. L. Ayles and T. G. Wright, *The Journal of Physical Chemistry A*, 2008, **112**, 4209–4214.

[11] E. Qing, L. A. Viehland, E. P. F. Lee and T. G. Wright, *The Journal of Chemical Physics*, 2006, **124**, 044316.

[12] E. P. Lee, B. R. Gray, N. A. Joyner, S. H. Johnson, L. A. Viehland, W. Breckenridge and T. G. Wright, *Chemical Physics Letters*, 2007, **450**, 19–24.

[13] B. R. Gray, E. P. F. Lee, A. Yousef, S. Shrestha, L. A. Viehland and T. G. Wright, *Molecular Physics*, 2006, **104**, 3237–3244.

[14] A. M. Gardner, K. A. Gutsmiedl, T. G. Wright, W. H. Breckenridge,

C. Y. N. Chapman and L. A. Viehland, *The Journal of Chemical Physics*, 2010, **133**, 164302.

[15] A. M. Gardner, K. A. Gutsmiedl, T. G. Wright, E. P. F. Lee, W. H. Breckenridge, S. Rajbhandari, C. Y. N. Chapman and L. A. Viehland, *The Journal of Physical Chemistry A*, 2011, **115**, 6979–6985.

[16] J. P. Harris, A. M. Gardner, T. G. Wright, W. H. Breckenridge and L. A. Viehland, *The Journal of Physical Chemistry A*, 2012, **116**, 4995–5007.

[17] P. Pyykkö, *Journal of the American Chemical Society*, 1995, **117**, 2067–2070.

[18] B. Prascher, D. Woon, K. Peterson, J. Dunning, ThomH. and A. Wilson, *Theoretical Chemistry Accounts*, 2011, **128**, 69–82.

[19] K. A. Peterson and C. Puzzarini, *Theoretical Chemistry Accounts*, 2005, **114**, 283–296.

[20] K. Peterson, Basis sets for Ca—Ra, private communication.

[21] A. Halkier, T. Helgaker, P. Jørgensen, W. Klopper and J. Olsen, *Chemical Physics Letters*, 1999, **302**, 437–446.

[22] R. J. LeRoy, Level 8.0: A Computer Program for Solving the Radial Schrödinger Equation for Bound and Quasibound Levels, University of Waterloo Chemical Physics Research Report No. CP-663, 2007; see http://leroy.uwaterloo.ca/programs/.

[23] G. Schaftenaar and J. H. Noordik, *Journal of Computer-Aided Molecular Design*, 2000, **14**, 123–134.

[24] M. J. Frisch, et al., Gaussian 09, Revision D.01, Gaussian, Inc., Wallingford CT, 2010.

[25] E. D. Glendening, J. K. Badenhoop, A. E. Reed, J. E. Carpenter, J. A. Bohmann, C. M. Morales, C. R. Landis and F. Weinhold, NBO 6.0, Theoretical Chemistry Institute, University of Wisconsin, Madison, 2013.

[26] T. A. Keith, T. K. Gristmill Software, AIMAll, Overland Park, KS, 2011, see aim.tkgristmill.com.

[27] K. Abdessalem, L. Mejrissi, N. Issaoui, B. Oujia and F. X. Gadéa, *The Journal of Physical Chemistry A*, 2013, **117**, 8925–8938.

[28] N. X. Hong, S. W. Wen, W. Shuai and S. D. Heng, *Canadian Journal of Chemistry*, 2014, **92**, 397–405.

[29] T. G. Wright and W. H. Breckenridge, *The Journal of Physical Chemistry A*, 2010, **114**, 3182–3189.

[30] R. J. LeRoy and R. B. Bernstein, *The Journal of Chemical Physics*, 1970, **52**, 3869–3879.

Chapter 6

Theoretical Results on the HM^+–RG Complexes

6.1 Introduction

As seen previously in Chapter 5, interactions in Group 2 M^+–RG complexes are, for the most part, dominated by 'physical' forces, with the interaction potential dependent on an often delicate balance between dispersion, repulsion, and ion/induced-dipole interactions. As was also demonstrated, an important part of the interaction in these systems is the moving of electron density around the metal atom, away from the internuclear region by orbital hybridisation. It would seem plausible that if another atom were used to 'fix' this distorted electron density to one side of the metal, the interaction between metal centre and rare gas atom could potentially see an increase in strength.

A likely (and simple) candidate for such fixing of the electron density is a hydrogen atom—Chapter 4 has already highlighted the strength of interaction between Group 2 metals and the hydride anion, which results in the formation of a covalent bond between the two centres. Moving to the corresponding cationic series of complexes HM^+, the strength of interaction could be expected to increase. Removing two electrons from these species

will depopulate the 'antibonding' orbital formed through interaction of the highest occupied metal orbital and the hydrogen 1s, as well as decrease the electronic repulsion.

Here then, the triatomic HM^+–RG (M = Group 2 metal, RG = rare gas) series of complexes are examined, with the expectation being that not only will the strength of the hydrogen-metal interaction be increased compared to the anionic species, but more pertinently that the binding of the rare gas to the metal centre should be stronger relative to the M^+–RG diatomics.

6.2 Computational Methodology

Geometry optimisations were performed on the HM^+–RG and HM^+ series of complexes (where M = Be, Mg, Ca, Sr, Ba, and Ra, and RG = He, Ne, Ar, Kr, Xe, and Rn) using MP2 theory as implemented in the MOLPRO *ab initio* package.[1] The basis sets used were of quadruple-ζ quality; more specifically, H, Be, and He used aug-cc-pVQZ basis sets, Mg, Ne, and Ar used aug-cc-pwCVQZ basis sets, and the heavier elements (Ca—Ra and Kr—Rn) used aug-cc-pwCVQZ-PP basis sets along with a fully relativistic small-core pseudopotential ECPXXMDF. ECPs used were as follows; Ca and Kr—ECP10MDF, Sr and Xe—ECP28MDF, Ba—ECP46MDF, Rn—ECP60MDF, and Ra—ECP78MDF.

Beryllium, magnesium, and neon had their 1s orbitals frozen in all calculations, and the 1s, 2s, and 2p orbitals of argon were similarly frozen. For the heavier rare gases krypton, xenon, and radon, the 'outer core' (n-1)s and (n-1)p orbitals were frozen (where the n orbitals are valence). All other orbitals were correlated for all calculations (save for those orbitals which were described by the ECPs).

The convergence of each geometry optimisation was checked by calculating harmonic vibrational frequencies—for the cases where imaginary

frequencies were found, the geometry optimisation was repeated with more stringent convergence criteria applied to the energy and gradient. However, in some cases the trends in the real calculated harmonic frequencies between complexes seemed erratic. As the frequency calculations conducted in MOLPRO used numerical gradients, additional calculations were conducted using Gaussian 09[2] where analytical gradients are available for MP2, the results of which were found to show smoother trends and so these are the results presented here. Similar results would also be obtainable by use of smaller step sizes in the numerical gradient calculations, but at greater computational expense.

Single-point CCSD(T) dissociation energies for loss the of the rare gas atom were calculated at each MP2 optimised geometry using basis sets of the same design as those mentioned above, of quadruple- and quintuple-ζ quality. The results of these calculations allowed extrapolation of the binding energy to the basis set limit (see Section 2.2.1). Further, dissociation energies were also calculated using the same basis sets and applying full counterpoise correction.

Additional analyses similar to those undertaken in earlier chapters are also discussed here; NPA and AIM partial atomic charge analyses were undertaken on the QCISD density calculated using triple-ζ basis sets analagous to those stated above, using the NBO6[3] and AIMAll[4] programs respectively. Contour plots of the natural orbitals are also presented, created using the same triple-ζ basis sets and visualised using MOLDEN.[5]

6.3 Interactions in the HM^+ Complexes

6.3.1 Previous Results

In contrast to previous chapters, the species under scrutiny here are triatomics. However, interest is primarily focussed on the interaction between the HM^+ unit and the RG atom, and as such it is first important to understand the HM^+ unit. To this end, the results of calculations focussing on the isolated HM^+ species were conducted using the same methodology as outlined above. Spectroscopic parameters for these species are collected in Table 6.1. Several previous studies have been conducted on the Group 2 HM^+ series to which the present results can be compared.

For HBe^+, a recent study from 2013 by Koput[6] used multi-reference averaged coupled-pair functional (MR-ACPF) methodology with up to septuple-ζ sized basis sets, the results from which also included correction factors for relativistic and adiabatic effects. Spectroscopic parameters from that study can be seen to be in good agreement with the CCSD(T) calculations, although agreement for the harmonic vibrational frequency, ω_e, is slightly poorer. An experimental result is also available for comparison from Coxon and Colin in which the emission spectrum was recorded,[7] the bond length from which is in excellent agreement. The experimental dissociation energy is in good agreement also, although it is a little higher than predicted by the theoretical results.

Several previous studies also exist for HMg^+. Aymar *et al.* conducted a study using the Configuration Interaction by Perturbation of a multiconfiguration wavefunction Selected Iteratively (CIPSI) approach,[8] the results from which give reasonable agreement with the current CCSD(T) results, with a longer bond length and lower binding energy. A study from Abe *et*

al.[9] used various combinations of basis sets and methodologies, the highest level of which was CCSD(T) with cc-pCV5Z basis sets. This produced a value for R_e which is longer than the CCSD(T) results here, giving fairly poor agreement, although the binding energy from that study is in excellent agreement with the present value. An experimental study from Dalleska *et al.*[10] used guided ion beam mass spectrometry to investigate the kinetic energy dependence of reactions to form the HM^+ species, which also yielded zero-point dissociation energies, D_0, which can be used in conjunction with the values of ω_e calculated here to yield values for D_e. The uncertainties associated with these experimental results are sizeable, and so although the value of 16 500 cm^{-1} for HMg^+ seems to be in poor agreement with CCSD(T) results, the associated uncertainty is $\pm$500 cm^{-1}, meaning the calculated value falls within the experimental range. Another experimental study is also available for this complex, from Balfour.[11] R_e from that study is in fairly poor agreement with the present CCSD(T) study, but in excellent agreement with the other studies mentioned here. Balfour's D_e is in good agreement with both CCSD(T) results.

Abe *et al*'s[9] results on HCa^+, again from CCSD(T)/cc-pCV5Z calculations, are in poorer agreement than they were for the magnesium complex. Again, the predicted bond length is longer than the present result, and again the binding energy is seen to be in good agreement. In addition to their study on HMg^+,[8] Aymar *et al.* also published results for M = Ca–Ba, using similar methodology.[12] For HCa^+, the agreement with the present CCSD(T) results is seen to be very good. An experimental result[13] from the same laboratory as reference 10 gives a binding energy of 16 700 $\pm$1000 cm^{-1}, with the present CCSD(T) result lying slightly higher than this range.

In the case of HSr^+, Abe *et al.*[9] used a slightly smaller basis set than for their previous calculations, of the ANO-RCC type, with the same level

	R_e / Å	D_e / cm^{-1}	ω_e / cm^{-1}	Reference
HBe^+	1.307	25 550	2275	Present Work
	1.310	25 740	2140	6[a]
	1.310	26 285 ±100	2222	7[b]
HMg^+	1.637	16 840	1789	Present Work
	1.65	16 376		8[c]
	1.653	16 888	1705.8	9[d]
		16 500 ±500		10[e]
	1.652	∼17 000	1699.1	11[f]
HCa^+	1.877	17 830	1558	Present Work
	1.896	18 111	1502.7	9[d]
	1.87	17 972	1453	12[c]
		16 700 ±1000		13[g]
HSr^+	2.020	17 200	1448	Present Work
	2.041	17 105	1408.8	9[d]
	1.97	18 078	1429	12[c]
		18 200 ±500		10[e]
HBa^+	2.123	20 020	1350	Present Work
	2.139	19 764	1352.7	9[d]
	2.08	21 604	1368	12[c]
		20 600 ±800		14[g]
HRa^+	2.226	16 390	1299	Present Work

[a] MR-ACPF calculations by Koput *et al.*
[b] Emission spectrum from Coxon and Collins.
[c] CIPSI calculations by Aymar *et al.*
[d] CCSD(T) calculations by Abe *et al.*
[e] Experimental result from Dalleska *et al.*
[f] Emission spectrum from Balfour.
[g] Experimental result from Armentrout *et al.*

Table 6.1: Spectroscopic constants for the HM^+ species. R_e is the equilibrium bond length, D_e is the equilibrium dissociation energy, and ω_e is the harmonic vibrational frequency.

of theory, CCSD(T). R_e obtained using this methodology is again slightly longer than the present result, but the binding energies are in excellent agreement. CIPSI results from Aymar *et al.*[12] are seen to be in somewhat poorer agreement with the present CCSD(T) results, with a shorter bond length and higher binding energy. Reference 10 provides an experimental value for D_e of 18 200 ±500 cm^{-1}, which is in fairly poor agreement with the present result.

As regards BaH^+, CCSD(T)/ANO-RCC calculations from Abe *et al.*[9] are in reasonable agreement with the present CCSD(T) results, with Abe's R_e being slightly longer and D_e being lower again. Aymar *et al*'s CIPSI results[12] are seen to give reasonable agreement for R_e but poor agreement

for D_e, again exhibiting a higher interaction energy. Finally, experimental work by Armentrout[14] focussed on the isotopologue BaD^+, but appropriate scaling of the present calculated value of ω_e allows their value for D_0 to be used to calculate a value for D_e, in this case giving 20 600 ±800 cm^{-1}. These values put the result from the present study just within the range of the experimental uncertainty.

There are no results available in the literature for HRa^+—due to the generally reasonable agreement with other results leads, the values from the calculations discussed here are likely to be reliable.

6.3.2 Trends in Spectroscopic Parameters

Trends down the HM^+ series are similar to those seen for the MH^- species in Chapter 4. R_e increases monotonically across the series with increasing size of the metal centre. The trend in D_e for the cationic series follows the same non-linear trend as for the anions, due to the similar trends in energetic cost of hybridisation. Table 6.2 collects the values for the Group 2 cation excitation energies to provide a guide as to these energetic costs, as was provided for the neutrals in Table 4.7. For Be^+ and Mg^+, the excitation to the ^2P state is lower in energy than excitation to the lowest-lying ^2D state, whereas the heavier members of the group, Ca^+—Ra^+, have a lower-lying ^2D than ^2P state. The change in excitation energy to the lower-lying state oscillates from element to element on top of a general decrease in energy with increasing atomic weight. This pattern is reflected in the relative binding energies for each complex. HBe^+ is seen to be an outlier, as although it has

	Be^+	Mg^+	Ca^+	Sr^+	Ba^+	Ra^+
$^2P \leftarrow {}^2S$ / cm^{-1}	31 929	35 669	25 192	23 715	20 262	21 351
$^2D \leftarrow {}^2S$ / cm^{-1}	98 055	71 490	13 650	14 556	4 874	12 084

Table 6.2: Energies of the lowest $^2P \leftarrow {}^2S$ and $^2D \leftarrow {}^2S$ excitations for the Group 2 metal cations taken from Reference 15.

the highest excitation energy it also shows the highest binding energy. This is discussed further below.

Excitation energies for the cationic series show a decrease from the corresponding neutrals, which is likely partially responsible for the increased binding energies compared to the MH^- species. The significant reduction in repulsion through loss of two electrons from the complex will also be a strong contributing factor to this effect, as discussed above. Furthermore, as D_e is shorter for the cationic complexes, the strength of the ion/induced-dipole interaction is increased, also raising the overall binding energy.

6.3.3 Partial Atomic Charges and Contour Plots

Results of partial atomic charge analysis are presented in Table 6.3. The two approaches employed are generally in good agreement with each other except for HBe^+, where the charge predicted by AIM is somewhat higher than that from NPA. In all cases, there is seen to be a significant amount of charge transfer, with the charge on M being >1.5 e for almost all cases.

Examination of the NBO data for these orbitals is instructive as to the breakdown of atomic orbital contributions to the HOMO, as seen in Table 6.4. Most of the orbital character comes from hydrogen orbitals, and this hydrogen contribution is shown by NBO analysis to originate overwhelmingly (>97 %) from H s-orbitals. Contributions to the HOMO from the metal are smaller but still significant, accounting for ∼10—25 % of the HOMO character. Subdivision of this contribution into orbitals of different angular momenta yields interesting differences between the different elements of Group 2. The beryllium and magnesium species show mostly s-orbital character (quite notably so for magnesium) with some contribution from p-orbitals, whereas the heavier metals in the group show much larger amounts of hybridisation occurring as significant amounts of d-orbital character become mixed in.

		HBe^+	HMg^+	HCa^+	HSr^+	HBa^+	HRa^+
NPA	Q_M	1.46	1.47	1.71	1.74	1.76	1.76
	Q_H	-0.46	-0.47	-0.71	-0.74	-0.76	-0.76
AIM	Q_M	1.72	1.53	1.65	1.66	1.64	1.67
	Q_H	-0.72	-0.53	-0.65	-0.66	-0.64	-0.67
$H(r)$		-0.050	-0.012	-0.020	-0.019	-0.022	-0.017

Table 6.3: Partial atomic charges in atomic units (e) calculated using NPA and AIM theories from QCISD/aTZ density, and the total local energy density $H(r)$ at the BCPs in atomic units (E_h $a_0{}^{-3}$).

Contour plots of the HOMO density provide a complementary analysis to this, and are seen on the left-hand side of Figure 6.1. The form of these orbitals show clear contributions from both centres, corresponding to mixed HOMO character in line with the NBO results. Density located on the metals for the beryllium and magnesium species is quite isotropic, whereas the heavier metals show density which looks like a d_{z^2} orbital, reflecting the shape of the more energetically accessible virtual d-orbitals in line with Table 6.2.

In contrast with the other members of the group, beryllium possesses no occupied p-orbitals, and so repulsive effects with the hydrogen atom will be less strongly felt. As an additional consequence, the hydrogen will be able to position itself closer to the partially-exposed beryllium core, thus increasing the strength of the ion/induced-dipole interaction. The shorter R_e will also lead to a better overlap of orbitals, increasing the strength of covalent effects. These cooperative effects are the rationale for the high binding energy of the HBe^+ species compared to the rest of the group.

Values of the total local energy density, $H(r)$, introduced in Section 2.3.3,

		HBe^+	HMg^+	HCa^+	HSr^+	HBa^+	HRa^+
Atomic	% M	26.3	25.6	14.0	12.4	11.2	11.3
Contributions	% H	73.7	74.4	86.0	87.6	88.8	88.7
Metal	% M s	91.1	98.3	69.8	63.1	28.4	54.9
Contributions	% M p	8.8	1.5	0.4	0.3	0.6	1.0
	% M d	0.1	0.2	29.6	36.4	70.0	42.7

Table 6.4: NBO data for the HOMOs for the HM^+ species.

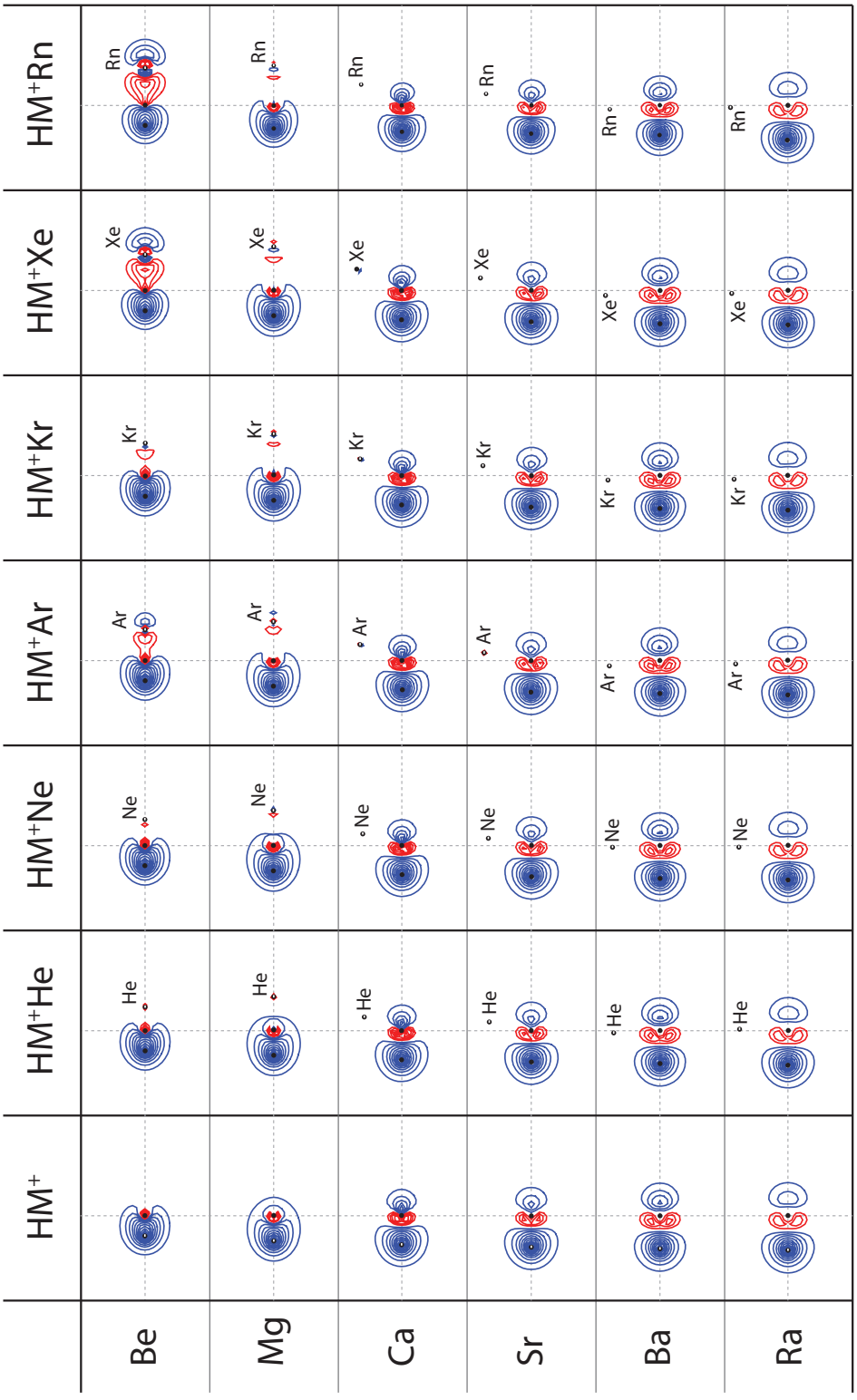


Figure 6.1: Contour plots of the HM^+ and HM^+RG complexes.

for the HM^+ species are gathered in Table 6.3. It can be seen that for all six species, the sign of $H(r)$ is negative, indicating that there is some covalent character in the bonding interaction here. HBe^+ is seen to be an outlier here also with an $H(r)$ parameter which is notably higher, at more than twice any other complex in the series, likely a consequence of increased orbital overlap for these complexes.

6.4 Interactions Between HM^+ and RG atoms

6.4.1 Geometric Parameters

Collected in Table 6.5 are the various spectroscopic constants that have been calculated for the HM^+–RG complexes. The metal-rare gas bond length, $R_{\text{M–RG}}$, is seen to increase monotonically with increasing size of rare gas atom, and also with increasing size of metal.

Inspection of the metal-hydrogen bond length, $R_{\text{M–H}}$, shows overall consistency between the isolated HM^+ unit and its corresponding HM^+–RG complexes. Deviations from this are extremely subtle yet interesting, as there is seen to be a near-universal increase in this bond length for a specific HM^+ unit with increasing atomic number of rare gas. Curiously, the $R_{\text{M–H}}$ length for all HBe^+–RG complexes is very slightly shorter than for the isolated HBe^+ species—although this subtle effect is true for the lighter HM^+–RG complexes compared to the corresponding HM^+ diatomic, the beryllium complexes are unique in that this is true for all rare gases.

For the H—M—RG bond angle, θ, whether each complex adopts a bent or linear global energetic minimum geometry is dependent on the metal involved. Each of the beryllium and magnesium complexes are found to be linear, whilst the heavier metals Ca—Ra show bent minima. This division corresponds to the patterns of hybridisation discussed earlier and outlined

	R_{M-H} / Å	R_{M-RG} / Å	θ / °	ν_1 / cm^{-1}	ν_2[a] / cm^{-1}	ν_3 / cm^{-1}	k_1[b] / Nm^{-1}
HBe^+	1.307					2275	
HBe^+–He	1.299	1.523	180.0	612	235	2341	63.1
HBe^+–Ne	1.299	1.671	180.0	474	245	2339	88.4
HBe^+–Ar	1.300	1.979	180.0	488	327	2308	112.4
HBe^+–Kr	1.301	2.115	180.0	466	312	2331	114.5
HBe^+–Xe	1.302	2.301	180.0	451	330	2324	111.6
HBe^+–Rn	1.303	2.385	180.0	436	334	2317	107.4
HMg^+	1.637					1789	
HMg^+–He	1.635	2.132	180.0	233	84	1807	11.0
HMg^+–Ne	1.635	2.232	180.0	177	90	1808	20.5
HMg^+–Ar	1.636	2.497	180.0	213	121	1811	41.1
HMg^+–Kr	1.638	2.618	180.0	200	135	1808	45.4
HMg^+–Xe	1.640	2.791	180.0	199	157	1802	49.0
HMg^+–Rn	1.641	2.865	180.0	194	161	1799	49.8
HCa^+	1.877					1558	
HCa^+–He	1.876	2.553	110.0	160	95	1568	5.5
HCa^+–Ne	1.878	2.616	107.0	131	101	1563	13.6
HCa^+–Ar	1.882	2.882	111.4	156	116	1555	29.0
HCa^+–Kr	1.885	3.001	111.9	150	106	1551	36.5
HCa^+–Xe	1.889	3.187	115.7	148	103	1543	40.3
HCa^+–Rn	1.891	3.261	117.5	146	100	1539	43.4
HSr^+	2.020					1448	
HSr^+–He	2.020	2.757	101.7	138	82	1467	4.3
HSr^+–Ne	2.022	2.812	99.4	109	87	1462	11.4
HSr^+–Ar	2.025	3.052	99.3	132	98	1457	28.3
HSr^+–Kr	2.028	3.184	101.0	131	84	1452	43.6
HSr^+–Xe	2.032	3.365	103.3	132	78	1447	54.5
HSr^+–Rn	2.031	3.431	103.2	134	73	1442	67.2
HBa^+	2.123					1350	
HBa^+–He	2.124	2.988	86.9	122	55	1391	3.4
HBa^+–Ne	2.125	3.056	87.9	82	67	1390	6.9
HBa^+–Ar	2.127	3.255	84.2	120	85	1381	26.3
HBa^+–Kr	2.131	3.359	84.6	115	70	1378	40.8
HBa^+–Xe	2.135	3.526	84.6	118	64	1373	55.5
HBa^+–Rn	2.135	3.590	84.5	118	58	1369	70.1
HRa^+	2.226					1299	
HRa^+–He	2.226	3.139	90.5	104	57	1349	2.5
HRa^+–Ne	2.227	3.165	87.7	80	66	1348	6.9
HRa^+–Ar	2.230	3.357	86.1	110	77	1342	24.2
HRa^+–Kr	2.231	3.461	86.1	113	62	1339	46.1
HRa^+–Xe	2.233	3.631	86.9	114	56	1335	63.9
HRa^+–Rn	2.235	3.693	86.9	117	50	1331	90.5

[a] ν_2 is doubly degenerate for the linear HBe^+–RG and HMg^+–RG species
[b] Force constant calculated using a pseudo-diatomic (HM$\cdots$RG) model

Table 6.5: Spectroscopic constants for the HM^+–RG species.

in Table 6.4; the bent geometries accompany inclusion of d-orbital character in the HOMO, whereas those metals which undergo sp or essentially no hybridisation produce linear complexes. This point will be revisited later in this chapter.

6.4.2 Harmonic Vibrational Frequencies

Values of the harmonic vibrational frequencies calculated using analytical gradients are also collected in Table 6.5. All of the frequencies show a general decrease in wavenumber as Group 2 is descended, due chiefly to the mass effect. As the rare gas is changed however, more nuanced trends are seen.

ν_1, the van der Waals HM$\cdots$RG stretch, shows a general decrease down Group 18 for the Be—Ca series, although the frequency for each HM^+Ne complex is notably lower than would be expected from this trend. The difference in wavenumber between the He and Rn complex for each series decreases from Be to Ca such that for the heavier three metals Sr—Ra, there is very little difference in ν_1 upon substitution of rare gas atom. Again, however, the corresponding Ne complexes are much lower in wavenumber than the rest of the series.

To remove the mass dependency from ν_1, force constants, k_1, from Hooke's law have been calculated according to a pseudo-diatomic HM$\cdots$RG model. Examination of the nuclear displacements from the frequency calculations shows that there is a slight mixing between the intramolecular H$\cdots$M stretch and the van der Waals HM$\cdots$RG stretch, but the extent of this is very slight and is not expected to perturb the energy of either vibration significantly, validating this pseudo-diatomic approach. Comparison of the force constants show a monotonic increase for the heavier metal series as Group 18 is descended. For the HBe^+–RG series, k_1 essentially plateaus for RG = Ar—Rn, with only a slight decrease seen over this range. The HMg^+–RG series behaves similarly to the beryllium complexes, although the essential plateauing for RG = Ar—Rn now demonstrates a slight increase throughout, moving towards the monotonic increase seen for the heavier rare gases.

The bending mode, ν_2, shows a straightforward monotonic increase for the Be and Mg series (in these linear cases, this mode is also doubly degenerate). For the heavier metal series, Ca—Ra, the trend is no longer monotonic, and instead shows an increase from HM^+–He to HM^+–Ar, and a decrease from there to HM^+–Rn.

Similar to the above trend in $R_{\mathrm{M–H}}$ is the behaviour of the M$\cdots$H stretching frequency, ν_3. The value for each HM^+ unit remains largely consistent for each of the rare gases, with each individual metal series exhibiting a maximum difference for ν_3 of no more than 2 %. There is, in general, a slight decrease in this frequency throughout Group 18 for each HM^+ series, which is attributed to the mixing of a small amount of HM$\cdots$RG stretch character being mixed in, as deduced from the calculated displacements, and the reduced mass effect responsible for the slight lowering in energy with increasing mass of rare gas. As discussed above in the context of ν_1 however, this effect is not particularly significant, with the consistency of ν_3 supporting this.

6.4.3 Contour Plots

Inspection of the contour plots in Figure 6.1 shows that the form of the HOMO remains essentially consistent for each HM^+ unit with each different rare gas, with only minimal orbital density located on the rare gas atom. A few notable exceptions are seen for the heavier HBe^+–RG complexes for RG = Ar—Rn, although even in these cases the density localised to the HM^+ unit is essentially the same as for the isolated diatomic, with the RG contributions seen to be 'extra' and not to affect the HM^+ density significantly.

These contour plots also give an interesting perspective on the linear vs. bent geometries. The HOMOs of HBe^+ and HMg^+ show considerable

orbital density located around the hydrogen atom. Consequently, in order to be closer to the metal center and increase the strength of the ion/induced-dipole force, the rare gas atoms approach the metal on the side opposite the hydrogen atom, avoiding repulsive effects with the HM^+ HOMO density.

For HCa^+—HRa^+, sd-hybridisation occurs (as shown from the NBO results in Table 6.4) such that the phase of the s-orbital and the lobes of the d_{z^2}-orbital match. This results in a build-up of electron density along the HM^+ internuclear axis and concurrent depletion of density off-axis resulting from destructive inteference between the torus of the d_{z^2}-orbital and the s-orbital density. Consequently, the RG atom approaches along the curved nodal planes resulting from cancellation of s-orbital and d_{z^2}-orbital density, rather than linearly along the HM^+ internuclear axis. Again, this minimises repulsion effects whilst giving the closest approach to the metal centre for the rare gas atom and thus increasing the strength of the ion/induced-dipole interaction.

Contour plots of the HOMO density for the heavier HBe^+–RG complexes are especially revealing. Notable contributions are seen from the rare gas for RG = Ar—Rn, in stark contrast to the other HM^+–RG complexes. This strong delocalisation of orbital density over both the HM^+ unit and the rare gas atom is possibly indicative of some covalent character being present in the interactions.

6.4.4 Dissociation Energies

Collected in Table 6.6 are the equilibrium dissociation energies, D_e, calculated using CCSD(T) theory at the MP2 optimised geometries. These calculations were conducted using both quadruple- and quintuple-ζ quality basis sets both with and without application of full counterpoise correction in order to assess the basis set dependence and BSSE of the binding energies

for these complexes.

BSSE was found to be fairly significant when quadruple-ζ basis sets were used. The extent of this error is largest for the HM^+–Ne complexes, and reaches almost 10 % of the total binding energy for the barium and radium complexes. Use of quintuple-ζ basis sets reduces this error to less than 4 % for all complexes. Additionally, although the results from using quintuple-ζ basis sets would be expected to show an increase in binding energy, there is no systematic increase or decrease upon increasing the quality of basis set

	aQZ	aQZ + CP	a5Z	a5Z + CP	EBS + CP
HBe^+–He	2 958	2 941	2 958	2 951	2 961
HBe^+–Ne	4 610	4 487	4 552	4 513	4 540
HBe^+–Ar	9 913	9 797	9 894	9 833	9 870
HBe^+–Kr	11 692	11 559	11 641	11 581	11 603
HBe^+–Xe	14 110	13 905	14 007	13 917	13 929
HBe^+–Rn	15 248	15 026	15 122	15 021	15 015
HMg^+–He	686	667	683	672	678
HMg^+–Ne	1 377	1 284	1 345	1 313	1 342
HMg^+–Ar	3 817	3 740	3 816	3 767	3 795
HMg^+–Kr	4 839	4 756	4 838	4 785	4 817
HMg^+–Xe	6 272	6 154	6 258	6 187	6 222
HMg^+–Rn	7 039	6 912	7 011	6 937	6 964
HCa^+–He	394	378	399	390	403
HCa^+–Ne	809	749	813	791	835
HCa^+–Ar	2 152	2 101	2 175	2 145	2 191
HCa^+–Kr	2 721	2 671	2 746	2 719	2 770
HCa^+–Xe	3 490	3 426	3 522	3 489	3 555
HCa^+–Rn	3 917	3 853	3 951	3 916	3 983
HSr^+–He	321	307	325	317	328
HSr^+–Ne	667	613	665	645	679
HSr^+–Ar	1 767	1 716	1 788	1 759	1 804
HSr^+–Kr	2 242	2 194	2 262	2 238	2 284
HSr^+–Xe	2 870	2 812	2 901	2 871	2 934
HSr^+–Rn	3 218	3 161	3 255	3 225	3 291
HBa^+–He	276	260	274	267	274
HBa^+–Ne	535	488	523	507	527
HBa^+–Ar	1 431	1 377	1 442	1 416	1 456
HBa^+–Kr	1 832	1 777	1 839	1 816	1 856
HBa^+–Xe	2 360	2 292	2 371	2 345	2 400
HBa^+–Rn	2 651	2 586	2 669	2 642	2 700
HRa^+–He	224	210	224	218	226
HRa^+–Ne	472	428	465	449	470
HRa^+–Ar	1 304	1 250	1 321	1 294	1 341
HRa^+–Kr	1 683	1 627	1 696	1 673	1 721
HRa^+–Xe	2 176	2 110	2 198	2 171	2 236
HRa^+–Rn	2 461	2 395	2 487	2 461	2 529

Table 6.6: Equilibrium dissociation energies (/ cm^{-1}) for the HM^+–RG complexes both with (+ CP) and without full counterpoise correction using quadruple- and quintuple-ζ basis sets, and extrapolating to the basis set limit (EBS).

when the non-CP corrected values are considered. This is corrected upon counterpoise correction, and the quintuple-ζ results are now more strongly bound in all cases (although HBe^+–Rn does not obey this trend even with counterpoise correction, the difference between the binding energies using different basis sets is an insignificant percentage, and is likely within the accuracy of the calculations).

Using the two sets of counterpoise corrected values, it is possible to extrapolate the D_e values to the basis set limit, EBS + CP. These values are to be considered the 'best' results, and so it is this set of dissociation energies that will be considered henceforth.

Binding energies for these complexes are found to be rather high for rare gas interactions. This is most notable for the beryllium series, which features a binding energy for HBe^+–Rn of over 15 000 cm^{-1}. In general, there is seen to be a decrease for a particular rare gas with increasing atomic number of metal, attributable to increasing repulsion effects from the larger metal centres. Conversely, for a specific metal series, larger rare gas atoms give higher dissociation energies, primarily attributable to the polarisability of the rare gas atom increasing. For M = Mg—Ra, the increase in D_e through the series is about an order of magnitude, but for M = Be the difference between HBe^+–He and HBe^+–Rn is roughly a factor of 5. In combination with the binding energies for the beryllium complexes being markedly higher than for the other metal series, this would seem to indicate that the character of the interaction between the rare gas atoms and the HBe^+ unit are differentiable from the other metal series.

6.4.5 Partial Atomic Charges

Partial atomic charges have been calculated with both AIM and NPA methodologies for the HM^+–RG complexes, the results of which are shown

in Table 6.7. As was seen for the partial atomic charges for the HM^+ diatomics, the two methodologies yield results which are generally in reasonable agreement for the heavier metals Ca—Ra. Agreement for the magnesium-containing complexes is also seen to be fair, although for the heavier rare gas complexes, NPA predicts a charge of up to 0.14 e on the rare gas. Charges on rare gas atoms for the HBe^+–RG series are predicted by NPA analysis to be even higher, with up to 0.29 e seen in the case of HBe^+–Rn. The

			HM^+	HM^+–He	HM^+–Ne	HM^+–Ar	HM^+–Kr	HM^+–Xe	HM^+–Rn
HBe^+–RG	NPA	Q_H	-0.46	-0.49	-0.50	-0.50	-0.50	-0.51	-0.52
		Q_{Be}	1.46	1.43	1.44	1.35	1.31	1.25	1.22
		Q_{RG}	—	0.06	0.06	0.15	0.19	0.26	0.29
	AIM	Q_H	-0.72	-0.76	-0.76	-0.78	-0.78	-0.79	-0.79
		Q_{Be}	1.72	1.75	1.75	1.74	1.73	1.72	1.71
		Q_{RG}	—	0.01	0.01	0.04	0.05	0.07	0.08
HMg^+–RG	NPA	Q_H	-0.47	-0.50	-0.51	-0.53	-0.54	-0.55	-0.55
		Q_{Mg}	1.47	1.49	1.49	1.47	1.45	1.43	1.41
		Q_{RG}	—	0.02	0.02	0.06	0.08	0.12	0.14
	AIM	Q_H	-0.53	-0.56	-0.57	-0.60	-0.61	-0.62	-0.63
		Q_{Mg}	1.53	1.56	1.57	1.58	1.58	1.57	1.57
		Q_{RG}	—	0.00	0.00	0.02	0.03	0.05	0.06
HCa^+–RG	NPA	Q_H	-0.71	-0.71	-0.71	-0.71	-0.72	-0.72	-0.72
		Q_{Ca}	1.71	1.71	1.70	1.69	1.68	1.66	1.66
		Q_{RG}	—	0.01	0.01	0.03	0.04	0.05	0.06
	AIM	Q_H	-0.65	-0.66	-0.66	-0.67	-0.67	-0.68	-0.68
		Q_{Ca}	1.65	1.65	1.65	1.65	1.64	1.63	1.63
		Q_{RG}	—	0.00	0.00	0.02	0.03	0.04	0.05
HSr^+–RG	NPA	Q_H	-0.71	-0.74	-0.74	-0.74	-0.74	-0.74	-0.74
		Q_{Sr}	1.71	1.74	1.73	1.72	1.71	1.70	1.69
		Q_{RG}	—	0.00	0.01	0.02	0.03	0.04	0.05
	AIM	Q_H	-0.66	-0.67	-0.67	-0.67	-0.68	-0.68	-0.68
		Q_{Sr}	1.66	1.67	1.67	1.66	1.65	1.64	1.64
		Q_{RG}	—	0.00	0.00	0.02	0.03	0.04	0.05
HBa^+–RG	NPA	Q_H	-0.76	-0.76	-0.76	-0.76	-0.76	-0.76	-0.76
		Q_{Ba}	1.76	1.76	1.76	1.75	1.74	1.73	1.72
		Q_{RG}	—	0.00	0.00	0.01	0.02	0.03	0.04
	AIM	Q_H	-0.64	-0.65	-0.65	-0.65	-0.65	-0.65	-0.65
		Q_{Ba}	1.64	1.64	1.65	1.63	1.62	1.61	1.60
		Q_{RG}	—	0.00	0.00	0.02	0.02	0.04	0.05
HRa^+–RG	NPA	Q_H	-0.76	-0.76	-0.76	-0.76	-0.76	-0.76	-0.76
		Q_{Ra}	1.76	1.76	1.76	1.74	1.74	1.73	1.72
		Q_{RG}	—	0.00	0.00	0.01	0.02	0.03	0.04
	AIM	Q_H	-0.67	-0.68	-0.67	-0.68	-0.68	-0.68	-0.68
		Q_{Ra}	1.67	1.68	1.68	1.67	1.66	1.65	1.64
		Q_{RG}	—	0.00	0.00	0.01	0.02	0.03	0.04

Table 6.7: Partial atomic charges for the HM^+–RG series calculated using NPA and AIM theories from QCISD/aTZ density.

charge assigned to the rare gas atom is low for all complexes with AIM methodology, with <0.1 e found in all cases. Heavier rare gas atoms carry a slightly larger partial charge than the lighter ones, in line with the increasing polarisability down Group 18. As was discussed in Chapter 5, it seems that Group 2 complexes can be difficult to describe using partial atomic charge analysis.

Comparing the charges found on the metal and hydrogen atoms in the diatomic species to the corresponding triatomics shows remarkable consistency for M = Ca—Ra, a conclusion which agrees well with the consistency in $R_{\mathrm{M—H}}$ and ν_3. For M = Be and Mg, however, there is an increase in charge transferred from the metal to the hydrogen atom, which is seem to increase along with atomic number of rare gas atom. An explanation for this is that the heavier four metals, which exhibit sd-hybridisation, are able to move incoming electron density from the rare gas atom into off-axis d-orbital character, and so in these cases the movement of charge does not involve the hydrogen atom. Since magnesium undergoes essentially no hybridisation and beryllium has undergone slight sp-hybridisation, the small amount of electron density transferred from the rare gas to the metal is partially shifted to the hydrogen atom in order to reduce repulsion in the M—RG internuclear region.

The total local energy density, $H(r)$, also from AIM analysis, has been calculated, the results of which are collected in Table 6.8. These values show remarkable consistency in the value of $H(r)$ at the H—M bond critical point throughout each metal series, including for the diatomic species. Once again, the beryllium series is seen to be in defiance of this trend, as the value of $H(r)$ is slightly lower for the uncomplexed HBe^+ unit.

Turning attention now to the M—RG bonding critical point, almost all HM^+–RG complexes show $H(r)>0$, which indicates that the electronic

M	BCP	HM^+	HM^+–He	HM^+–Ne	HM^+–Ar	HM^+–Kr	HM^+–Xe	HM^+–Rn
Be	M—H	-0.049	-0.056	-0.055	-0.056	-0.056	-0.056	-0.055
	M—RG		0.012	0.017	-0.003	-0.009	-0.014	-0.016
Mg	M—H	-0.012	-0.012	-0.012	-0.012	-0.012	-0.012	-0.012
	M—RG		0.005	0.006	0.004	0.002	0.000	-0.001
Ca	M—H	-0.020	-0.020	-0.020	-0.020	-0.019	-0.019	-0.018
	M—RG		0.003	0.004	0.003	0.002	0.001	0.001
Sr	M—H	-0.019	-0.019	-0.019	-0.018	-0.018	-0.018	-0.017
	M—RG		0.003	0.003	0.003	0.002	0.001	0.001
Ba	M—H	-0.022	-0.022	-0.022	-0.022	-0.022	-0.021	-0.021
	M—RG		0.002	0.002	0.002	0.001	0.001	0.000
Ra	M—H	-0.017	-0.017	-0.017	-0.017	-0.017	-0.017	-0.017
	M—RG		0.002	0.001	0.002	0.001	0.001	0.000

Table 6.8: Total local energy densities $H(r)$ at the bond critical points BCP in the HM^+ HM^+–RG complexes. Values of less than zero indicate partial covalent character.

interaction at the critical point between the metal and rare gas is destabilising, with no covalent contribution. However, HBe^+–Ar, HBe^+–Kr, HBe^+–Xe, and HBe^+–Rn, as well as HMg^+–Rn, all have a value of $H(r)$ which is less than zero, indicating that there is partial covalent character in the interaction. Previously discussed peculiarities of the beryllium series also concur with this conclusion, notably the contour plots.

6.4.6 Charge Induced Dipole Interactions

Attempting to fit the triatomic HM^+–RG complexes to an ion/induced-dipole model yields a slight complication as both atoms in the HM^+ unit are charged, as illustrated by the partial atomic charge analysis in Table 6.7. Consequently, even when considering only polarisation of the rare gas atom, there are two dipoles being imposed, and so in order to give a proper treatment of this situation both contributions must be assessed.

First, the expression for the two dipoles are as follows:

$$\mu_{\mathrm{M}} = \frac{q_{\mathrm{M}} \cdot \alpha}{{R_{\mathrm{M}}}^2} \qquad\qquad \mu_{\mathrm{H}} = \frac{q_{\mathrm{H}} \cdot \alpha}{{R_{\mathrm{H}}}^2} \tag{6.1}$$

where μ_{X} is the dipole imposed by atom X, q_{X} is the charge on atom X, α is

the rare gas polarisability, and R_{X} is the distance to atom X from RG. The two opposing dipoles being created can be considered as the dipole created by one atom plus the parallel component of the dipole created by the other atom, as such:

$$\mu^{tot}{}_{\mathrm{M}} = \mu_{\mathrm{M}} + \mu_{\mathrm{H}} \cdot cos\chi \qquad\qquad \mu^{tot}{}_{\mathrm{H}} = \mu_{\mathrm{H}} + \mu_{\mathrm{M}} \cdot cos\chi \tag{6.2}$$

where χ is the M—RG—H bond angle. The charge/induced-dipole interactions take the following form:

$$V_{\mathrm{M}} = -\frac{1}{2}\frac{\mu^{tot}{}_{\mathrm{M}} \cdot q_{\mathrm{M}}}{{R_{\mathrm{M}}}^2} \qquad\qquad V_{\mathrm{H}} = -\frac{1}{2}\frac{\mu^{tot}{}_{\mathrm{H}} \cdot q_{\mathrm{H}}}{{R_{\mathrm{H}}}^2} \tag{6.3}$$

Since the total charge induced dipole interaction, V_{tot}, is the sum of V_{M} and V_{H}, the above equations can be combined and rearranged to give the following expression:

$$V_{\mathrm{tot}} = -\frac{\alpha}{2}\left[\frac{{q_{\mathrm{M}}}^2}{{R_{\mathrm{M}}}^4} + \frac{{q_{\mathrm{H}}}^2}{{R_{\mathrm{H}}}^4} + 2\frac{q_{\mathrm{M}} \cdot q_{\mathrm{H}}}{{R_{\mathrm{M}}}^2 \cdot {R_{\mathrm{H}}}^2} cos\chi\right] \tag{6.4}$$

For the linear case, $cos\chi = 1$, and so the expression simplifies to the following:

$$V_{\mathrm{tot}} = -\frac{\alpha}{2}\left[\frac{q_{\mathrm{M}}}{{R_{\mathrm{M}}}^2} + \frac{q_{\mathrm{H}}}{{R_{\mathrm{H}}}^2}\right]^2 \tag{6.5}$$

This model simplifies the problem somewhat, as it ignores the effects of higher order terms, damping terms, and many body effects. These omissions however are justifiable; firstly, as the bond lengths involved are reasonably long, damping terms should not be a significant correction. Additionally, the small hydrogen centre and close to doubly-charged metal centre will not

be particularly polarisable, so higher order attractive terms will likely be unimportant. Consequently, the model should quite adequately serve its purpose.

There also arises the question of what charges to use in the model. Using the integer formal charges is an oversimplification, as it completely neglects any of the effects of charge transfer. Much better would be the application of partial atomic charges as calculated from either AIM or NPA methodologies. As mentioned above, the charges from AIM theory seem to give the more reasonable results in the cases where the methodologies differ, and so these are the charges employed moving forwards.

Interaction terms arising from this analysis are collated in Table 6.9. As expected, owing to the greater charges and shorter seperations, the interaction between rare gas and metal outweighs the interaction with the hydrogen. Ratios of the sum of the charge/induced-dipole terms and the binding energy, $V_{\mathrm{tot}}/D_{\mathrm{e}}$, have been determined to assess the importance of this induction term in the total interaction energy. These ratios are greater than one for several of the smaller complexes, notably for the beryllium series and many of the magnesium complexes, with the implication being that repulsion terms are important for these species—this is not surprising, as it is also these complexes that exhibit the shortest values for $R_{\mathrm{M—RG}}$. For the remainder of the HM^{+}–RG complexes, the ratios are close to unity. In these cases, it would seem that the ion/induced-dipole terms are crucial to the overall strength of the interaction. Obviously this model, as mentioned above, neglects many different effects, but it would appear from this analysis that these effects are either very small, that the positive and negative contributions approximately cancel out, or both.

	V_{M}	V_{H}	V_{tot}	$V_{\mathrm{tot}}/D_{\mathrm{e}}$
HBe^+–He	5 929	-740	5 189	1.75
HBe^+–Ne	7 791	-1 071	6 720	1.48
HBe^+–Ar	15 729	-2 568	13 160	1.33
HBe^+–Kr	17 818	-3 080	14 738	1.27
HBe^+–Xe	20 121	-3 769	16 351	1.17
HBe^+–Rn	21 608	-4 175	17 433	1.16
HMg^+–He	1 241	-143	1 098	1.62
HMg^+–Ne	2 008	-243	1 765	1.32
HMg^+–Ar	5 268	-730	4 538	1.20
HMg^+–Kr	6 535	-955	5 580	1.16
HMg^+–Xe	8 037	-1 259	6 778	1.09
HMg^+–Rn	9 083	-1 474	7 610	1.09
HCa^+–He	634	-100	534	1.33
HCa^+–Ne	1 153	-200	952	1.14
HCa^+–Ar	3 159	-590	2 569	1.17
HCa^+–Kr	3 896	-715	3 181	1.15
HCa^+–Xe	4 928	-1 001	3 927	1.10
HCa^+–Rn	5 520	-1 094	4 426	1.11
HSr^+–He	468	-79	389	1.19
HSr^+–Ne	819	-144	675	0.99
HSr^+–Ar	2 388	-456	1 932	1.07
HSr^+–Kr	2 982	-595	2 387	1.05
HSr^+–Xe	3 814	-791	3 023	1.03
HSr^+–Rn	4 437	-936	3 501	1.06
HBa^+–He	313	-58	255	0.93
HBa^+–Ne	557	-106	451	0.86
HBa^+–Ar	1 683	-356	1 327	0.91
HBa^+–Kr	2 203	-480	1 723	0.93
HBa^+–Xe	2 872	-659	2 213	0.92
HBa^+–Rn	3 575	-824	2 750	1.02
HRa^+–He	270	-51	220	0.96
HRa^+–Ne	502	-96	407	0.87
HRa^+–Ar	1 573	-328	1 245	0.93
HRa^+–Kr	2 057	-445	1 612	0.94
HRa^+–Xe	2 701	-612	2 090	0.93
HRa^+–Rn	3 128	-723	2 401	0.95

Table 6.9: Ion/induced-dipole interaction terms (/ cm^{-1}) for the HM^+–RG complexes, and the ratio with the equilibrium dissociation energy.

6.5 Comparison to M^+–RG and M^{2+}–RG

Interactions between the HM^+ unit and RG atoms have been shown to be largely physical in nature, with the RG interacting directly with the metal centre. Consequently, this draws a natural comparison with the Group 2 M^+–RG and M^{2+}–RG complexes, which have been shown previously to interact in a chiefly physical manner.[16–18] Plots of $R_{\mathrm{M–RG}}$ and D_{e} for the three series are shown in Figures 6.2–6.5. Since the charge on the metal in

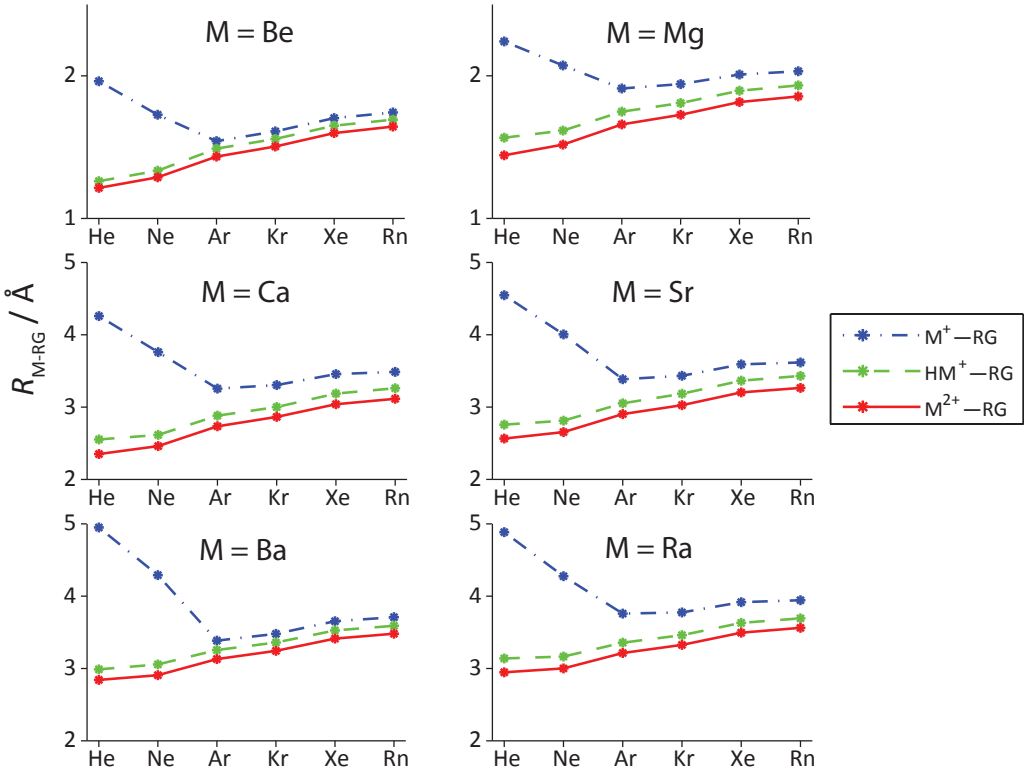


Figure 6.2: Trends in equilibrium internuclear separation between metal and rare gas for the M^+–RG, HM^+–RG, and M^{2+}–RG series. Each plot corresponds to a specific metal series with each rare gas.

the HM^+–RG complexes is ∼1.5 e, it would be expected that the values for these complexes would fall between those of the analogous diatomics. The figures indicate that this is indeed true for all complexes studied here.

Figure 6.2 shows trends in $R_{\text{M–RG}}$ for the three series, with one plot for each metal with the different rare gases. Strikingly, the behaviour of the HM^+–RG species follow very closely that of the dicationic complexes in that there is a monotonic increase in $R_{\text{M–RG}}$ with increasing size of rare gas atom. Conversely, a non-monotonic trend is evident for the M^+–RG complexes as the rare gas is varied, with each series exhibiting an intial decrease from He to a minimum at Ar, and then an increase to Rn.

Figure 6.3 shows trends in $R_{\text{M–RG}}$ for each rare gas series with the different metals. Again, the trend in the values for the HM^+–RG complexes follows the M^{2+}–RG complexes quite closely in a monotonic increase throughout

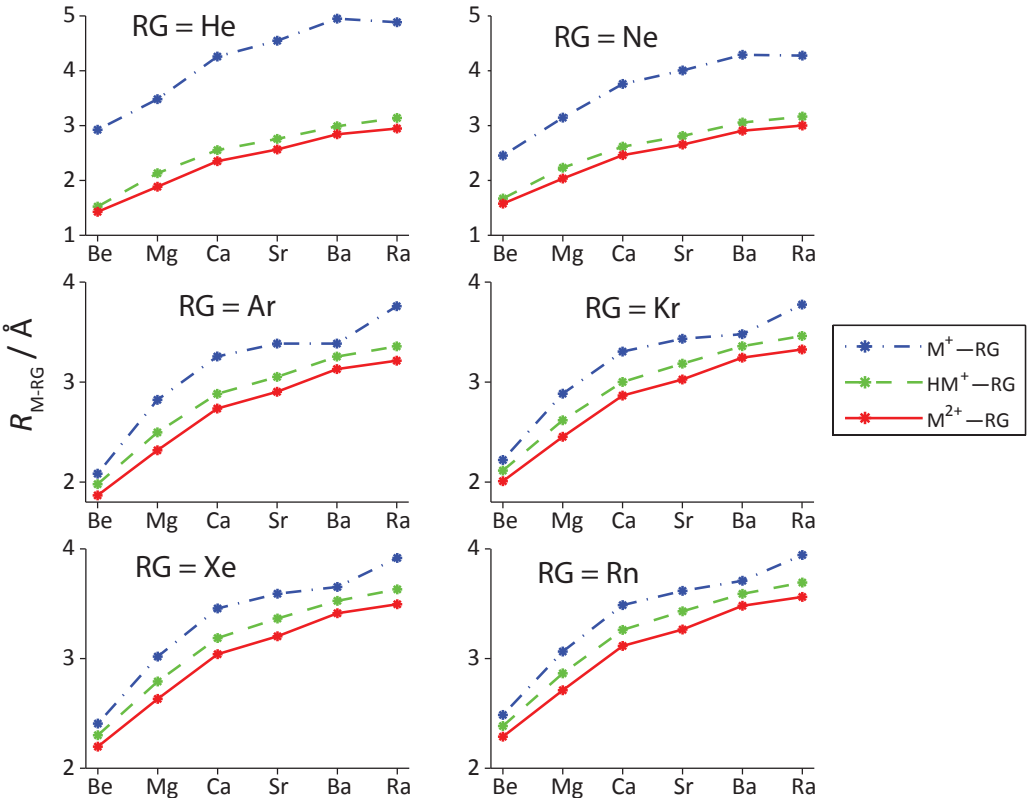


Figure 6.3: Trends in equilibrium internuclear separation between metal and rare gas for the M^+–RG, HM^+–RG, and M^{2+}–RG series. Each plot corresponds to a specific rare gas series with each metal.

each series, whereas the M^+–RG series display more nuanced trends. In previous publications, the more complicated trends for the M^+–RG complexes were attributed to subtle balances between attractive and repulsive terms. The more strongly-bound HM^+–RG and M^{2+}–RG complexes display more straightforward monotonic trends, and it is likely that this is due to the stronger ion/induced-dipole terms, arising from higher charges and shorter bond lengths, overriding the more subtle variations in the dispersive and repulsive terms.

Figure 6.4 shows the variation in D_e for each metal series with the different rare gases. Again, the values for the HM^+–RG series fall between the values for the corresponding M^+–RG and M^{2+}–RG series, although unlike for R_e, the values fall closer to those of the M^+–RG complexes. All three series of complexes show a monotonic increase as the rare gas atom is

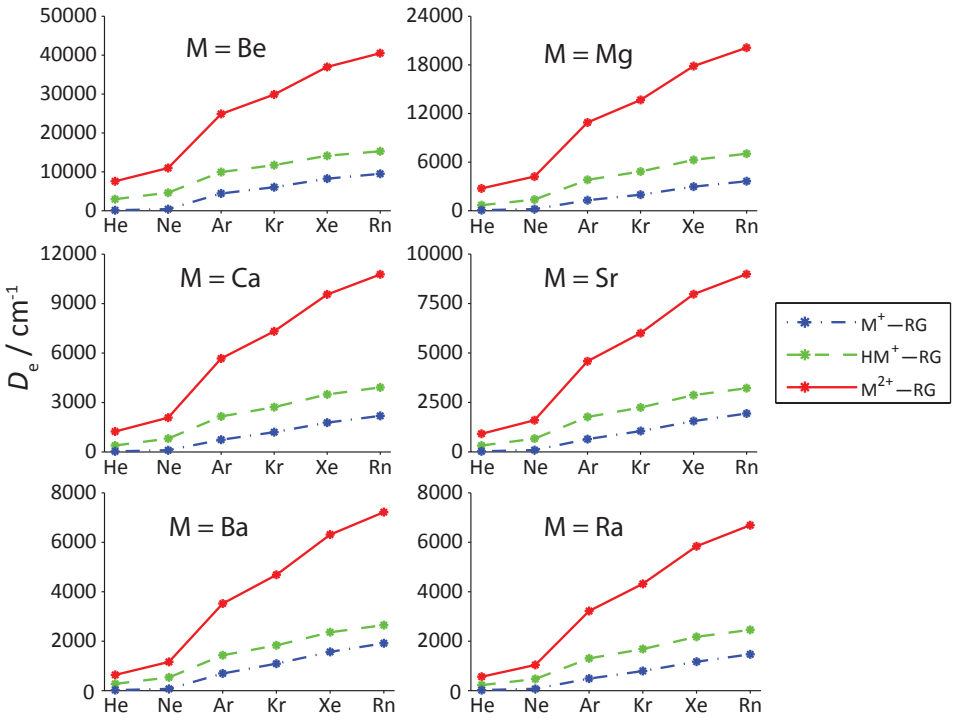


Figure 6.4: Trends in equilibrium dissociation energy between metal and rare gas for the M^+–RG, HM^+–RG, and M^{2+}–RG series. Each plot corresponds to a specific metal series with each rare gas.

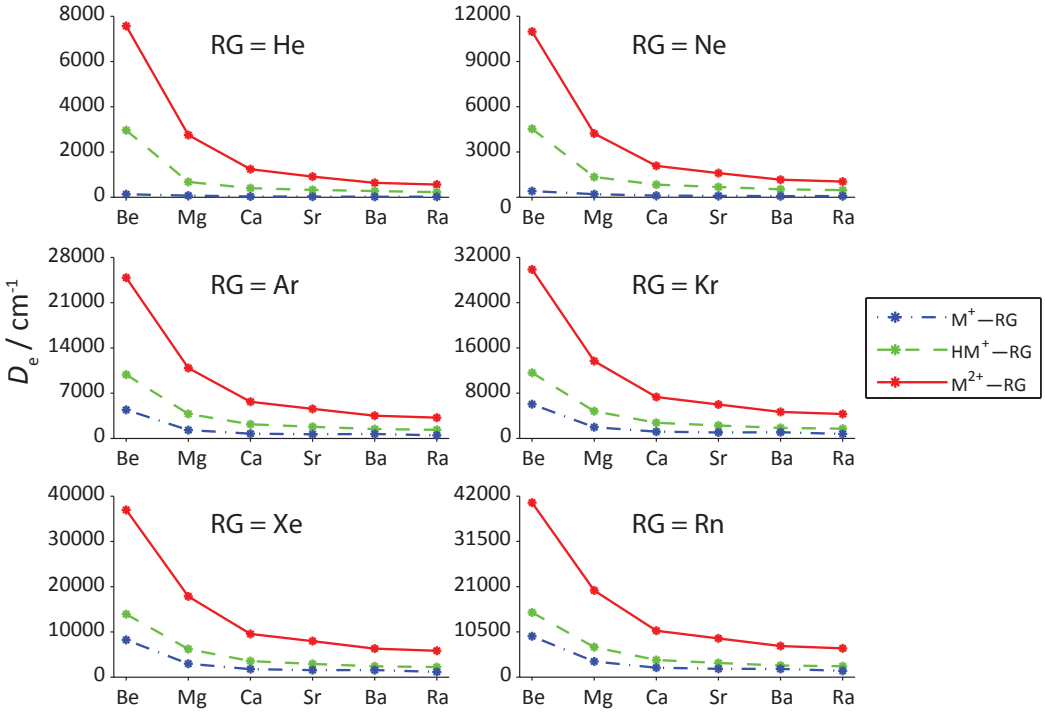


Figure 6.5: Trends in equilibrium dissociation energy between metal and rare gas for the M^+–RG, HM^+–RG, and M^{2+}–RG series. Each plot corresponds to a specific rare gas series with each metal.

varied.

Trends in D_e for a specific rare gas with the various metals are plotted in Figure 6.5. A general decrease through each rare gas series is seen—for the HM^+–RG and M^+–RG series this trend is not monotonic, although the non-monoticity is very subtle, and hardly noticeable when the values are plotted on the same scale as the M^{2+}–RG complexes.

More systematically, Table 6.10 shows ratios between values of D_e for related complexes. D_e^{R1+} is equal to the D_e for HM^+–RG divided by the value for M^+–RG, and D_e^{R2+} is equal to the value for M^{2+}–RG divided by that of HM^+–RG.

Values of D_e^{R1+} show quite considerable variation in values, demonstrating the different trends in the HM^+–RG which are less apparent from the plots owing to the very low binding energies of the M^+–RG series. Examination of the values for D_e^{R2+} show significantly more stability—evident from this is that the trends in the HM^+–RG and M^{2+}–RG series are highly similar, implying that the overall form of interaction is similar. Differences between the latter two series and the M^+–RG series, as mentioned above, likely arise from the increased charges on the metals and shorter bond lengths

M	BCP	HM^+–He	HM^+–Ne	HM^+–Ar	HM^+–Kr	HM^+–Xe	HM^+–Rn
Be	D_e^{R1+}	22.25	11.15	2.23	1.92	1.69	1.58
	D_e^{R2+}	2.56	2.42	2.52	2.57	2.65	2.70
Mg	D_e^{R1+}	9.26	6.61	2.92	2.44	2.09	1.91
	D_e^{R2+}	4.06	3.15	2.87	2.84	2.87	2.89
Ca	D_e^{R1+}	11.23	7.66	2.95	2.31	2.00	1.82
	D_e^{R2+}	3.08	2.49	2.59	2.64	2.69	2.70
Sr	D_e^{R1+}	11.35	7.44	2.79	2.18	1.88	1.70
	D_e^{R2+}	2.79	2.36	2.54	2.63	2.72	2.73
Ba	D_e^{R1+}	12.57	7.26	2.10	1.70	1.53	1.41
	D_e^{R2+}	2.33	2.21	2.42	2.52	2.63	2.67
Ra	D_e^{R1+}	9.70	6.14	2.76	2.17	1.91	1.72
	D_e^{R2+}	2.49	2.21	2.40	2.51	2.61	2.65

Table 6.10: Ratios of the dissociation energies for the M^+–RG, HM^+–RG, and M^{2+}–RG series. D_e^{R1+} is equal to $D_e(\frac{HM^+-RG}{M^+-RG})$, and D_e^{R2+} is equal to $D_e(\frac{M^{2+}-RG}{HM^+-RG})$

increasing the strength of the ion/induced-dipole interaction such that the subtle variations in dispersive and repulsive forces (which determine the trends for the M^+–RG) become less pertinent to the overall strength of interaction.

6.6 Conclusions

Investigation of the HM^+ species has revealed them to be strongly bound, with covalent bonding character. The highest occupied metal s orbital undergoes hybridisation (save for in Mg) with the lowest virtual p or d orbital (the p-orbitals are lower for M = Be, and the d-orbitals lower for M = Ca—Ra), and the resulting sp- or sd-hybrid interacts with the H 1s orbital. Interaction of these HM^+ species with rare gas atoms produces a bent or linear complex based on the angular momentum of the virtual orbital involved, as the rare gas atom positions itself so as to minimise the repulsive interaction with the HM^+ density and maximise exposure to the partially-exposed dicationic metal core.

For the majority of complexes, the interaction between metal and rare gas is physical in nature. Binding energies and M—RG bond lengths fall in between values previously calculated for the corresponding M^+–RG and M^{2+}–RG complexes, in line with expectations based on the partial atomic charges calculated for the metal centres in the triatomic species being ∼1.6—1.7 e. In many cases, D_e values are also found to have good correspondence with a simple ion/induced-dipole model, reinforcing the assertion that these complexes are predominantly bound by 'physical' forces.

Contour plots and $H(r)$ analysis show that, in addition to these physical interactions, there is a slight covalent character to the heavier HBe^+–RG complexes (RG = Ar—Rn), as well as HMg^+–Rn. The magnitude of $H(r)$ indicates that this covalent contribution is very slight however, on a much

smaller scale than the covalency in the HM^+ interaction.

Bibliography

[1] H.-J. Werner, P. J. Knowles, G. Knizia, F. R. Manby, M. Schütz *et al.*, MOLPRO , version 2012.1, a package of ab initio programs, 2012, see http://www.molpro.net.

[2] M. J. Frisch, et al., Gaussian 09, Revision D.01, Gaussian, Inc., Wallingford CT, 2010.

[3] E. D. Glendening, J. K. Badenhoop, A. E. Reed, J. E. Carpenter, J. A. Bohmann, C. M. Morales, C. R. Landis and F. Weinhold, NBO 6.0, Theoretical Chemistry Institute, University of Wisconsin, Madison, 2013.

[4] T. A. Keith, T. K. Gristmill Software, AIMAll, Overland Park, KS, 2011, see aim.tkgristmill.com.

[5] G. Schaftenaar and J. H. Noordik, *Journal of Computer-Aided Molecular Design*, 2000, **14**, 123–134.

[6] J. Koput, *The Journal of Chemical Physics*, 2013, **139**, 104309.

[7] J. A. Coxon and R. Colin, *Journal of Molecular Spectroscopy*, 1997, **181**, 215–223.

[8] M. Aymar, R. Guérout, M. Sahlaoui and O. Dulieu, *Journal of Physics B: Atomic, Molecular and Optical Physics*, 2009, **42**, 154025.

[9] M. Abe, M. Kajita, M. Hada and Y. Moriwaki, *Journal of Physics B: Atomic, Molecular and Optical Physics*, 2010, **43**, 245102.

[10] N. F. Dalleska, K. C. Crellin and P. B. Armentrout, *The Journal of Physical Chemistry*, 1993, **97**, 3123–3128.

[11] W. J. Balfour, *Canadian Journal of Physics*, 1972, **50**, 1082–1091.

[12] M. Aymar and O. Dulieu, *Journal of Physics B: Atomic, Molecular and Optical Physics*, 2012, **45**, 215103.

[13] R. Georgiadis and P. B. Armentrout, *The Journal of Physical Chemistry*, 1988, **92**, 7060–7067.

[14] P. Armentrout and J. Beauchamp, *Chemical Physics*, 1980, **48**, 315–320.

[15] W. M. Haynes, *CRC Handbook of Chemistry and Physics*, CRC Press/Taylor and Francis, Boca Raton, FL, 2014.

[16] A. M. Gardner, C. D. Withers, J. B. Graneek, T. G. Wright, L. A. Viehland and W. H. Breckenridge, *The Journal of Physical Chemistry A*, 2010, **114**, 7631–7641.

[17] M. F. McGuirk, L. A. Viehland, E. P. F. Lee, W. H. Breckenridge, C. D. Withers, A. M. Gardner, R. J. Plowright and T. G. Wright, *The Journal of Chemical Physics*, 2009, **130**, 194305.

[18] A. M. Gardner, C. D. Withers, T. G. Wright, K. I. Kaplan, C. Y. N. Chapman, L. A. Viehland, E. P. F. Lee and W. H. Breckenridge, *The Journal of Chemical Physics*, 2010, **132**, 054302.

Chapter 7

Resonance-Enhanced Multiphoton Ionisation Spectroscopy

For the experiments described in the following chapters, the key experimental technique employed has been resonance-enhanced multiphoton ionisation spectroscopy (REMPI).[1] This technique is best understood when compared to non-resonant multiphoton ionisation, as shown in scheme a) in Figure 7.1.

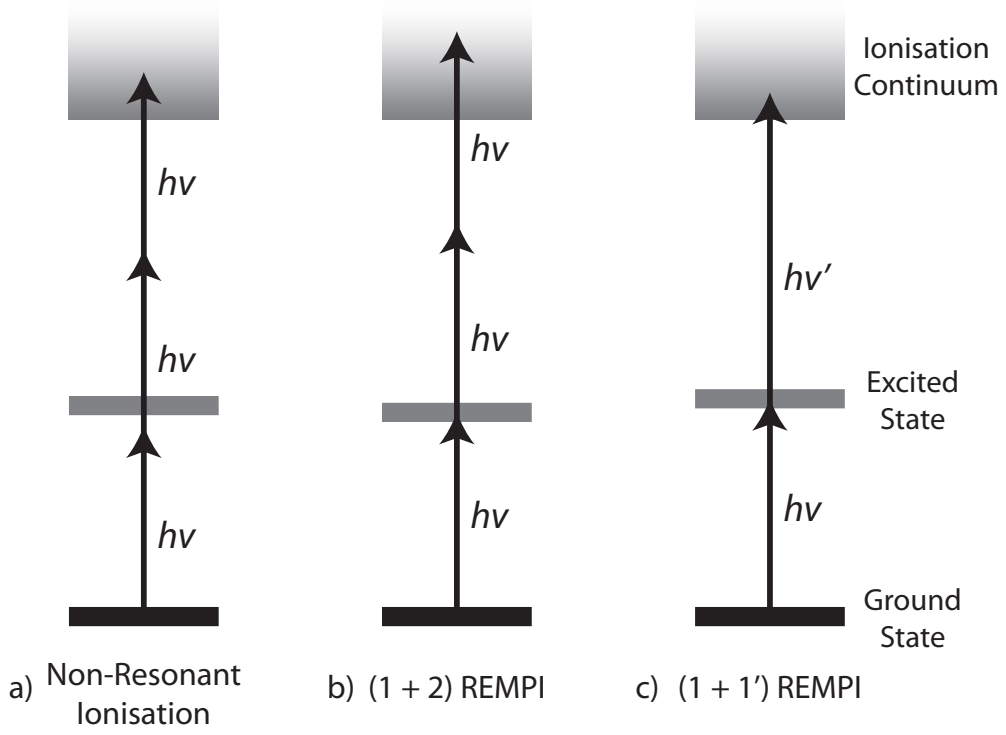


Figure 7.1: Schematic representation of different multiphoton ionisation regimes.

Molecules or complexes can be ionised by the absorption of photons of lower energy than the ionisation energy, IE, by the concurrent absorption of multiple photons. The probability of this concurrent absorption is very low (unless very high photon densities are used), usually resulting in a relatively low ion yield. However, if the energy of the incident photons matches that for some transition in the species, the absorption processes need no longer be concurrent, resulting in a much higher ion yield. Consequently, if the energy of the ionising photons is scanned and the ion yield monitored, increases in ion yield will correspond to some resonant transition having been accessed, referred to as resonance-enhanced multiphoton ionisation (REMPI), and plotting the ion yield against the excitation photon energy gives the REMPI spectrum.

Different REMPI schemes may occur depending on the specific energetics involved. Scheme b) in Figure 7.1 shows a one-photon excitation, two-photon ionisation scheme where both steps use the same photon energy. This can be described more concisely in the form (1 + 2). In other cases, different photon energies may be used for excitation and ionisation, such as is shown in scheme c) in Figure 7.1. A prime symbol is used to differentiate between the photons of different energies, with the abbreviation for this particular scheme being (1 + 1′).

The information that REMPI gives pertains to the intermediate excited state. Typically, the light source used will be a laser, which is scanned over some electronic transition. The structure within this spectrum will usually correspond to the rotational and vibrational structure—the extent to which this can be probed depends on the Franck-Condon factors between the ground and excited electronic states. Spin-orbit splitting effects are also observable, if they are present.

7.1 Experimental Apparatus

REMPI experiments described in the following chapters have been performed using the set-up seen in Figure 7.2. A pair of neodoymium-doped yttrium-aluminium-garnet (Nd:YAG) lasers (Continuum Surelite I and Surelite III) are used to pump either one or two dye lasers (Sirah Cobra Stretch). Depending on whether the 2^{nd} (532 nm) or 3^{rd} (355 nm) harmonic of the Nd:YAGs is used as the pump wavelength, and which dye is used, the dye lasers are capable of highly tunable visible light generation with a bandwidth of $\sim$0.1 cm^{-1}. This visible output is then typically frequency-doubled into the UV by means of second harmonic generation (SHG) crystals, giving a highly tunable UV source with a narrow bandwidth well suited to probing vibronic transitions. The bandwidth of these lasers are able to resolve different vibrational features, and often identify the P and R branches of the associated rotational envelopes.

Gaseous samples are mixed in a stagnation volume held at a typical pressure of $\sim$5 bar, with a low partial pressure of the species of interest and a high partial pressure of backing gas (usually argon). Liquid samples can be introduced by means of an in-line liquid sample holder between the stagnation volume and the vacuum chamber, in which the backing gas is passed over a small amount of liquid sample held in a small volume in order to pick up the vapour.

Backing gas seeded with a small amount of sample is then passed into the nozzle chamber through a pulsed valve with an orifice of 750 μm, forming a supersonic jet expansion. Crucial to the formation of a supersonic jet expansion is the criterion that the diameter of the nozzle must be greater than the mean-free path of the gas. Consequently, the relative translational temperature of the gas molecules/atoms becomes extremely low as the

velocities are averaged through exchange of kinetic energy over numerous collisions. This process will result in a distribution of translational energies with a much narrower spread and a slightly higher average than when compared to a sample with a Maxwell-Boltzmann distribution.

Rotational and vibrational cooling is also achieved, by means of collisional deactivation of excited states in the sample by transferring the (ro)vibrational energy to backing gas atoms in the form of momentum. This ensures that the sample is spectroscopically cold, and helps remove hot bands arising from transitions from the excited vibrational and rotational states in the ground electronic state. Were it not for this, the spectra recorded would be congested with these warm features, greatly impairing the assignment of any cold bands present.

This supersonic jet expansion proceeds unskimmed into the ionisation chamber, where it intersects the focussed UV laser beam(s) between two grids with different magnitudes of positive charge applied so as to create

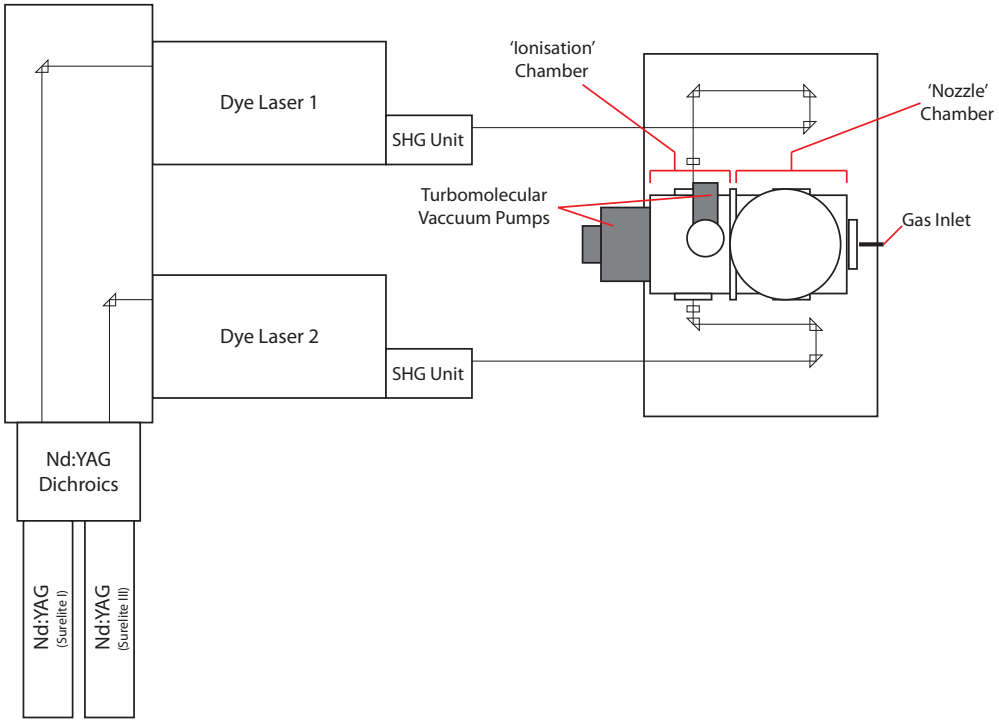


Figure 7.2: Diagram of the experimental apparatus used to perform REMPI.

an electric field between them. These grids essentially form the extraction region of a time-of-flight (TOF) mass spectrometer, a photograph of which can be seen in Reference 2, and any ions formed here by photoionisation are extracted and allowed to proceed along a field-free region 1 m in length. At the end of this TOF tube, the ions are incident upon a pair of microchannel plate (MCP) detectors in a chevron arrangement which serve to translate the ion count into a measurable voltage. This signal is then passed to a boxcar for integration over selected times-of-flight (and by relation, ion masses), and then subsequently on to both an oscilloscope for imaging of the signal, and a computer for data storage and analysis.

Digital delay generators (SRS DG535) are employed in order to make sure the pulsed valve and the lasers operate at the correct time, which is especially sensitive when aligning two laser pulses to arrive simultaneously in the ionisation region as the pulse widths are only a few nanoseconds. Adjustment of the laser delay relative to the pulsed nozzle operating also allows different parts of the supersonic jet expansion to be probed, with the coldest molecules or complexes being formed at the front of the expansion.

In some cases, such as when attempting to detect complexes, uncomplexed species may have an extremely intense non-resonant multiphoton ionisation cross-section. As such, the detection equipment may experience an intense ringing signal lasting several microseconds, introducing significant noise and effectively masking the signal arising from any species which arrive shortly afterwards. Introduction of some sort of 'mass gate' proves necessary in these cases. In this laboratory, this has been achieved by a length of copper being positioned in front of the MCPs and connected to a pulsed voltage supply. A high positive potential is then pulsed to coincide with the arrival

of the interfering species which removes the associated intense signal.[3]

Bibliography

[1] A. Ellis, M. Feher and T. Wright, *Electronic and Photoelectron Spectroscopy*, University Press, Cambridge, 2005.

[2] V. L. Ayles, *Spectroscopy of Small Molecules and Clusters*, PhD Thesis, University of Nottingham, 2008.

[3] V. M. Tamé-Reyes, A. M. Gardner, J. P. Harris, J. McDaniel and T. G. Wright, *The Journal of Chemical Physics*, 2012, **137**, 214307.

Chapter 8

Spectroscopy of Laser-Ablated Copper: Towards Copper-Containing Complexes

8.1 Introduction

Experimental detection of metal cation–RG complexes is decidedly non-trivial.

The intent behind these experiments was to record REMPI spectra of small copper-containing molecules such as CuSH and $CuSCH_3$. These molecules serve as simple models for the active sites of copper proteins, wherein the copper atoms are typically bound by sulphur atoms from nearby amino acid residues, such as cystein. Such proteins are ubiquitous throughout biology and are highly important in many processes—for example, plastocyanin is a sulphur-containing protein which is vital to photosynthesis. In spite of this, the binding of copper in these molecules is quite poorly understood.

As a precursor to these studies, spectra of the Cu–RG complexes were to be recorded for RG = Ne, Ar, Kr, and Xe. These RG complexes provide a

further simplified environment in which to study how copper atoms interact with ligands. Of these complexes, only Cu–Kr had been previously recorded,[1] despite the corresponding series of gold[2–5] and silver[6,7] complexes being previously studied. Additionally, these complexes have been the subject of many theoretical studies—see reference 8 and references therein.

As mentioned in Chapter 1, rare gas complexes provide useful models for studying solvation, and especially building up from micro-solvation (interaction with only a few solvent molecules/atoms) towards bulk solvation. Effects of micro-solvation, however, are essentially only able to be studied under gas phase conditions, and so gas phase techniques are a necessity.

Gas phase studies can be carried out quite straightforwardly on gaseous precursors, and many liquid precursors will have sufficient volatility that vapour can be picked up from the surface and seeded into an inert gas. Solid precursors however, such as pure copper, present a challenge as atoms must be somehow put into the gas phase before the experiment can proceed. In some cases, simply heating the sample e.g. in a crucible is viable, allowing the vapour produced to be picked up by backing gas and subsequently cooled in a supersonic jet expansion, although this technique may be problematic for samples with very high boiling points. Furthermore, problems may be caused by deposition of solid in the system if the whole of the sample delivery system is not heated sufficiently.

For the experiments described in this chapter, the method employed to produce gas-phase copper atoms is laser vaporisation (LaVa), also known as laser ablation. This particular method is highly versatile, as virtually any material not transparent to the ablation wavelength should produce a plasma from its surface upon intense irradiation from a laser. This short-lived plasma will cool, and the products can then be seeded into a carrier gas and collisionally cooled in the usual manner.

Although these experiments ultimately did not give the results sought, the spectra of atomic copper obtained gave some interesting results, and so are discussed here, the original analysis for which was led by Anna Andrejeva. Additionally, the spectrum of Cu–Kr presented in reference 1 shows some interesting inconsistencies with other work on the Group 12–Kr complexes; these are discussed, with possible reasons suggested.

8.2 Experimental

The technique used for the experiments described in this chapter is REMPI spectroscopy, as outlined in Chapter 7. Both one-colour and two-colour REMPI schemes were used. In both cases, the excitation wavelength was the frequency-doubled output of a dye laser operated with DCM, pumped with the second harmonic (532 nm) of a Nd:YAG laser (Continuum Surelite III). This gave a typical maximum pulse energy of 5—6 mJ / pulse of UV. For the experiments in which two lasers were used, the fourth harmonic (266 nm) of a Nd:YAG laser (Continuum Surelite I) was used for the second colour.

The instrument used was that described in Chapter 7, with a major modification in the form of a LaVa source. This is mounted on the front of the pulsed valve in the 'nozzle' chamber, and is constructed from a piece of polyether ether ketone (PEEK), a cross-section of which is shown in Figure 8.1. The ablation laser beam is steered into the LaVa source via the indicated conical aperture and produces a plasma from the surface of the copper rod (Goodfellow, 99.99% purity). The cooled plasma is then seeded into backing gas from the pulsed nozzle, and a supersonic jet expansion is formed at the end of the long channel. Several PEEK nozzles were fabricated with different lengths of channel in each case, the effects of which will be discussed later.

The metal rod is suspended perpendicular to the direction of both the

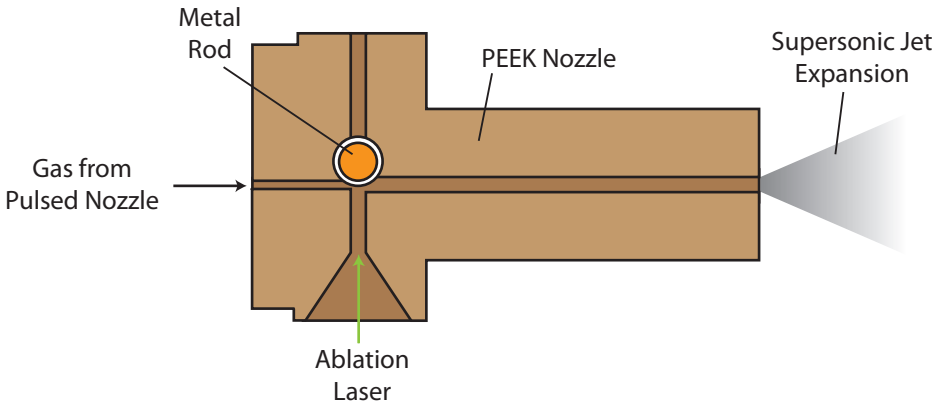


Figure 8.1: Schematic of the LaVa source.

gas and laser beam (i.e. in the plane of Figure 8.1) from a motor assembly. This motor facilitates movement of the rod both vertically and rotationally, ensuring that a fresh surface of rod is exposed to the ablation laser at all times to maintain consistent production of plasma. It was found in many cases that the consistency of observed copper signal was in fact more stable with the metal rod held stationary: when the motor was rotating the rod, the signal observed whilst 'sitting' on a particular resonant transition would fluctuate quite severely; conversely, with a stationary rod, the signal was seen to be far more consistent and, despite fears of this signal quickly decaying as the surface of the copper was ablated away, was seen to remain consistent for several hours at a time. Fluctuations with rotation of the rod were determined to occur on the same time scale as the rotation of the rod itself, and so the mount was fitted with metal bush to arrest precession of the rod in the nozzle; although this helped somewhat, the signal intensity was still seen to be much steadier with the motor turned off. Consequently, the spectra presented here were recorded with a stationary target.

For the ablation laser, the second harmonic (532 nm) of a Nd:YAG laser (Continuum Minilite I) was used, and focussed onto the copper rod using a 30 mm lens. Laser powers were optimised so as to give the best compromise between abundance of copper produced and the consistency of this signal

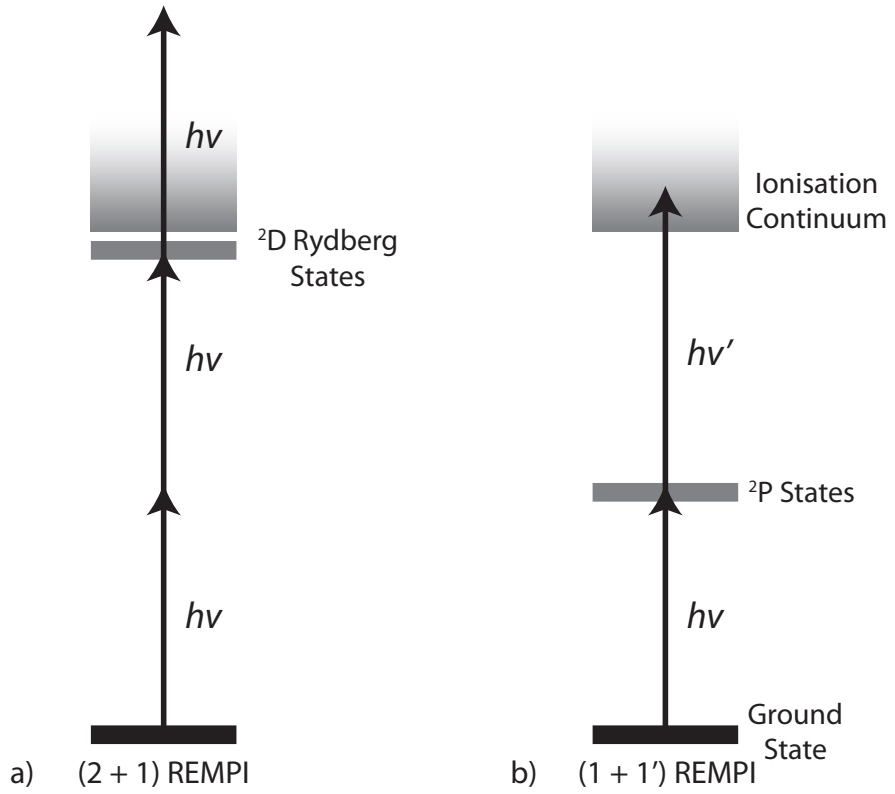


Figure 8.2: Different REMPI schemes used. Trace a) shows the one-colour (2 + 1) REMPI process responsible for the ^{2}D Rydberg spectrum, and trace b) the two-colour (1 + 1′) REMPI process which leads to the observation of the ^{2}P spectrum.

over time, with typical energies of ∼5 mJ / pulse being used.

Collisions between the gas pulse and the channel of the ablation source will cause the gas pulse to become elongated, and so the integrity may be compromised which can in turn spoil the subsequent supersonic jet expansion. Higher pressures of backing gas are used to counteract this, typically in the region of ∼12 bar, with argon being used as the inert gas.

A liquid nitrogen cooling system was also used for some of the experiments. A reservoir of liquid nitrogen was held outside of the vacuum chamber, and connected to a cooling ring designed to fit around the channel of the PEEK nozzle. However, there was no clear evidence of an improvement in the quality of the results obtained when the coolant was used, and so this went largely unused.

8.3 Spectra of Atomic Copper

Two different REMPI schemes were employed, a (2 + 1) and a (1 + 1′) scheme, as outlined in Figure 8.2. Depending on the scheme used, very different spectra were observed. Use of a single colour at high intensity for both excitation and ionisation led to two-photon excitation of a series of $3d^{10}nd$ Rydberg states, with one additional photon ionising these states. When the excitation laser was used at lower intensities and 266 nm light used for ionisation, there were instead one-photon excitations observed to a lower-lying ^{2}P state arising from the $3d^{10}4p^1 \leftarrow 3d^{10}4s^1$ transition, with ionisation from these states occurring by one 266 nm photon.

8.3.1 One-Colour (2 + 1) REMPI Spectra

The spectrum resulting from the (2 + 1) REMPI scheme is shown in trace a) of Figure 8.3. Seen in this spectrum are $3d^{10}nd$ bands arising from $n = 8$—17, with a large step in intensity attributed to the ionisation energy being reached.

As these transitions proceed *via* a two-photon excitation process, the pertinent selection rules using LS-coupling are $\Delta l = 0, \pm 2$ and $\Delta J = 0, \pm 1$, ± 2 ($J = 0 \leftarrow 0$ forbidden), with $\Delta S = 0$. Thus, from the ground $^2S_{\frac{1}{2}}$ state, ^{2}D states with both $J = \frac{3}{2}$ and $\frac{5}{2}$ are accessible. Higher values of n result in lower magnitudes of spin-orbit splitting, and so the laser bandwidth used is insufficient to resolve both J states in this spectrum fully.

Along with the $3d^{10}nd$ series of Rydberg states, there are also numerous $3d^{10}ns$ and $3d^{10}np$ metastable states over the same energetic region; however, transitions to the np states are forbidden for two-photon transitions (since $\Delta l = 1$),and transitions to these states are not expected to be observed. Curiously, although the zero-order rank transition tensor component of the

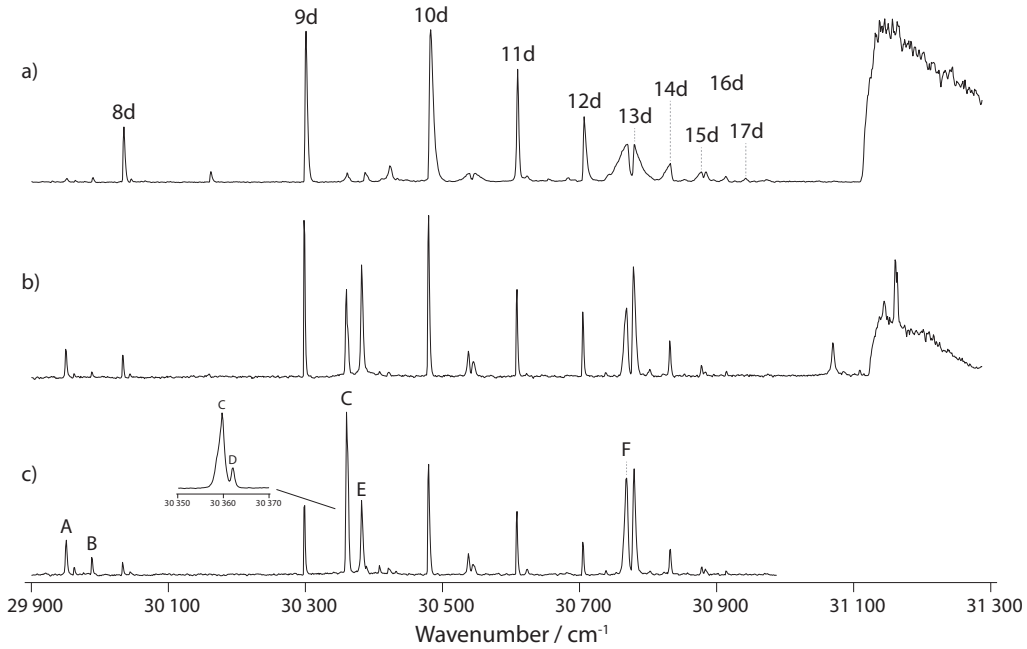


Figure 8.3: REMPI spectrum of ^{63}Cu, recorded under one-colour conditions. Trace a) shows mainly contributions from $3d^{10}n$d $\leftarrow$ $3d^{10}4$s transitions, trace b) shows increasing contributions from transitions originating from metastable excited electronic states, and in trace c) some metastable transitions are seen to be more intense than the $3d^{10}n$d lines.

two-photon transition does allow s $\leftarrow$ s transitions, no transitions to ^{2}S Rydberg states are observed in these spectra, as has also been found by others over the same energetic region previously.[11]

Measured line positions, E_n, of each of these $3d^{10}n$d bands are given in Table 8.1, along with positions from previous studies. Calibration of these line positions was achieved by means of comparison to lines previously recorded by Sugar and Musgrove.[9] The wavenumber precision achievable

Band Assignment	Measured Position / cm^{-1}	Sugar and Musgrove[9]	Loock *et al.*[10]	Castleberry *et al.*[11]
$3d^{10}$ 8d	60 065.6	60 066.33	-	60 066.19
$3d^{10}$ 9d	60 596.0	60 595.05	60 595.6	60 594.90
$3d^{10}$ 10d	60 957.2	60 957.35	60 961.4	60 957.07
$3d^{10}$ 11d	61 214.8	61 215.59	61 216.0	61 215.96
$3d^{10}$ 12d	61 407.2	-	61 408.0	61 407.39
$3d^{10}$ 13d*	61 554.0	-	61 557.4	61 552.93
$3d^{10}$ 14d	61 661.6	-	61 662.8	61 666.15
$3d^{10}$ 15d	61 754.4	-	61 754.6	61 755.96
$3d^{10}$ 16d	61 825.2	-	61 826.6	61 828.40
$3d^{10}$ 17d	61 883.2	-	61 885.4	61 887.66

* This band is overlapped by other features, affecting the measured position.

Table 8.1: Measured band positions for the $3d^{10}n$d series, including previous positions reported by previous studies.

is estimated to be ∼0.4 cm^{-1}, although the width and asymmetry of the spectral features means that the measured line positions here are less precise than this. Taking the measured positions allows them to be fit using a least squares procedure to the Rydberg equation;

$$E_n = IE - \frac{R}{(n-\delta)^2} \tag{8.1}$$

where IE is the ionisation energy, n is the principal quantum number, δ is the quantum defect, and R is the Rydberg constant (specifically, R_∞—although the Rydberg constant for copper, R_{Cu}, will differ from R_∞, the difference is so small that it will have essentially no effect on the results obtained). By fitting the measured band positions, it is possible to determine simultaneously the ionisation energy and the quantum defect. The quantum defect is a useful quantity when considering Rydberg states as it allows a quantitative analysis of how much a given state deviates from hydrogenic behaviour.

Fitting to the Rydberg equation yields IE = 62 317(6) cm^{-1} and δ = 1.02(9). These values are seen to be in excellent agreement with the measurements of Loock *et al.*,[10] which gave IE = 62 317.3(2) cm^{-1} and δ = 1.018(2), measured using optical-optical double resonance and pulsed-field ionisation. Equally excellent agreement is seen with the work of MacAdam *et al.*[12] using microwave spectroscopy, which reported IE = 62 317.46(3) cm^{-1}. An analysis of data recorded using REMPI by Castleberry *et al.*[11] extrapolated the 6 highest 3d^{10}nd bands observed in their spectra (n = 15—21) to $n = \infty$ to obtain a value for IE, found to be 62 337 cm^{-1}, in slightly worse agreement with other results discussed here. In a subsequent fitting procedure, IE was fixed to the established experimental value taken from the NIST database,[13] and their experimentally observed band positions fitted to obtain δ = 0.92(3); again, this is seen to be in somewhat worse agreement with other results.

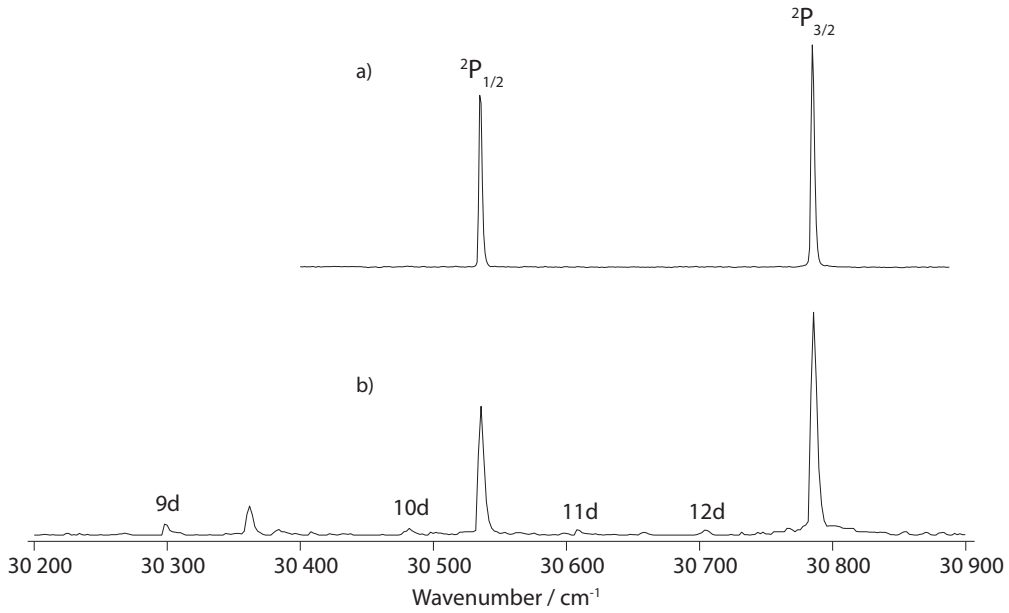


Figure 8.4: REMPI spectrum of ^{63}Cu using (1 + 1′) REMPI conditions, with low (trace a) and higher (trace b) excitation laser powers.

8.3.2 Two-Colour (1 + 1′) REMPI Spectra

Use of the (1 + 1′) REMPI scheme produces the spectrum shown in Figure 8.4. The bands observed in this spectrum are straightforwardly attributable to transitions to the low-lying ^{2}P state. Relevant selection rules for this one-photon excitation are $\Delta l = \pm 1$, $\Delta J = 0, \pm 1$ ($J = 0 \leftarrow 0$ forbidden), and $\Delta S = 0$. Consequently, excitations to both $^2\mathrm{P}_{\frac{1}{2}}$ and $^2\mathrm{P}_{\frac{3}{2}}$ should be observable, and two corresponding strong features are present in the spectrum.

Additionally, two distinct regimes are shown in Figure 8.4; trace a) shows a spectrum which has been recorded using low excitation energies (∼0.5 mJ/pulse), and shows only two intense bands corresponding to excitation to the two components of the ^{2}P state. Trace b) shows a spectrum for which the excitation energies are much higher (∼5 mJ / pulse) and demonstrates clear contributions to the $^2\mathrm{P} \leftarrow {}^2\mathrm{S}$ spectrum in the form of much weaker features. These bands are found to show excellent correspondence to the bands seen in the one-colour experiments, seen in trace a) of Figure 8.3,

and as such are assigned to the same two-photon excitations to the $3d^{10}nd$ series produced by scheme a) as depicted in Figure 8.2.

8.3.3 Metastable States of Copper

In the one-colour REMPI spectrum in trace a) of Figure 8.3, along with the bands seen arising from the $3d^{10}nd \leftarrow 3d^{10}4s$ transition, additional features are seen throughout. Spectra are seen in traces b) and c) in which these additional features are more prominent. No convincing assignments could be found for these bands amongst transitions originating from the ground electronic state, and so possible assignments were expanded to include transitions from higher electronic states. Amongst these, transitions were identified which fitted the observed band positions very well, and these are presented in Table 8.2, with the energies of the states involved listed in Table 8.3.

Most of the proposed assignments originate from the $3d^94s^2(^2D_{\frac{5}{2}})$ state; this state has no allowed one-photon optical decay route by which to relax to the ground state, as the s $\leftarrow$ d transition would require $\Delta l = 2$. Additionally, even when *jj* coupling is considered and transitions between levels with the same J value are allowed, the transition to the ground state would require $\Delta J = 2$ which is also forbidden. Thus, the $^2D_{\frac{5}{2}}$ state is expected to be reasonably long lived, making assignments of transitions from this state quite reasonable.

Other transitions are assigned as arising from the $3d^94s4p(^4F_{\frac{9}{2}})$ initial state. This state cannot decay to the lower-lying ^4P states as they have at most $J = \frac{5}{2}$, which would require a $\Delta J = 2$ transition, which is forbidden. Additionally, these lower-lying ^4P states would be able to decay to the lower ^2D states which, although formally forbidden by Russell-Saunders coupling, is allowed if *jj* coupling is important. Consequently, this $^4F_{\frac{9}{2}}$ state

Spectral Feature	Observed Position (one-photon) cm^{-1}	Photon Order	Assigned Transition
A	29 950.0	1	$3d^9 4s4p(^4F_{7/2}) \leftarrow 3d^9 4s^2(^2D_{5/2})$
		1	$3d^9 4s4d(^2G_{9/2}) \leftarrow 3d^9 4s4p(^4F_{9/2})$
B	29 988.2	2	$3d^9 4s4d(^4P_{5/2}) \leftarrow 3d^9 4s^2(^2D_{5/2})$
C	30 359.7	1	$3d^9 4s4p(^4F_{5/2}) \leftarrow 3d^9 4s^2(^2D_{5/2})$
		2	$3d^9 4s5p(^2P_{3/2}) \leftarrow 3d^9 4s^2(^2D_{5/2})$
		1	$3d^9 4s4d(^4D_{7/2}) \leftarrow 3d^9 4s4p(^4F_{9/2})$
D	30 362.1	2	$3d^9 4s4d(^4P_{3/2}) \leftarrow 3d^9 4s^2(^2D_{5/2})$
E	30 381.9	1	$3d^9 4s4d(^4F_{9/2}) \leftarrow 3d^9 4s4p(^4F_{9/2})$
F	30 767.3	2	$3d^9 4s5p(^2P_{1/2}) \leftarrow 3d^9 4s^2(^2D_{5/2})$

Table 8.2: Assignments of the additional features observed in the (2 + 1) REMPI spectra. Energies of the states involved relative to the ground state are collected in Table 8.3.

is expected to be the longest lived quartet state.

As can be seen from the different spectra in Figure 8.3, the intensities of the transitions involving metastable states are not always consistent with the cold bands. In trace a), the transitions to the $3d^{10}n$d series clearly dominate the spectrum, and in trace b) the additional features are seen to be of comparable intensity to the $3d^{10}n$d transitions. Conditions for the recording of trace c) show some transitions from metastable initial states of greater intensity than the cold transitions. Although the differences between these regimes are marked, the reasons as to why this occurs are not so apparent. All experimental variables that could be reasonably expected to effect these changes in intensity were varied over the course of recording the spectra, and no one variable was found to impact the spectra significantly.

Factors relating to the production of the copper plasma would seem the

State	Energy / cm^{-1}
$3d^9 4s^2(^2D_{5/2})$	11 202.57
$3d^9 4s4p(^4F_{9/2})$	40 909.138
$3d^9 4s4p(^4F_{7/2})$	41 153.433
$3d^9 4s4p(^4F_{5/2})$	41 562.895
$3d^9 4s4d(^2G_{9/2})$	70 859.53
$3d^9 4s4d(^4P_{5/2})$	71 178.19
$3d^9 4s4d(^4D_{7/2})$	71 268.21
$3d^9 4s4d(^4F_{9/2})$	71 290.54
$3d^9 4s5p(^2P_{3/2})$	71 917
$3d^9 4s4d(^4P_{3/2})$	71 927.22
$3d^9 4s5p(^2P_{1/2})$	72 737.8

Table 8.3: Energetic positions of the states involved in the transitions from metastable states above the ground state.

most likely candidates, such as the ablation laser's power, alignment, and timing relative to the gas pulse arriving, and so these were varied. Although it is perhaps unlikely that the supersonic jet expansion would be able to cool electronic states by means of standard collisional cooling, the conditions of this were also varied, including the pressure of backing gas and time for which the pulsed valve remains open. The conditions under which the atoms are ionised were also adjusted, including laser alignment and power, as well as the strength of the extracting electric field. Considering the PEEK nozzle, it seems conceivable that the length of exit channel could play a role in how many metastable states are able to survive for long enough to be excited and ionised—using different lengths of channel and even forgoing a nozzle altogether and attempting free ablation experiments gave no systematic variation in the relative intensities of different transitions.

In order for excited states to be detected, they must be initially produced by the laser ablation source, and then remain populated upon pick-up by the carrier gas and through the nozzle channel, as well as survive the supersonic jet cooling process. Of particular note is the fact that the metastable states must also remain populated for a reasonable length of time after this in order to reach the ionisation region. Assuming the speed of the supersonic jet expansion is equivalent to the root mean square speed of the carrier gas (argon) at 293 K, the velocity of the expansion can be found as $\sim$430 m s^{-1}. Since the distance between the ablation source and ionisation region is known to be $\sim$0.25 m, it is trivial to find the time it takes for the gas to traverse this distance as $\sim$600 μs. Another estimate for the lifetimes can be found by comparing the timings of the ablation and ionisation lasers, thus giving the approximate time between the population and ionisation of the excited states—this gives an even greater value, at $\sim$800 μs. From these, it is highly unlikely that any excited electronic states with any pathway to the

ground state by radiative decay would still be populated in the ionisation region. From these various factors, it seems plausible that at least part of the metastable states' populations come from decaying higher-lying states, which would serve to effectively reduce the time for which the excited states would need to survive to be detected.

8.4 Cu–Kr Complex

Of the copper–rare gas complexes which were the aim of the experiments described here, Cu–Kr is of special interest as it is the only member of the series which has been previously experimentally identified. That study was conducted by Brock and Duncan,[1] and their spectrum is shown in Figure 8.5.

Clearly marked in the spectrum are two separate progressions, corresponding to the $^2\Pi_{\frac{1}{2}} \leftarrow {}^2\Sigma_{\frac{1}{2}}$ and $^2\Pi_{\frac{3}{2}} \leftarrow {}^2\Sigma_{\frac{1}{2}}$ transitions. Since the excitation is localised to the copper atom, these transitions are analogous to the atomic $^2\mathrm{P}_{\frac{1}{2},\,\frac{3}{2}} \leftarrow {}^2\mathrm{S}_{\frac{1}{2}}$ transitions seen in Figure 8.5. Each electronic transition also shows an associated vibrational progression.

It is stated in reference 1 that the Cu–Kr spectrum is reported to have been recorded by resonant two-photon ionisation spectroscopy (R2PI), equivalent to (1 + 1) REMPI. This would appear to be at odds with the spectra presented here, which under one-colour conditions required three photons to reach the ionisation limit for Cu, with the $3d^{10}nd$ features arising from (2 + 1) REMPI dominating the one-colour spectrum and the (1 + 2) ^{2}P features being negligible; however, the ionisation energy of Cu–Kr is less than that of atomic Cu. This effect arises due to the relative binding energies of Cu–Kr and Cu^+–Kr, which have been found by high-level *ab initio* calculations (including correction for zero-point effects) as 134.3 and 5 799.6 cm^{-1} respectively[8,14]. Taking the difference between these values gives the reduction in the ionisation energy for the complex, and so the ionisation

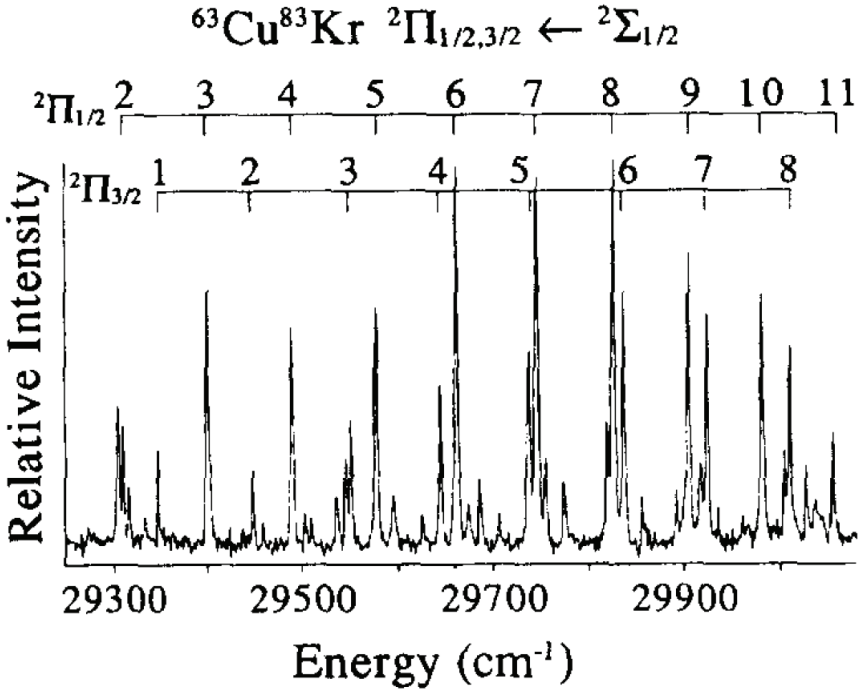


Figure 8.5: Spectrum of Cu–Kr recorded using one-colour (1 + 1) REMPI, taken from Reference 1.

energy of Cu^+–Kr is found to be ∼56 650 cm^{-1}. A second photon of the same energy as the first is thus seen to be sufficient to ionise the complex.

Since spectra were recorded for both ^{63}Cu and ^{65}Cu isotopes, absolute vibrational numbering for each observed member of a progression is assignable by use of the isotopic shifts according to Equation 8.2;

$$\Delta v = (1-\rho)\omega_e(v+\frac{1}{2}) - (1-\rho)^2\omega_e x_e(v+\frac{1}{2})^2 \tag{8.2}$$

where Δv is the observed isotopic shift, and ρ is related to the ratio of the reduced masses μ_1 and μ_2, where μ_1 is that of the isotope of interest;

$$\rho = \sqrt{\frac{\mu_1}{\mu_2}} \tag{8.3}$$

Using different trial values for v, ω_e, and $\omega_e x_e$, a set of values can be found which give the best agreement with the observed isotopic shifts. Using this method, Duncan and co-workers were able to assign absolute vibrational

numberings of $v' = 1$—13 for the $\Delta J = 0$ transition, and $v' = 1$—9 for $\Delta J = 1$.

This Franck-Condon allowed region is seen to be in contrast with the results for Ag–Kr and Au–Kr recorded *via* the same electronic transition. For Ag–Kr, Duncan and coworkers reported seeing cold transitions corresponding to $v' = 17$—31 for the $^2\Pi_{\frac{3}{2}} \leftarrow {}^2\Sigma_{\frac{1}{2}}$ transition for the ^{109}Ag–^{86}Kr isotopomer which showed the most extensive progression.[6] Similarly high-numbered vibrational features have been observed for Au–Kr, with the most extensive progression being $v' = 22$—31, seen for ^{197}Au–^{84}Kr.[4] Although it is far from inconceivable that the Franck-Condon factors for Cu–Kr would be different, it seems surprising that there should be such a drastic change observed compared to the other Group 12–Kr complexes.

Analysis by Duncan and co-workers also included calculation of D_0'' for the $^2\Sigma$ state using both spin-orbit split components of the $^2\Pi$ state, and proposed that the value of 408 cm^{-1} from the $\Delta J = 0$ transition is more accurate owing to the more extensive vibrational progression observed there. This value also goes against the trend seen for the Ag–Kr and Au–Kr complexes, as experimental data provides the corresponding value for Ag–Kr as 138 cm^{-1},[6] and 240 $\pm$19 cm^{-1} for Au–Kr.[4] This notably elevated result for Cu–Kr is also at odds with the results of theoretical investigations, in which D_0 for the ground state has been predicted using CCSD(T) theory and large basis sets to be 134.3 cm^{-1}.[8] Similar calculations on the other krypton complexes discussed here gave reasonable agreement with the experimental results, and so it seems as though the value for D_0'' of 408 cm^{-1} is somewhat elevated.

Inconsistencies with the rest of the Group 12–Kr complexes as well as *ab initio* results imply that the spectrum in Figure 8.5 does not necessarily correspond to $^2\Pi \leftarrow {}^2\Sigma$ transition. Indeed, it was remarked upon in reference

1 that some features in the spectrum do not belong to the main progression. Although no assignments were suggested for these features, it was noted that further experiments were being conducted; however, these were never published.

It is possible that these features belong to two-photon excitations, analogous to the observation of the (2 + 1) $3d^{10}nd$ lines discussed in this chapter. Since a two-photon excitation would ionise the complex, in this case the excited states would have to be Rydberg states converging on an excited state of the cation.

8.5 Conclusions

Experiments were undertaken on copper atoms produced by means of laser ablation. No signals were observed corresponding to the formation of Cu–RG complexes. Some experiments which included a low partial pressure of N_2O mixed with the backing gas did give some signal in the copper mass channel which correlated with some of the lines observed by Parry *et al.*[15] indicating the presence of CuO; also in line with that study, no spectrum could be recorded in the precursor mass channel.

Despite this, spectra were recorded of atomic copper *via* the $3d^{10}4p \leftarrow 3d^{10}4s$ transition, with both the $^2\Pi_{\frac{1}{2}} \leftarrow {}^2\Sigma_{\frac{1}{2}}$ and $^2\Pi_{\frac{3}{2}} \leftarrow {}^2\Sigma_{\frac{1}{2}}$ transitions observed. These bands were only strongly observable under a two-colour (1 + 1′) REMPI scheme—when only one-colour of the excitation wavelength employed here was used, the ionisation energy of atomic copper is too high to be ionised by two photons, and instead a very different spectrum was observed. The dominant features in this spectrum correspond to a (2 + 1) REMPI scheme, ionising *via* a series of high-lying $3d^{10}nd$ Rydberg states.

In addition to the $3d^{10}nd \leftarrow 3d^{10}4s$ transitions, there are additional features observable in the one-colour spectrum which were assigned as tran-

sitions originating from excited electronic states. As these states would have to remain populated for ∼600—800 μs, the initial states for these excitations cannot have any efficient decay mechanisms. Both the $3d^9 4s^2(^2D_{\frac{5}{2}})$ and $3d^9 4s4p(^4F_{\frac{9}{2}})$ electronic states lack these mechanisms and would be expected to have a long lifetime—furthermore, assignments have been found from these states which concur with the observed transition energies.

Relative intensities of the $3d^{10}n$d $\leftarrow$ $3d^{10}$4s bands compared to the features from metastable transitions are seen to differ; although spectra have been recorded wherein different regimes of relative intensities are observable, the exact conditions responsible for these different regimes remain unclear, despite systematic investigation.

Bibliography

[1] L. Brock and M. Duncan, *Chemical Physics Letters*, 1995, **247**, 18 – 23.

[2] R. J. Plowright, A. M. Gardner, C. D. Withers, T. G. Wright, M. D. Morse and W. H. Breckenridge, *The Journal of Physical Chemistry A*, 2010, **114**, 3103–3113.

[3] R. J. Plowright, V. L. Ayles, M. J. Watkins, A. M. Gardner, R. R. Wright, T. G. Wright and W. H. Breckenridge, *The Journal of Chemical Physics*, 2007, **127**, 204308.

[4] R. J. Plowright, M. J. Watkins, A. M. Gardner, T. G. Wright, W. H. Breckenridge, F. Wallimann and S. Leutwyler, *The Journal of Chemical Physics*, 2008, **129**, 154315.

[5] R. J. Plowright, M. J. Watkins, A. M. Gardner, C. D. Withers, T. G. Wright and W. H. Breckenridge, *Phys. Chem. Chem. Phys.*, 2009, **11**, 1539–1550.

[6] L. R. Brock and M. A. Duncan, *The Journal of Chemical Physics*, 1995, **103**, 9200–9211.

[7] T. Diederich, J. Tiggesbaumker and K.-H. Meiwes-Broer, *The Journal of Chemical Physics*, 2002, **116**, 3263–3269.

[8] A. M. Gardner, R. J. Plowright, M. J. Watkins, T. G. Wright and W. H. Breckenridge, *The Journal of Chemical Physics*, 2010, **132**, 184301.

[9] J. Sugar and A. Musgrove, *Journal of Physical and Chemical Reference Data*, 1990, **19**, 527.

[10] H.-P. Loock, L. M. Beaty and B. Simard, *Phys. Rev. A*, 1999, **59**, 873–875.

[11] V. Castleberry, J. Dee, O. Villarroel, I. Laboren and D. Bellert, *Physics Letters A*, 2008, **372**, 4805 – 4808.

[12] K. B. MacAdam, S. F. Dyubko, V. A. Efremov, V. G. Gerasimov and A. S. Kutsenko, *Journal of Physics B: Atomic, Molecular and Optical Physics*, 2009, **42**, 165009.

[13] A. Kramida, Yu. Ralchenko, J. Reader and and NIST ASD Team, NIST Atomic Spectra Database (ver. 3.1.4), [Online]. Available: `http://physics.nist.gov/asd` [2008, March 24]. National Institute of Standards and Technology, Gaithersburg, MD., 2008.

[14] A. Yousef, S. Shrestha, L. A. Viehland, E. P. F. Lee, B. R. Gray, V. L. Ayles, T. G. Wright and W. H. Breckenridge, *The Journal of Chemical Physics*, 2007, **127**, 154309.

[15] I. S. Parry, A. C. Hermes, A. Kartouzian and S. R. Mackenzie, *Phys. Chem. Chem. Phys.*, 2014, **16**, 458–466.

Chapter 9

Spectroscopy of NO–Alkane Complexes

9.1 Introduction

The species covered in this chapter, the NO–alkane complexes (where alkane = methane, ethane, propane, and *n*–butane i.e. unbranched butane) are all neutral species, as well as being ground state radicals due to the $X^2\Pi$ state of NO. Such complexes can provide insight into interactions between radical and neutral species, and as such are sometimes referred to as 'pre-reaction' or 'encounter' complexes. Additionally, NO also possesses a relatively low-lying series of Rydberg states, which makes it ideal for use in the investigation of Rydberg complexes. The molecule is also attractive for study from a practical standpoint, as it possesses a very high oscillator strength and so absorbs photons very readily, often resulting in the recording of spectra with very high signal to noise ratios. For these reasons, there is a rich history of spectroscopic study focussing on a wide range of NO complexes. For example, NO–rare gas complexes have been well studied—see reference 1 for a review of work up to 2001. Other complexation partners include diatomic species such as N_2[2,3] and CO.[4]

More pertinent to this chapter, complexes of NO with both methane

and ethane have been previously investigated. The electronic transitions for these complexes use NO as the chromophore, and so excitation is essentially localised to that molecule. For ethane, only one previous study exists which examined the $\tilde{A} \leftarrow \tilde{X}$ transition by REMPI.[5]. This transition has also been examined in NO–methane, also by REMPI, in several previous studies,[6–9] as well as by velocity map imaging.[10] The $\tilde{X}$ state of NO–methane has also been investigated by near-IR+UV double-resonance experiments.[11] A study also exists which examined the $\tilde{C} \leftarrow \tilde{X}$ transition in addition to the aforementioned $\tilde{A} \leftarrow \tilde{X}$.[6] Some theoretical work has been carried out on the $\tilde{X}$ state of NO–methane, by Crespo-Otero *et al.*[12] and Poad *et al.*,[13] as well as by the Wright group previously.[8,9]

This chapter re-examines the $\tilde{A} \leftarrow \tilde{X}$ transition in NO–methane and NO–ethane. Further to this, spectra of the same transition for NO–propane and NO–(*n*–butane) are presented, which are the first such spectra of these complexes, in addition to complementary *ab initio* calculations being conducted on the ground state of the 1:1 complexes.

9.2 Experimental

The NO–alkane (alkane = methane, ethane, propane, and *n*–butane) series of complexes has been investigated using (1 + 1) REMPI (see Section 7.1). The third harmonic of the output of a Nd:YAG laser (355 nm) was used to pump a dye laser operating with Coumarin 450, the output of which was frequency-doubled into the UV. This UV was used at typical pulse energies of ∼0.5 mJ / pulse and focussed using a 300 mm lens into the ionisation region of the spectrometer.

Complexes were formed from a supersonic jet expansion of a gaseous mixture held at a stagnation pressure of 5 bar. Argon was used as the backing gas, with ∼2 % of NO (99.5 % purity) and ∼10 % of the alkane of

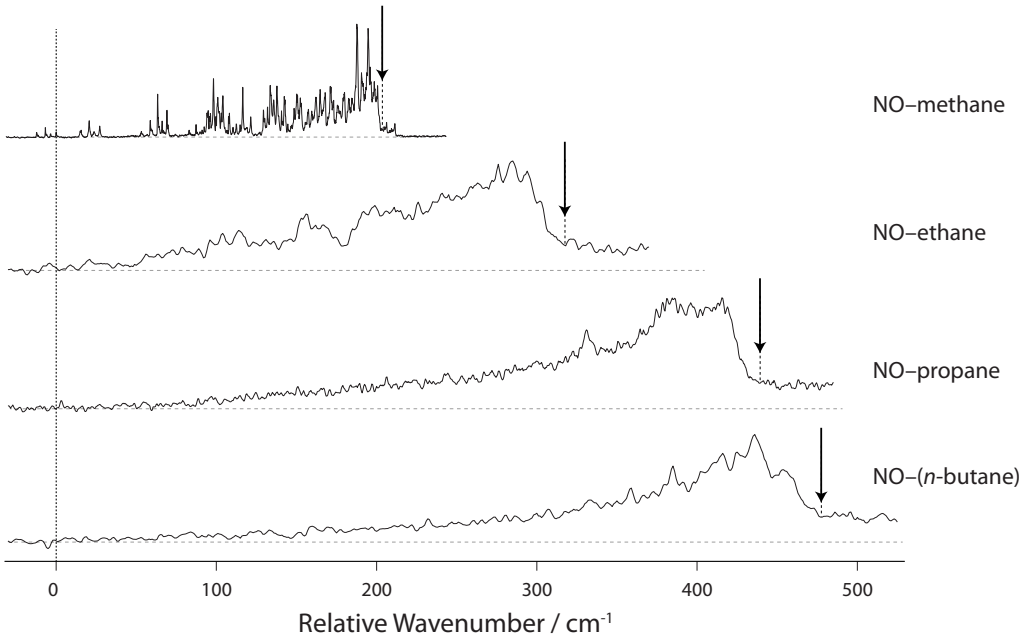


Figure 9.1: (1 + 1) REMPI spectra of the 1:1 NO–alkane complexes shifted so that the pure electronic transition is at zero wavenumber—see Table 9.1 for values of T_0. The data for NO–methane comes from Reference 9. The lines marked on the spectra indicate D_{L}, the dissociation limit being reached.

interest (98 % purity) by partial pressure.

Due to the very high oscillator strength of NO, an intense non-resonant signal originated from the uncomplexed diatomic, and so a mass gate (see Section 7.1) was used to minimise inteference with the spectra recorded in the complex mass channels.

The spectra were calibrated using the $\tilde{\mathrm{A}} \leftarrow \tilde{\mathrm{X}}$ transition for uncomplexed NO, as recorded by Danielak *et al.* using emission spectroscopy.[14]

9.3 NO–Alkane 1:1 Complex Spectra

Presented in Figure 9.1 are the spectra that have been recorded for the NO–alkane 1:1 complexes via the NO $\tilde{\mathrm{A}}$ state. Although spectra were recorded for the NO–methane complex during the present work, it was deemed that Reference 9, previously published by our group, contained a spectrum of better quality, and as such that is the data presented here.

9.3.1 NO–methane

The NO–methane spectrum in Figure 9.1 shows well defined groups of features at low energy. The overall intensity of the spectrum is seen to increase towards higher energy, with more and more structure appearing until the bands overlap and become unresolved. There is then a sharp drop in intensity, which is assigned as corresponding to the dissociation limit being reached according to Equation 9.1:

$$\text{NO–alkane} \rightarrow \text{NO} + \text{alkane} \tag{9.1}$$

There are some weak features beyond this point, which likely arise due to quasi-bound states above the dissociation limit.

In reference 9, structure within each group of features was assigned as arising from the hindered internal rotation of the methane molecule, and each group of features was ascribed to vibrational activity in the degenerate van der Waals bending mode—assignment of any low-energy bands to activity in the van der Waals stretching mode was ruled out based upon negligible isotopic shifts in the deuterated isotopomer.[7] The origin band was assignable as the band in the first group of features which has $j_{\mathrm{M}} = 0$ in both the $\tilde{\mathrm{X}}$ and $\tilde{\mathrm{A}}$ states, which was identified as being at 44 104.1 cm^{-1}.

It is possible to determine a dissociation energy for the $\tilde{\mathrm{A}}$ state by measuring the energy of the sharp drop-off in intensity or 'offset', D_{L}, which corresponds to the dissociation continuum being accessed. For NO–methane, D_{L} is seen to occur at 44 305 cm^{-1}; the difference between this value and the pure electronic transition energy, T_0, gives the zero-point dissociation energy for the excited state, D_0', which in this case is 201 cm^{-1}.

Using D_0' and the excitation energies for both the NO–alkane complex and uncomplexed NO, it is possible to determine the ground state binding

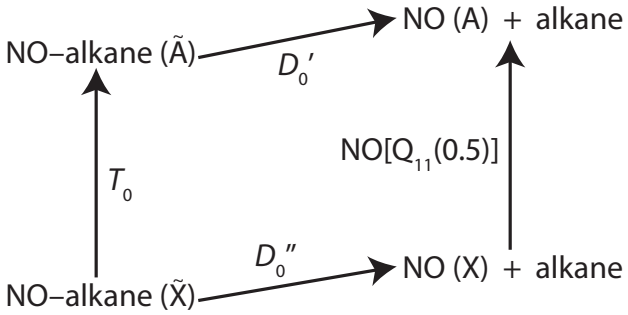


Figure 9.2: Energetic cycle used to calculate the ground state binding energy D_0''.

energy, D_0'' of this species using the energetic cycle outlined in Figure 9.2. Since D_L is equal to $T_0 - D_0'$, then D_0'' is found from Equation 9.2:

$$D_0'' = D_\mathrm{L} - \mathrm{NO}[\mathrm{Q}_{11}(0.5)] \tag{9.2}$$

which for NO–methane is 107 cm^{-1}. Use of D_L in place of $(D_0' - T_0)$ also provides the significant advantage of avoiding uncertainties in the determination of T_0 due to the gradual onset; the values of D_L come with much lower uncertainty, since the offset in the spectra are far better defined.

9.3.2 NO–ethane

The NO–ethane spectrum in Figure 9.1 shows less resolved structure than for NO–methane, with some partially-resolved features evident on top of an overall rise in intensity. Many vibrational modes are present in the ethane molecule—not only does this make it difficult to cool the molecule fully in

	T_0 / cm^{-1}	D_L / cm^{-1}	D_0' / cm^{-1}	D_0'' / cm^{-1}	D_e / cm^{-1}
NO–methane	44 104	44 305	201	107	201
NO–ethane	44 070	44 390	320	190	279
NO–propane	44 010	44 445	435	245	249
NO–butane	44 030	44 505	475	305	263

Table 9.1: Spectral parameters for the NO-alkane binary complexes. T_0 is the pure electronic transition, D_L is the dissociation limit, D_0' and D_0'' are the zero-point dissociation energies for the $\tilde{\mathrm{A}}$ and $\tilde{\mathrm{X}}$ states respectively, and D_e is the $\tilde{\mathrm{X}}$ state equilibrium dissociation energy from RCCSD(T) calculations at the UMP2 optimised geometry, using the 'best' result available.

the supersonic jet expansion, but it also potentially leads to a large number of spectral features arising from fundamental, overtone, and combination bands. Consequently, resolving all of these features does not seem to be possible with the laser bandwidth used here. Structural factors are also likely to play a role in the congestion of this spectrum, as will be discussed in section 9.4.3.

The gradual onset and long progression of features indicate that there is likely to be a large change in geometry between the ground and excited states, leading to relatively poor Franck-Condon factors. Even so, there is a markedly sharp drop in intensity still present corresponding to the point at which the complex dissociates, at 44 390 cm^{-1} as marked on the spectrum. The pure electronic transition, T_0, is taken as the point at which the onset of the spectrum begins, at 44 070 cm^{-1}; thus, D_0' is seen to be 320 cm^{-1}. Using the relationship in Equation 9.2, the ground state energy is found to be 190 cm^{-1}.

9.3.3 NO–propane and NO–(*n*–butane)

The NO–propane and NO–(*n*–butane) spectra are similar in appearance to that of NO–ethane, in that there is a weak initial onset indicative of poor Franck-Condon factors, with a gradual increase in intensity. There are also similarly partially-resolved features on top of the overall increase in intensity, with a sharp drop-off in intensity which corresponds to the dissociation limit being reached.

T_0 and D_L are read from the spectra as for the previous NO–alkane complexes, and the same relationships used to obtain the excited and ground state binding energies. For NO–propane this yields a value for D_0' of 435 cm^{-1}, and D_0'' of 245 cm^{-1}. The *n*–butane complex gives corresponding values of 475 cm^{-1} and 305 cm^{-1}.

9.3.4 Discussion of Binding Energies for the 1:1 NO–alkane Spectra

Table 9.1 collects the spectroscopic parameters for the NO–alkane 1:1 complexes. The estimated error in the values of T_0, taken from the shallow onsets, is ± 20 cm^{-1} for NO–ethane, although for the longer chain alkanes this increases due to shallower onsets. The onset of NO–methane is much better defined, and the error in D_0'' will be correspondingly much lower. The estimated error for the values of D_{L}, taken from the better defined sharp offsets, is estimated to be ± 5 cm^{-1}.

There is a consistent and progressive redshifting of the values of T_0 with increasing length of alkane from the NO[$Q_{11}(0.5)$] value of 44 199 cm^{-1}. The *n*–butane complex seemingly does not follow this trend, but this deviation is within the margins of error in estimating the dissociation energies of these complexes. Polarisabilities for the alkane molecules are seen to increase with increasing chain length, with the values being 2.59, 4.43, 6.37, and 8.20 Å^3 through the series.[15] Concurrent with these increasing polarisabilities is an increase in the binding energies, as seen in Table 9.1. This dependency of the binding energy on the polarisability suggests that the dipole/induced-dipole term is a significant contributor to the attractive terms. Consideration of the dipole/induced-dipole term alone, however, is an oversimplification, as the dispersion and repulsion terms will also vary as the alkane is varied.

Upon excitation to the $\tilde{\mathrm{A}}$ state, there is seen to be an increase in the binding energies. Again, the rationale for this is based upon the dipole/induced-dipole term increasing, as NO($\mathrm{A}^2\Sigma^+$) has a dipole moment of 1.08 D,[15] notably larger than 0.16 D for the $\tilde{\mathrm{X}}$ state.[16]

9.4 NO–Alkane 1:1 Complex Ground State Calculations

Electronic structure calculations have been carried out on the NO–alkane 1:1 complexes. Geometry optimisations have been carried out for the $\tilde{\mathrm{X}}$ state of the complexes, and equilibrium dissociation energies, D_{e}, calculated at these optimised geometries. These values are not directly comparable to the experimentally derived dissociation energies, as they do not take into account the zero-point vibrational energy (ZPVE) which is present in a 'real' system. The zero-point dissociation energy, D_0, can be obtained using these values in conjunction with calculated harmonic vibrational frequencies; however, as will be discussed in Section 9.4.2, this approach is not suited to the present case. The qualitative trends from D_{e} values however are instructive, and the discrepancy between the experimental and theoretical approaches will be informative of the ZPVE in the systems (assuming both binding energies are reliable).

9.4.1 Computational Methodology

Starting from a wide variety of initial geometries, geometry optimisations for the $\tilde{\mathrm{X}}$ state of the complexes were carried out using UMP2 theory and aug-cc-pVTZ (henceforth abbreviated aTZ) basis sets. Under C_{s} point group symmetry, both A' and A'' electronic state symmetries were considered in addition to calculations being conducted without symmetry constraints. These different symmetries correspond to the two components arising from the splitting of the doubly-degenerate $^2\Pi$ ground state of uncomplexed NO due to the presence of the nearby alkane molecule. The values of $\langle S^2 \rangle$ were examined for these spin-unrestricted geometry optimisations, and were found

to be ∼0.78 in all cases, which became the expected value of 0.75 upon annihilation of spin contamination.

At the optimised geometries, restricted open-shell CCSD(T) calculations (henceforth referred to as simply RCCSD(T)) were conducted in order to obtain more accurate dissociation energies. For NO–methane, triple-, quadruple-, and quintuple-ζ basis sets corresponding to the above were used, as well as doubly-augmented quadruple-ζ (daQZ). The NO–ethane, –propane, and –*n*–butane calculations used the same aTZ basis sets as above. The effects of basis set superposition error (BSSE) in the binding energy calculations were also investigated by application of full counterpoise (CP) correction.

9.4.2 NO–methane

Previous computational work has been conducted on the $\tilde{X}$ state of the NO–methane complex using UMP2 theory, and both 6-311++G(3d,3p) and aug-cc-pVTZ basis sets.[8,9] The conclusion from those studies was that the global energetic minimum was of A'' state symmetry, which was supported by a later study by Crespo-Otero *et al.*[12] The NO molecule was seen to be interacting with one face of the methane, the oxygen atom oriented slightly

	Theory	$D_e^{\text{non-CP}}$ / cm^{-1}	D_e^{CP} / cm^{-1}	BSSE / cm^{-1}
NO–methane	RCCSD(T)/aTZ	265	183	82
	RCCSD(T)/aQZ	230	196	34
	RCCSD(T)/daQZ	246	199	47
	RCCSD(T)/a5Z	212	201	11
NO–ethane	RCCSD(T)/aTZ	393	256	137
	RCCSD(T)/aQZ	334	279	55
	RMP2/aTZ	410	275	135
	RMP2/aQZ	360	297	63
NO–propane	RCCSD(T)/aTZ	422	249	173
NO–(*n*–butane)	RCCSD(T)/aTZ	451	263	188

Table 9.2: Calculated $\tilde{X}$ state equilibrium dissociation energies, D_e. All single-point calculations in the present study have been conducted at the optimised UMP2/aTZ energetic minimum structure.

towards it, with the NO bent slightly from C_{3v} symmetry. The geometry optimisation here was started from the same geometry of the A'' state.

For the UMP2/aTZ optimised global minimum energy structure, a single-point CP-corrected RCCSD(T) calculation was carried out here in order to gain more accurate energetics using the same aTZ basis set, the result of which is in Table 9.2. The D_e value of 183 cm^{-1} is in excellent agreement with the previous values of 181 cm^{-1} from reference 9 and 186 cm^{-1} from reference 12, both of which used the same level of theory as the calculations described here.

The effect of BSSE in the single point calculation is also given in Table 9.2, and is seen to be quite significant, at 82 cm^{-1}. Further single-point calculations were also conducted using different basis sets to shed additional light on this, using aQZ, daQZ, and a5Z basis sets. As can be seen, the value of ${D_e}^{CP}$ is seen to remain quite consistent with use of different quality basis sets, moving from 183 cm^{-1} for aTZ to 196 cm^{-1} for aQZ, and 201 cm^{-1} for a5Z. Effects from doubly-augmented basis sets are also minimal, with less than 2 % difference between aQZ and daQZ. The amount of BSSE however is seen to decrease notably as the quality of basis set increases, with the BSSE decreasing to only 11 cm^{-1} with the a5Z basis set.

Harmonic vibrational frequencies can be calculated at the UMP2/aTZ optimised geometry, and half of the sum of these used to estimate the ZPVE of the van der Waals modes for the complex. Taking the vibrational levels from reference 9 gives a ZPVE of 150 cm^{-1}, and in combination with the RCCSD(T)/a5Z value for D_e, this yields a theoretical value for ${D_0}''$ of 51 cm^{-1}. This is seen to be in very poor agreement with the experimentally determined value of 107 cm^{-1}; however, there are some complications to this approach. Magnitudes of the harmonic frequencies depend quite heavily on starting geometry, and the calculations in reference 9 used different

convergence criteria to those conducted here. Furthermore, the validity of using harmonic frequencies to calculate the ZPVE is called into question. In the $\tilde{A} \leftarrow \tilde{X}$ spectrum for NO–methane, structure arising from the van der Waals stretching mode does not make itself readily apparent for at least the first ~50 cm^{-1}, despite D_L occurring at 201 cm^{-1}. The implication is that there must be mixing between the bending mode and the van der Waals stretching mode, even at the lowest vibrational levels; indeed, it is quite possible that even the zero-point level contains anharmonic mixing between these two modes. Since the binding energy of the $\tilde{X}$ state is even less than the excited state, it is likely that the anharmonicity will be even greater, and so the use of harmonic frequencies is called into question.

Several different estimates for the ZPVE of this complex can be made. As mentioned in the above paragraph, the harmonic frequencies in reference 9 give a value of 150 cm^{-1}. Another estimate was made using a similar approach in reference 12, which gave a value of 46 cm^{-1}; it should be noted, however, that only two intermolecular modes were considered in this case, and these modes modelled the two moeities as point masses behaving harmonically. If the calculated value for D_e and the experimental value for D_0'' presented here are considered as reliable, this would place another estimate of the ZPVE for NO–methane at ~94 cm^{-1}. It should be noted in light of the above discussion that this latter estimate is the only one here which does not rely on harmonic frequencies.

Interestingly, in reference 12, Crespo-Otero *et al.* calculated the lowest barrier to alignment of the NO molecule along the C–H axis (and thus to C_{3v} symmetry) as being 77 cm^{-1}, and so the inclusion of zero-point effects could make it possible to access this geometry as the molecule undergoes vibrational motion, corresponding to the dynamic Jahn-Teller effect. The ZPVE includes contributions from all normal modes but the barrier to C_{3v}

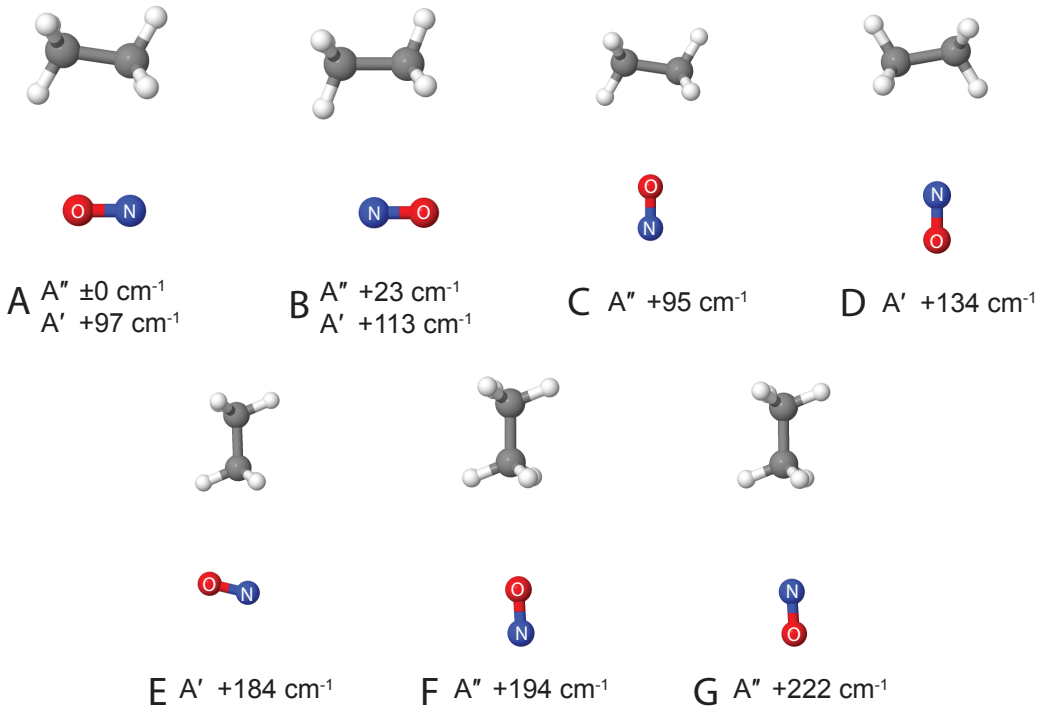


Figure 9.3: Optimised structures obtained by UMP2 calculations for the NO–ethane complex, along with the energy relative to that of the most stable structure obtained by CCSD(T) calculations.

symmetry is accessible only through certain modes, so it could perhaps be proposed that the system is instead a static Jahn-Teller system; however, the above arguments regarding coupling between differerent vibrational modes contradict this. In reference 9, intensity distributions of rotational bands were considered in the context of different nuclear spin statistical weightings, with the conclusion that the observed intensities correspond to a molecule of effective C_{3v} symmetry, which would also indicate a dynamic Jahn-Teller system. Conversely, the deductions of Wen and Meyer[11] concluded that the NO molecule is not on average aligned along the C_{3v} axis. Other studies have found the rotation of methane to be hindered by the presence of NO,[7,9] which is consistent with this static Jahn-Teller picture. In summary, whether NO–methane is a static or dynamic Jahn-Teller system is still debatable.

9.4.3 NO–ethane

For the longer-chain alkanes, no previous theoretical studies exist for comparison. The structures obtained for NO–ethane *via* geometry optimisation are presented in Figure 9.3. From the converged structures, the A'' species are seen to be consistently lower in energy, although the A' surfaces produce structures that are close in energy to these. The global minimum geometry (denoted A in Figure 9.3) is seen to consist of both molecules lying parallel, with the oxygen atom interacting with one hydrogen atom on ethane and the nitrogen situated between two others.

All of the structures considered here are seen to be quite close energetically. It is likely that once the effects of ZPVE are taken into account, the complex will sample a broad range of different geometries, and consequently these complexes are expected to be quite 'floppy', influencing the recorded spectrum significantly. Depopulating all of the higher-energy structures by means of the supersonic jet expansion would be extremely difficult if not impossible, and so many different structures may be sampled in the experiment and will contribute heavily to the congestion of features.

CP-corrected RCCSD(T)/aTZ calculations at the UMP2/aTZ minimum energy structure have been conducted, which produced a D_e^{CP} value of 256 cm^{-1} for NO–ethane. The effect of the CP correction was seen to be quite significant, with the BSSE being 137 cm^{-1}. To investigate this further, an additional RCCSD(T) calculation was performed at the same geometry but with larger aQZ basis sets. Use of larger basis sets would be expected to reduce the magnitude of BSSE, and this was seen to be the case. From the aQZ calculations, the value of D_e^{CP} was seen to remain largely consistent at 279 cm^{-1}, but the BSSE is now reduced to 55 cm^{-1}. Although the effects of BSSE are still quite large, they are proportionally smaller with these larger

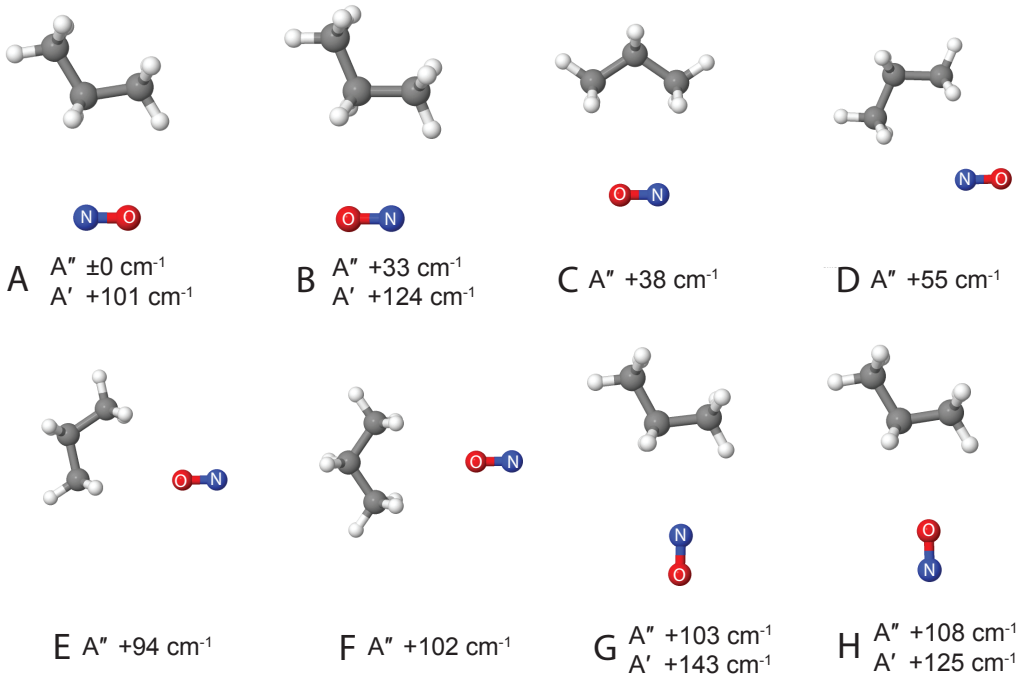


Figure 9.4: Optimised structures obtained by UMP2 calculations for the NO–propane complex, along with the energy relative to that of the most stable structure obtained by CCSD(T) calculations.

basis sets. The resulting value of D_e^{CP} is also in excellent agreement with a previously calculated value[8] of 180.8 cm^{-1}.

To check the dependence on the level of theory of these calculations, additional calculations were carried out at the same UMP2/aTZ optimised geometry, employing RMP2 theory with aTZ and aQZ basis sets and CP correction. Magnitudes of D_e^{CP} were found to be 275 cm^{-1} with the aTZ basis sets and 297 cm^{-1} with aQZ. The extent of BSSE was found to be 135 and 63 cm^{-1} respectively; in line with the RCCSD(T) results, the BSSE is seen to decrease with increasing size of basis set, and has been largely corrected for by the CP procedure.

As discussed in Section 9.4.2, calculation of ZPVE through harmonic frequency calculations is of debatable use for these complexes, and so no theoretical value for D_0'' is given here—the same is true for NO–propane and NO–(*n*–butane)

9.4.4 NO–propane

Structures of NO–propane are collected in Figure 9.4. Again, many structures are seen to lie close in energy to the global minimum, and it is again likely that with the inclusion of zero-point effects the geometry of the complex becomes quite poorly defined, significantly complicating the recorded spectrum.

The optimised global minimum structure is seen to concur with that of NO–ethane. This structure is also found to be of A″ state symmetry, with the NO molecule lying parallel to a C–C bond, and the oxygen atom interacting with a hydrogen atom.

For calculations on NO–propane, use of aQZ basis sets was found to be impracticable due to the computational expense involved, and so the results presented here have been conducted using RCCSD(T)/aTZ methodology at the UMP2/aTZ optimised geometry. The D_e^{CP} value was found to be 249 cm^{-1}, which is close to the value for NO–ethane at the same level of theory. As such, it seems that the aTZ basis sets are insufficient for a satisfactory description of the NO–propane complex, and the actual D_e^{CP} value is likely to be somewhat higher, in line with the increase in binding energy seen for NO–ethane with larger basis sets and the observed trend in the values for D_0'' determined from experiment. Again, BSSE is seen to be quite significant from Table 9.2, although use of CP correction seems to correct for this well in the D_e^{CP} value.

9.4.5 NO–(*n*–butane)

NO–(*n*–butane) is also reminiscent of the lighter complexes, as seen from the structures collected in Figure 9.5. The global minimum is seen to consist of the NO molecule lying parallel to one of the terminal C–C bonds in a

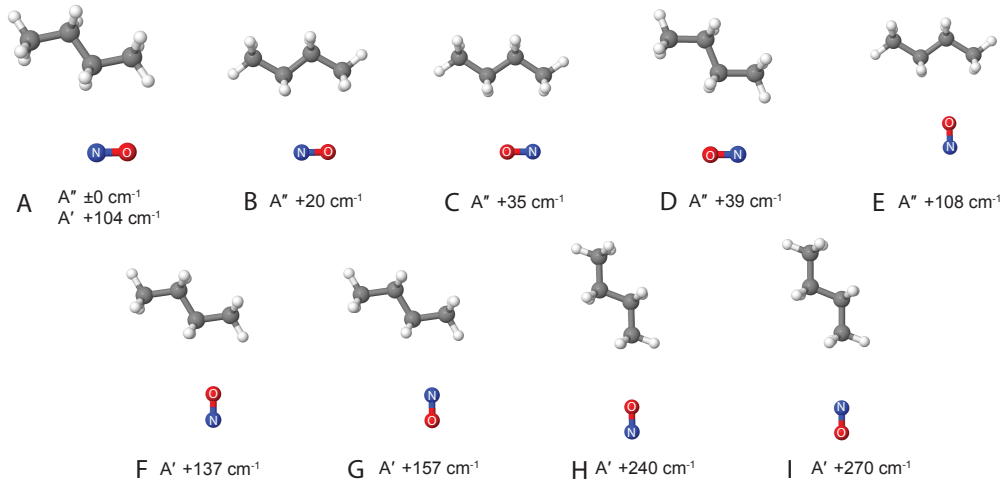


Figure 9.5: Optimised structures obtained by UMP2 calculations for the NO–(n–butane) complex, along with the energy relative to that of the most stable structure obtained by CCSD(T) calculations.

continuation of the bonding motif, with the state symmetry again found to to be A''.

From the RCCSD(T)/aTZ single-point energy calculation, the BSSE is now close to half the non-CP corrected D_e value. The $D_e{}^{CP}$ is once more very close to the values obtained for NO–ethane and NO–propane, at 263 cm^{-1}. Again, it appears that use of aTZ basis sets for binding energies does not give as good agreement with the experimental results as was seen with the larger basis sets.

	D_L / cm^{-1}	$D_0{}^{All}$ / cm^{-1}	$D_0{}^1$ / cm^{-1}
NO–ethane$_2$	45 030	830	640
NO–ethane$_3$	45 240	1 360	530
NO–propane$_2$	45 170	970	725
NO–n–butane$_2$	45 040	840	535

Table 9.3: Calculated spectroscopic constants for the higher-order NO–alkane$_n$ complexes. D_L is the measured dissociation limit, and $D_0{}^{All}$ and $D_0{}^1$ are the dissociation energies with respect to loss of all and one alkane from the excited state, respectively.

9.5 Higher-Order NO–Alkane$_n$ Complexes

No evidence for the formation of higher-order NO–methane$_n$ complexes was observed in the mass spectrum, and no spectral features were observed in the spectrum recorded in the NO–methane$_1$ mass channel to indicate contamination from dissociation of any complexes with n>1. For the longer chain alkanes, however, evidence was observed for the NO–alkane$_2$ complexes, and in the case of ethane, NO–ethane$_3$ also.

For these spectra, the gradual onset and offsets are rather more poorly defined than for the 1:1 complexes, due to the poorer signal-to-noise ratios. Consequently, binding energies for the complexes in the $\tilde{A}$ state are not provided, although values of D_L can still be used to give a reasonable estimate of the $\tilde{X}$ state binding energies. Owing to the likelihood of the full extent of the vibrational structure not being observed, these values are best considered as lower bounds.

9.5.1 NO–ethane$_2$

Signals were detected whilst recording the NO–ethane$_1$ spectra corresponding to the formation of higher-order complexes of the form NO–ethane$_n$. It proved possible to record spectra in the precursor mass channels for these heavier complexes up to $n = 3$, and these spectra are shown in Figure 9.6 along with the full-range spectrum recorded in the NO–ethane$_1$ mass channel. As can be seen for the spectrum recorded in the NO–ethane$_1$ mass channel, contributions from the dissociation of the higher-order complexes into the lower mass channels are evident as broad, unresolved structure to the blue of the dissociation limit of NO–ethane$_1$.

Unresolved features in these higher-order spectra arise due to more vibrational features being present, as well as possible complications arising

from multiple conformers; additionally, these complexes will be more difficult to cool than the 1:1 complex, and so it is quite likely that warm features are also contributing. The gradual onset and offset of the observed spectra for $n>1$ indicates a large change in geometry, leading to the observed Franck-Condon envelope.

The point at which the NO–ethane$_2$ spectrum returns to baseline intensity is seen to be slightly blueshifted from the position at which the unresolved structure in the NO–ethane$_1$ spectrum ends, at point *d* in Figure 9.6. It is likely that this is due to contamination of the NO–ethane$_2$ spectrum by NO–ethane$_3$, in the same way the NO–ethane$_1$ spectrum is contaminated by NO–ethane$_2$. Consequently, the D_{L} value for NO–ethane$_2$ is taken from point *c* in the NO–ethane$_1$ spectrum. For NO–ethane$_2$, the energy D_{L} is taken to correspond to loss of both alkanes, and so the binding energy, ${D_0}^{\mathrm{All}}$,

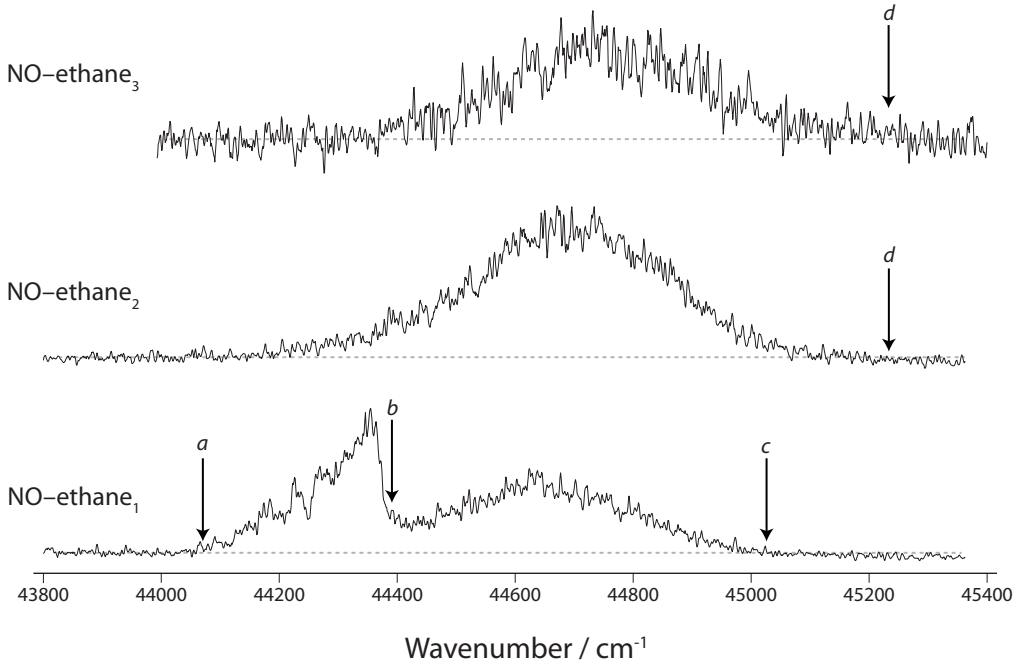


Figure 9.6: Higher-order NO–ethane$_n$ spectra. The marked arrows correspond to the following quantities; *a*) T_0 for NO–ethane$_1$, *b*) D_{L} for NO–ethane$_1$, *c*) D_{L} for NO–ethane$_2$, *d*) D_{L} for NO–ethane$_3$.

can be evaluated by use of Equation 9.3:

$$\text{NO–alkane}_2 \rightarrow \text{NO} + 2(\text{alkane}) \tag{9.3}$$

For the present case, this is calculated as 830 cm^{-1}. Subtracting the value of D_0' for NO–ethane$_1$ from $D_0{}^{\text{All}}$ gives the energy for loss of one alkane molecule, $D_0{}^1$, as 640 cm^{-1}.

Comparing $D_0{}^1$ and D_0'' shows that the energy for dissociation of a single alkane from NO–ethane$_2$ requires significantly more energy than removal of the second alkane. Furthermore, the energy of $D_0{}^1$ is, by virtue of its relation to $D_0{}^{\text{All}}$, a lower bound. Regardless, the substantial differences in energy for loss of one or two alkane molecules implies different modes of binding. A 2006 study by Tsuzuki *et al.* calculated the D_e values for the alkane dimers using MP2 theory and varying basis sets, the results of which were extrapolated to the basis set limit,[17] with the result for ethane$_2$ being 470 cm^{-1}. Although these theoretical results are equilibrium values and as such do not include zero-point effects, with the inclusion of ZPVE this value would likely be brought into better agreement with the experimentally derived $D_0{}^1$. Overall, it seems likely that this complex is of the form NO–ethane–ethane, rather than ethane–NO–ethane.

9.5.2 NO–ethane$_3$

The spectrum recorded for NO–ethane$_3$ is also seen in Figure 9.6. Its appearance is similar to that of NO–ethane$_2$, in that it consists of broad, unresolved structure. The high-energy offset at point *d* occurs at essentially the same position as the offset in the spectrum recorded in the NO–ethane$_2$ mass channel, and so, as mentioned above, the spectrum is thought to be affected by dissociation of the NO–ethane$_3$ complex into the lower mass

channel. D_L is read off from both spectra as occurring at 45 240 cm^{-1}; what process this energy corresponds to, however, is not necessarily straightforward to deduce.

It is possible that at D_L, the complex fully dissociates into NO + 3(ethane). $D_0{}^{All}$ is then found by subtraction of NO[$Q_{11}(0.5)$], giving a value of 1040 cm^{-1}. Since the binding energy of $D_0{}^{All}$ is also known for NO–ethane$_2$, the difference between the two is equal to the energy for dissociation of one alkane form NO–ethane$_3$, and this is found to be 210 cm^{-1}. This value is quite close to D_0'' for NO–ethane$_1$, and would imply that the third alkane is binding to the complex in a similar fashion to the first. In conjunction with the conclusion as to the form of NO–ethane$_2$ discussed above, this would give the complex the overall form ethane$_2$–NO–ethane. This seems to be at odds with the energetic stabilisation the second alkane obtains from interaction with the first alkane rather than the NO molecule directly.

Alternatively, the energy of D_L could be interpreted as corresponding to the energy for loss of two ethane molecules from the complex. From this assumption, the ground state binding energy for loss of all three ethane molecules can be found by summing D_L and D_0' for NO–ethane$_1$ and then subtracting NO[$Q_{11}(0.5)$], giving a $D_0{}^{All}$ value of 1 360 cm^{-1}. The energy for dissociation of one alkane can be found as above, giving a value of 530 cm^{-1}. This value of $D_0{}^1$ is seen to be in somewhat better agreement with the value of $D_0{}^{All}$ for NO–ethane$_2$, and as such would imply an overall form for the complex of NO–(ethane$_3$), i.e. the NO molecule is interacting with an alkane cluster. These findings are seen to be much more in line with the conclusions for NO–ethane$_2$, and so these are the values which are presented in Table 9.3.

9.5.3 NO–propane$_2$

Spectra were also recorded for the NO–propane$_2$ complex. The extended spectrum recorded in the NO–propane$_1$ mass channel is shown along with the spectrum recorded in the NO–propane$_2$ mass channel in Figure 9.7.

The offset of the NO–propane$_2$ spectrum occurs at almost exactly the same point as the end of the broad feature of the NO–propane$_1$ spectrum (at point *c* in both spectra), and so this energy is equivalent to dissociation of both alkane molecules from A state NO. D_{L} for NO–propane$_2$ is accordingly taken from the spectrum recorded in the precursor mass channel, and the quantity ${D_0}^{\mathrm{All}}$ found by subtraction of NO[$Q_{11}(0.5)$], giving 970 cm^{-1}. Subtraction of ${D_0}''$ for NO–propane$_1$ from this gives ${D_0}^1$ which is found to be 725 cm^{-1}, as tabulated in Table 9.3.

As was seen for NO–ethane$_2$, the difference between ${D_0}''$ and ${D_0}^1$ is seen to be significant. Again, as was concluded for the ethane complex, it is highly likely that the mode of binding for the second propane molecule is different

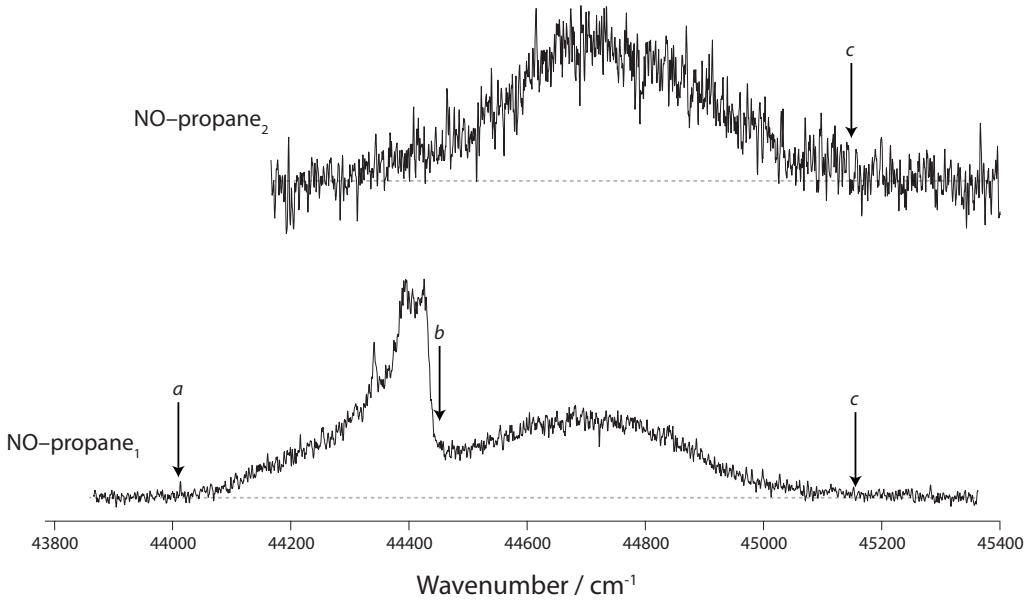


Figure 9.7: Higher-order NO–propane$_n$ spectra. The marked arrows correspond to the following quantities; *a*) T_0 for NO–propane$_1$, *b*) D_{L} for NO–propane$_1$, *c*) D_{L} for NO–propane$_2$.

from the first. The calculated equilibrium binding energy of the propane$_2$ complex has been found by Tsuzuki *et al.*[17] to be 730 cm^{-1}—this is found to be in excellent agreement with the value of $D_0{}^1$ determined experimentally. Although the uncertainty associated with $D_0{}^1$ is quite high due to the relatively poor Franck-Condon factors for the NO–propane$_2$ spectrum, the value presented here is still to be considered as a lower limit. Consequently, although the true value of $D_0{}^1$ may be higher than that presented here, and so the agreement with the calculated alkane dimer binding energy will likely worsen (as it would with inclusion of ZPVE regardless), this value is still much higher than the value of $D_0{}''$, and so it is more likely that the second propane molecule is interacting with the first (as opposed to interacting directly with the NO molecule) as was concluded for NO–ethane$_2$.

9.5.4 NO–(*n*–butane)$_2$

For the higher-order NO–(n–butane)$_n$ complexes, no spectra were able to be recorded in any precursor mass channels, but the appearance of the spectrum recorded in the NO–(n–butane)$_1$ mass channel does indicate the dissociation of complexes of n>1 into the $n = 1$ mass channel. Broad,

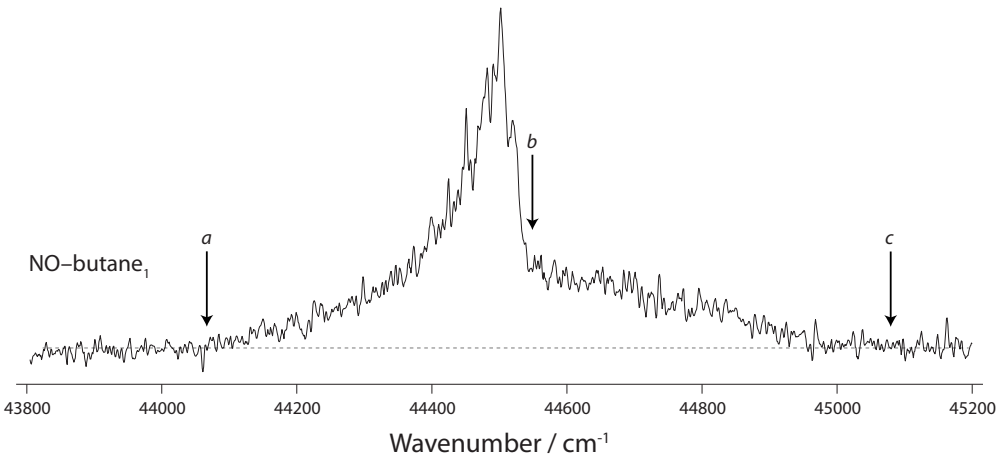


Figure 9.8: Full-range spectrum recorded in the NO–(n–butane)$_1$ mass channel. The marked arrows correspond to the following quantities; *a*) T_0 for NO–butane$_1$, *b*) D_L for NO–butane$_1$, *c*) D_L for NO–butane$_2$.

unresolved structure is seen to the blue of the sharp offset at point *b* in Figure 9.8. By analogy with the additional structure seen in the spectra recorded for NO–ethane$_1$ and NO–propane$_1$, this is attributed to NO–(*n*–butane)$_2$.

Taking D_L from the broad structure and subtracting NO[$Q_{11}(0.5)$] gives a value of the energy for loss of both alkanes, D_0^{All}—the value obtained for this is 840 cm^{-1}. Subtracting the D_0'' value for NO–(*n*–butane)$_1$ from this gives the energy for loss of one alkane, D_0^1, as 535 cm^{-1}. The discrepancy between the binding energies of successive alkanes is seen to be less pronounced here than for the other cases; however, the signal to noise ratio of the structure associated with NO–(*n*–butane)$_2$ is not as good as it was for the shorter-chain alkane complexes, and so it is highly likely that the estimated value of D_L is less accurate. There is still an apparent discrepancy between the dissociation energies for loss of successive alkanes, and so by analogy with the results for the NO–ethane$_n$ and NO–propane$_2$ complexes, the overall geometry is most likely NO–butane–butane.

9.6 Conclusions

REMPI spectra have been recorded for the $\tilde{A} \leftarrow \tilde{X}$ transition in the NO–alkane complexes for alkane = methane, ethane, propane, and *n*–butane. For NO–methane, the spectrum shows groups of features arising from activity from the intermolecular stretching mode, with individual bands within each group arising from the hindered internal rotation of the NO molecule. The spectra of the longer-chain alkanes show partially-resolved structure on top of an overall rise in intensity towards higher energy, likely due to contributions from several different geometries being present in the experiment, as well as these complexes presumably being more difficult to cool fully in the supersonic jet expansion due to the large number of vibrational modes present.

Dissociation energies for the 1:1 complexes have been determined for the $\tilde{A}$ state from the width of the observed structure, and energetic cycles have been used to also calculate binding energies for the $\tilde{X}$ state. These dissociation energies are seen to increase with increasing length of alkane, attributed to the increasing polarisabilities. The excited state is also seen to be more strongly bound than the ground state, due to the excited state of NO having a larger dipole moment than the ground state.

Calculations were undertaken for the 1:1 complexes, with geometries being optimised using UMP2/aTZ theory. In all cases, the lowest-energy structure was found to consist of the NO molecule lying parallel to one of the C–C bonds, and to be of A'' symmetry. RCCSD(T) theory was used to obtain more accurate binding energies at these optimised geometries; tests on NO–methane and –ethane showed that basis sets of triple-ζ quality give dissociation energies for these systems which show fairly poor agreement with experimental values, but computational expense limited the size of basis set which could be used for calculations on the complexes containing the longer-chain alkanes. BSSE has also been seen to be very high for the smaller basis sets, but this is corrected for by full CP correction. Use of harmonic vibrational frequencies to estimate the ZPVE has been shown to be inappropriate for these complexes, due to strong anharmonic coupling, and so the values of D_e seen here are to be considered only qualitatively.

NO–methane has been previously suggested as being a Jahn-Teller distorted system, and here an estimate of the ZPVE is seen to be likely greater than the barrier between Jahn-Teller minima as calculated by others.[12] Even so, it is unclear if this system is dynamically or statically Jahn-Teller distorted; there is no clear consensus in the literature either, as evidence for both cases has been reported.

Higher-order NO–alkane$_n$ complexes were also observed, with spectra

being recorded in the precursor mass channels for NO–ethane$_2$ and –ethane$_3$, NO–propane$_2$—additionally, evidence was observed for NO–(n–butane)$_2$ in the NO–(n–butane)$_1$ mass channel. These spectra showed broad, partially-resolved structure, with binding energies being deducible for the ground states of these complexes. Comparison of the binding energies of successive alkane molecules implies that these complexes are likely to be essentially the NO molecule interacting with an alkane$_n$ cluster.

Bibliography

[1] Y. Kim and H. Meyer, *International Reviews in Physical Chemistry*, 2001, **20**, 219–282.

[2] J. Lozeille, S. E. Daire, S. D. Gamblin, T. G. Wright and E. P. F. Lee, *The Journal of Chemical Physics*, 2000, **113**, 10952–10961.

[3] B. Wen, H. Meyer and J. Kos, *The Journal of Chemical Physics*, 2010, **132**, 154305.

[4] S. E. Daire, J. Lozeille, S. D. Gamblin, E. P. Lee and T. G. Wright, *Chemical Physics Letters*, 2001, **346**, 305–312.

[5] S. E. Daire, J. Lozeille, S. D. Gamblin and T. G. Wright, *The Journal of Physical Chemistry A*, 2000, **104**, 9180–9183.

[6] J. C. Miller, *The Journal of Chemical Physics*, 1987, **86**, 3166–3171.

[7] M. Akiike, K. Tsuji, K. Shibuya and K. Obi, *Chemical Physics Letters*, 1995, **243**, 89–93.

[8] S. E. Daire, J. Lozeille, S. D. Gamblin, T. G. Wright and E. P. F. Lee, *Phys. Chem. Chem. Phys.*, 2001, **3**, 917–924.

[9] A. Musgrave, D. E. Bergeron, R. J. Wheatley and T. G. Wright, *The Journal of Chemical Physics*, 2005, **123**, 204305.

[10] D. S. Wright, H. L. Holmes-Ross and W. D. Lawrance, *Chemical Physics Letters*, 2007, **435**, 19–23.